UNIVERSIDADE DE LISBOA
FACULDADE DE CIÊNCIAS
DEPARTAMENTO DE FÍSICA

Exploring Titan's Atmosphere Composition and Temporal Evolution using High-Resolution Spectroscopy, and its Interaction with the Surface using Atomistic Molecular Dynamics Simulations

Rafael Duarte Rianço Gomes da Silva

Mestrado em Física
Especialização em Astrofísica e Cosmologia

Dissertação orientada por:
Prof. Dr. Pedro Machado (FCUL, IA)
Prof.ª Dr.ª Zita Martins (IST, CQE)

2023

Abstract

The atmosphere of Titan is a unique natural laboratory for the study of atmospheric evolution and photochemistry akin to that of the primitive Earth, with a wide array of complex molecules discovered through infrared and sub-mm spectroscopy. Experimental simulations have suggested the synthesis of organic molecules under the conditions of Titan's atmosphere. In this work, I analysed very high-resolution visible VLT/UVES spectra of Titan and developed a new line characterisation method that retrieved an empirical high resolution linelist of methane (CH_4) with 97 new absorption lines between 5250Å and 6180Å, for 4 CH_4 visible bands for which no similar linelists are yet available. Furthermore, I searched for the predicted, but previously undetected carbon trimer, C_3, on the atmosphere of Titan, at its 4051Å band on VLT/UVES spectra. The results are consistent with the presence of C_3 at the upper atmosphere of Titan, with a column density of 10^{13} cm^{-2}. This first tentative detection of C_3 in Titan may provide much needed constraints to models of its upper atmosphere photochemistry. I have also run molecular dynamics simulations of amino acid films in Titan, aiming to computationally replicate laboratory experiments and measure intermolecular interactions between amino acid molecules. This study of Titan's atmosphere with very high-resolution visible spectroscopy presents a unique opportunity to observe a small planetary target with CH_4 on its atmosphere, from which CH_4 optical proprieties can be studied. It also showcases the use of a close planetary target to test new methods for chemical retrieval of minor atmospheric compounds, in preparation for upcoming studies of cold terrestrial exoplanet atmospheres. Molecular dynamics simulations of organic molecules performed during this work are complementary to laboratory and future *in situ* studies of organic molecules in extraterrestrial environments, paving the way to assess the potential for habitability of icy moons.

Keywords: Planetary Atmospheres, Titan, Organic molecules, High resolution spectroscopy, Molecular dynamics simulations

Resumo

Titã, a maior lua de Saturno é um dos mundos no sistema solar que atrai mais atenção do ponto de vista das ciências atmosféricas e da astrobiologia. É um mundo gelado, mas com uma atmosfera complexa, com uma pressão à superfície próxima da terrestre, assim como uma composição atmosférica dominada pelo Nitrogénio molecular. Crucialmente, o segundo gás mais abundante nesta atmosfera, o metano (CH_4), é destruído fotoquimicamente na estratosfera de Titã, permitindo que os seus átomos se recombinem e reajam com o nitrogénio atmosférico, formando hidrocarbonetos e nitrilos de complexidade crescente. Alguns desses compostos sofrem condensação e chovem sobre a superfície gelada de Titã, formando os mares polares de hidrocarbonetos de Titã, os únicos corpos líquidos superficiais conhecidos fora do planeta Terra.

Muitas destas moléculas mais complexas têm vindo a ser descobertas com recurso a espectroscopia de alta resolução em comprimentos de onda infravermelhos e sub-mm. O espectro de alta resolução de Titã em comprimentos visíveis tem sido menos estudado. Este trabalho de mestrado é então focado em analisar observações espectrais de Titã em comprimentos de onda visíveis em alta resolução. Para tal, usam-se espectros obtidos pelo espectrógrafo de alta resolução VLT/UVES, em dados de arquivo e observações dedicadas pelo grupo de Sistema Solar no Instituto de Astrofísica e Ciências do Espaço, com cuja expertise foi possível aprender a processar e calibrar dados espectrais de alta resolução.

O gás metano é um dos compostos mais relevantes nas ciências planetárias atuais, pela sua relação com os processos de evolução atmosférica em mundos gelados como Titã (não se conhecendo ainda a origem da reposição geoquímica do metano destruído irreversivelmente nesta atmosfera), mas também pela sua importância astrobiológica, sendo considerado uma bioassinatura em planetas rochosos, como é o caso da Terra ou de Marte. Tal é a sua importância que novos observatórios como o telescópio espacial James Webb e a missão ARIEL são especialmente sensíveis às bandas de absorção infravermelhas do CH_4. Apesar disto, as bandas visíveis de metano não estão ainda caracterizadas em alta resolução, não se conhecendo em pormenor as linhas de absorção visíveis de metano. É por isso um dos objetivos deste trabalho de mestrado caracterizar 4 das bandas de absorção visíveis de CH4 incluídas no espectro de alta resolução de Titã (centradas a 6190Å, 5970Å, 5760Å e 5430Å).

Para detetar linhas de absorção de CH_4 em Titã no espectro de alta resolução havia que ser capaz de distingui-las das muito prevalentes linhas de absorção solar do espectro de Titã (que corresponde essencialmente ao espectro solar que sofreu retrodispersão na névoa fotoquímica que cobre o globo de Titã). Aproveitando o facto de as observações de arquivo de Titã com o VLT/UVES (de alta resolução, R = 100.000) corresponderem a diversas noites de observação durante o mesmo mês, constatou-se que a alta resolução destes espectros permitia a observação de desvios Doppler das linhas solares entre noites de observação, devido às distintas velocidades radiais entre o Sol e Titã no decurso da sua órbita. Constatou-se também que semelhante desvio não ocorria em linhas de absorção presentes no espectro que não correspondiam a nenhuma linha do espectro solar.

Baseado neste efeito de desvio Doppler, foi possível desenvolver todo um novo método para deteção

e caracterização de linhas espectrais originárias de uma atmosfera planetária, distinguindo-as de linhas de absorção solares. Desta forma, foi possível detetar 97 novas linhas de absorção de metano nas 4 bandas de absorção visíveis desta molécula. Usando 2 métodos alternativos, foi também possível estimar a intensidade das linhas de absorção, tendo para tal sido necessário integrar um perfil atmosférico de metano em Titã até ao seu raio ótico nestes comprimentos de onda.

Neste trabalho, também foram analisados dados de observações dedicadas de Titã com o instrumento VLT/UVES (desta vez com uma resolução inferior, $R = 60.000$) em busca da banda de absorção de 4051Å de uma molécula até agora nunca observada em atmosferas planetárias: o tricarbono, ou C_3. A existência desta molécula transiente nas camadas mais altas da atmosfera de Titã fora prevista por modelos fotoquímicos dedicados a compreender a química atmosférica nas camadas mais energéticas, e ao contrário de muitas das restantes moléculas presentes na atmosfera de Titã, tem as suas principais bandas de absorção em comprimentos de onda visíveis.

Dada o previamente inexistente interesse nesta molécula por parte da comunidade de astrofísica planetária, nenhum modelo espectral da absorção desta molécula existia para uma atmosfera planetária. Houve, por isso, que desenvolver, ao longo deste trabalho de mestrado, um modelo simples e aproximado (modelo de 1 camada) que replique a transferência radiativa através da atmosfera de Titã, e simule a absorção que uma densidade de coluna N de C_3 numa camada da alta atmosfera de Titã causa no espectro visível de alta resolução de Titã. Obtendo estes espectros sintéticos de Titã sem C_3 e com quantidades variáveis deste gás, foi possível fazer a deteção (tentativa) de 3 linhas de absorção no espectro observado de Titã que não são explicadas pelo espectro solar retrodisperso pela névoa de Titã. Pelo contrário, estas 3 linhas de absorção no espectro de Titã, apesar de pouco profundas, coincidem em comprimento de onda com 3 linhas de absorção de C_3 – promovendo o melhor fit um espectro sintético de Titã com uma densidade de coluna de C_3 de 10^{13} cm^{-2}.

Dado o reduzido número e profundidade das linhas de absorção de C_3 tentativamente detetadas, preparou-se uma proposta de observação de Titã com um instrumento que permite uma resolução espectral ainda maior ($R = 190.000$), o espectrógrafo VLT/ESPRESSO. O objetivo desta observação será confirmar a deteção de C_3 a partir da deteção de pelo menos 9 linhas de absorção, para observações com um Doppler Shift de espectro solar mais favorável à deteção de linhas de C_3.

O interesse da comunidade científica em Titã não se circunscreve apenas à sua química atmosférica. Simulações laboratoriais sugerem que nas condições da atmosfera de Titã é possível a formação abiótica de moléculas orgânicas como bases azotadas (centrais ao ácidos ribonucleico, ARN, e desoxirribonucleico, ADN, que contêm a informação genética em todos os seres vivos na Terra) e aminoácidos (os monómeros constituintes das proteínas de todas as formas de vida na Terra). Surge então a pergunta: o que sucede a todas estas moléculas orgânicas potencialmente depositadas na superfície gelada de Titã? Experiências laboratoriais de irradiação de filmes finos de aminoácidos (glicina, alanina e ácido α-aminobutírico) depositados sobre gelo, nas condições de Titã, estão precisamente a ser efetuadas para responder a esta pergunta, pelo grupo de Astrobiologia do Instituto Superior Técnico. De forma a poder estudar as interações intermoleculares em filmes finos de aminoácidos e comparar os seus resultados com os resultados laboratoriais, durante o meu trabalho de mestrado preparei e corri uma série de simulações computacionais de dinâmica molecular. Para tal, foi usado o software de simulações de dinâmica molecular GROMACS.

Apesar de terem sido efetuados alguns desvios às condições de Titã (e das condições experimentais) ao modelar os filmes de aminoácidos na sua fase líquida em lugar da de sólido amorfo, foi possível retirar algumas conclusões acerca das interações intermoleculares entre aminoácidos. Os aminoácidos em estudo, nas condições de Titã, apresentam um estado Zwitterónico em que, apesar de globalmente neutros,

2 dos seus grupos funcionais formam iões de polaridades opostas. Nas simulações de filme fino (que permitiram estudar a estrutura emergente no líquido) foi possível observar algum grau de organização, devido à aglomeração de grupos funcionais mais polares no interior do filme, levando à concentração das cadeias laterais neutras dos aminoácidos na interface com o vácuo.

Além disso, simulou-se também o interior de um filme líquido de aminoácidos, longe de efeitos de organização causados pelas interfaces. Nestas simulações foi possível obter funções de distribuição radial de átomos de hidrogénio (do grupo amina) na vizinhança de átomos de oxigénio (do grupo carboxilo) entre aminoácidos diferentes. Calculou-se com base nestes perfis radiais o número de átomos de hidrogénio vizinhos a átomos de oxigénio, correspondentes a átomos que estabelecem pontes de hidrogénio.

Concluindo, estudar a atmosfera de Titã com espectroscopia visível de alta resolução é uma oportunidade única de observar um alvo planetário com CH_4 na sua atmosfera, permitindo o estudo das propriedades espectrais desta molécula. Permite também o uso de uma atmosfera próxima e quimicamente complexa para testar novos métodos para a deteção remota de elementos químicos minoritários na atmosfera – preparando futuros estudos de atmosferas de exoplanetas rochosos como a missão ARIEL. Já as simulações de dinâmica molecular de aminoácidos feitos neste projeto são profundamente complementares a estudos em laboratório e (futuramente) in situ sobre moléculas orgânicas em ambientes extraterrestres e no estudo da habitabilidade de luas geladas.

Palavras chave: Atmosferas planetárias, Titã, Moléculas orgânicas, Espectroscopia de alta resolução, Simulações de dinâmica molecular

Acknowledgements

First of all, I would like to thank my family for all the unconditional support over the course of all my academic and personal journey. In particular, I wish to thank my parents, Isabel and Jorge, for motivating me to follow my passions and dreams since I was a child, and for teaching me, through their example, to work hard to achieve them. I also want to thank my sister Matilde, for always having the right words to say at the right time.

I would also like to thank my friends, near and far, who have reminded me over this past year that there is more to life than planetary astrophysics – and with whom it has been a pleasure to share talks, laughs and starry nights.

A great thank you is due to my supervisors, Dr. Pedro Machado and Dr.ª Zita Martins for their time and guidance prior to and during this master thesis work, and for giving me the opportunity to conduct scientific research in the fields of Planetary Astrophysics and Astrobiology as I have always longed for. Through your example, I saw the kind of humane scientist I wish to one day become. I also wish to thank Diogo Gonçalves at IST/CQE and my colleagues (and friends) at IA's solar system group: Francisco Brasil, Daniela Espadinha, José Ribeiro, João Dias, Diogo Quirino and Constança Freire, for all the help and the very, very fruitful collaboration over the course of the last year. It has been an immense pleasure to learn from and work with all of you.

I also owe a great thank you to the Molecular Dynamics group at IST, in particular to Dr. Tiago Eusébio, Dr. Pedro Morgado and Dr. Eduardo Filipe for all their time and crucial help with the molecular dynamics simulations software, with whom I have learned immensely. A great thank you is also due to Dr. Emmanuel Lellouch from Paris Observatory for his time and insightful discussion regarding the search for minor compounds at the atmosphere of Titan.

At last, I would like to thank my dear Susana for always being there for me in the best and worst of times, and for inspiring me every single day to explore the beauty of the Cosmos, while making this world, a "mote of dust, suspended in a sunbeam", a better place for those inhabiting it.

Financial support: This work was funded by national funds through a Research Fellowship for R&D Initiation (BII) at FCiências.ID - Associação Para a Investigação e Desenvolvimento de Ciências, for the R&D institution Instituto de Astrofísica e Ciências do Espaço, project UIDP/04434/2020, funded by the Fundação para a Ciência e a Tecnologia, I.P./MCTES through national funds (PIDDAC).

Índice

List of Figures

List of Tables

LIST OF TABLES

"We may mount from this dull Earth, and viewing it from on high, consider whether Nature has laid out all her cost and finery upon this small speck of Dirt"

- Christiaan Huygens, *The Celestial Worlds Discovered, c. 1690*

Chapter 1

Introduction

1.1 The Atmosphere of Titan - A pre-biotic chemistry laboratory?

Titan is an unique and fascinating world in our Solar System, whose singularities vaguely recall us of an exotic, yet strangely similar image of our own planet - which has been studied with crescent interest by planetary science and astrobiology as a key to solve several mysteries regarding how life might have started on Earth (Ali et al., 2015) (Hörst, 2017).

As the largest moon of Saturn, its radius is just slightly larger than that of planet Mercury (Sánchez-Lavega, 2011). However, and unlike any other solar system icy moon, Titan hosts an atmosphere, thick enough to have a surface pressure 1,5 times higher than Earth (Sánchez-Lavega, 2011). Just like our home planet, the bulk of Titan's atmosphere is comprised of N_2 (at 94%) (Sánchez-Lavega, 2011). However, it is the second main gas compound of this atmosphere, methane (CH_4, at concentrations of 5% on its troposphere) that is the origin of the great complexity of this atmosphere (Hörst, 2017).

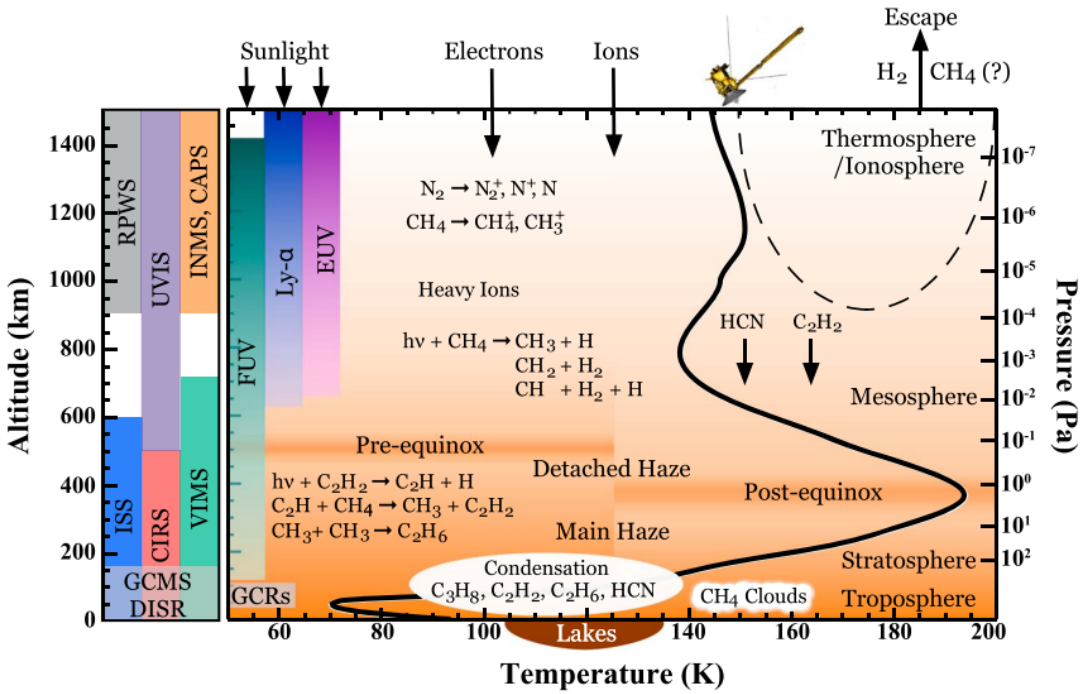

Figure 1.1: Vertical Structure and Thermal Profile of the Atmosphere of Titan, indicating the main chemical species and processes that have been reported at each atmospheric layer. From Hörst, 2017.

1. INTRODUCTION

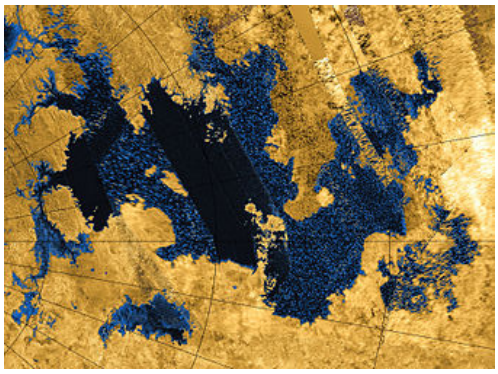

Figure 1.2: Cassini Radar image of Titan's Polar hydrocarbon liquid lake, Kraken Mare, as large as Earth's Caspian Sea, hosting an intricate coastline and respective drainage basins.

Figure 1.3: Cassini-Huygens photo of its landing site in Titan's equatorial region - with rounded ice pebbles suggesting erosion by a liquid agent.

Alongside this N_2-CH_4 atmosphere, observing Titan's atmosphere has revealed a diverse array of hydrocarbon and nitrile species that condense into optically thick global haze layers, as a result of photochemical dissociation of CH_4 (and to a smaller extent, N_2) on Titan's upper atmosphere, (see figure 1.1) (Sánchez-Lavega, 2011) (Hörst, 2017) (Coustenis et al., 2007) (Nixon et al., 2013). Complementary theoretical studies have also been conducted to model chemical species, chemical pathways and vertical profiles, in order to replicate observations and obtain new predictions that can be further tested with new data (Hérbad et al., 2013) (Dobrijevic et al., 2016) (Vuitton et al., 2019).

The hazy world of Titan was visited, at a distance, by several unmanned spacecrafts during the 70's and 80's of the last century, such as NASA's Pioneer 11, and Voyagers 1 and 2 (Hörst, 2017). Nonetheless, the landmark mission that improved dramatically our understanding of the complex world of Titan was the NASA/ESA Cassini space mission to the Chronian system (Hörst, 2017). In particular, this space mission included a small lander - Huygens - dedicated to penetrate Titan's thick atmospheric fog and descend upon this moon's icy surface (Hörst, 2017). In 2005, Huygens' landing upon Titan's surface became the most distant landing of any human spacecraft to this day. This combined mission studied the chronian system up to the atmospheric entry of the Cassini spacecraft on Saturn's atmosphere in September 2017. This landmark mission allowed numerous discoveries and advances on Titan science - namely by allowing a complete mapping of Titan's heterogeneous surface, confirming the existence of the only known liquid surface lakes beyond Earth (comprised of photochemically-produced hydrocarbons) on Titan's polar regions (figures 1.2) as well as widespread evidence for erosion caused by the presence of a liquid agent (1.3) (Hörst, 2017).

After the end of the Cassini mission, ground-based observations have been used to further constrain Titan's trace atmospheric compounds, detecting several new chemical species. This has been mostly done with sub-mm arrays such as the Atacama Large Millimetre Array (ALMA), retrieving the presence of species such as ethyl cyanide (C_2H_5CN) (Cordiner et al., 2015), vinyl cyanide (C_2H_3CN) (Palmer et al., 2017), and cyclopropenylidene (c-C_3H_2) (Nixon et al., 2020) - or with the use of high-resolution infrared spectroscopy, as was the case of the discovery of propadiene (CH_2CCH_2) (Lombardo et al., 2019), from observations with NASA Infrared Telescope Facility-Texas Echelon Cross Echelle Spectrograph (IRTF-TEXES).

Intense molecular spectral features populating infrared bands can be identified using High Resolution Infrared Spectroscopy, making of it an excellent tool to discover new molecules on chemically complex planetary atmospheres (Hanel et al., 2003) (Encrenaz et al., 2010) (Lombardo et al., 2019). Nonetheless,

molecular transitions are not limited to Infrared wavelengths, with some molecules providing examples of rich visible spectra (such as H_2O, CH_4, C_2, among others (Gordon et al., 2022) (Tennyson et al., 2016) (Villanueva et al., 2018)). However, due to the higher energies involved, associated with reduced absorption cross-sections, obtaining detailed, high resolution line-lists for molecules in shorter visible wavelengths is challenging (Hargreaves et al., 2020) (Gordon et al., 2022).

An example of this lack of detailed knowledge regarding the high resolution nature of visible molecular bands is that of methane's visible spectrum, for which no high resolution linelist exists for wavelengths below 7460Å (Hargreaves et al., 2020) even though several weaker methane absorption bands are empirically known at lower wavelengths, such as the weak 6190Å, 5970Å, 5760Å and 5430Å bands (Giver et al., 1978) (Smith et al., 1990) (Karkoschka, 1994) (Karkoschka and Tomasko, 2010). This lack of knowledge of the high-resolution nature of CH_4 spectrum is problematic for the study of planetary atmospheres within and beyond the solar system, as methane is a critically important gas on the study of planetary geochemichal history and atmospheric evolution - as well as a possible biomarker in some planetary atmospheres as is described on the section 1.1.1. Hence, one of the main goals of this masters thesis work is to characterise visible methane bands in high resolution spectra of Titan's atmosphere.

1.1.1 Methane in Rocky Worlds and the Methane Cycle of Titan

Atmospheric methane is regarded as a molecule with very significant geochemical and astrobiological interest in terrestrial planets and icy worlds (Thompson et al., 2022). This is since, for habitable zone rocky planets around Sun-like stars, atmospheric methane photochemical lifetime is expected to be rather short (< 1 Myr) in geological timescales, and hence its presence in the atmosphere requires an active replenishment source (Thompson et al., 2022). Its astrobiological potential is, in part, rooted in the fact that most of Earth's atmospheric methane is biogenic in origin, at least since Archean Earth (Thompson et al., 2022), but also due to this gas thermodynamic instability when combined with oxidising species such as CO_2 in a rocky planet's atmosphere (Krissansen-Totton et al., 2018) (Thompson et al., 2022). This suggests that large quantities of atmospheric CO_2 and CH_4 in a terrestrial planet's atmosphere are unlikely to coexist without a biological source of CH_4, particularly when observed in the absence of CO (Krissansen-Totton et al., 2018) (Thompson et al., 2022). Indeed, the detection of CH_4 in Mars' atmosphere at ppb levels (with significant temporal and spatial variability) has sparked the debate of whether the origin of gas was geochemical (through underground serpentinization reactions, whereby ferromagnesian minerals deep in a silicated planetary crust are hydrolysed and release H_2, which in turn reduces CO_2 into CH_4) or biological (by subsurface methanogenic martian microorganisms) (Krasnopolsky et al., 2004) (Formisano et al., 2004).

At the same time, the irreversible photolysis of CH_4 on Titan's atmosphere (sparking its complex atmospheric photochemistry as it is described in section 1.2.1) points towards a geochemical replenishment mechanism, since Titan's atmospheric content of this gas should have been completely depleted given its current photolysis rates (Tobie et al., 2009). Methane photolysis in Titan's atmosphere is also one of the drivers of its Methane cycle (Lunine et al., 2008), by which the atmospheric destruction of methane sparks the formation of heavier and more complex hydrocarbons such as ethane (C_2H_6) or acetylene (C_2H_2). These gases may endure condensation on Titan's atmosphere, which leads to rain (Lunine et al., 2008) (Hörst, 2017) that fills the basins on Titan's polar regions where rivers and lakes of liquid hydrocarbons form. At the same time, however, this photochemical destruction of atmospheric methane also leads to the production of molecular hydrogen (H_2), which due to its very reduced molecular weight is lost to space (Lunine et al., 2008). This means that the photolysis of CH_4 on Titan's atmosphere is

irreversible, which should lead to the depletion of Titan's atmospheric content of this gas over tens of millions of years (Lunine et al., 2008) (Thompson et al., 2022).

The continuous existence of methane on Titan's atmospheres implies therefore some sort of replenishment source, which is thought to be related to interior outgassing of significant quantities of this gas over geological timescales (Tobie et al., 2006). Unlike rocky planets, however, the geological outgassing of methane in substantial amounts onto the atmosphere is not unlikely in Titan, since models of its interior suggest the abundance of hydrated methane clathrates - ices with substantial concentration of trapped volatile molecules such as methane (Tobie et al., 2006). As the planetary interior suffers differentiation over geological timescales, it is expected that trapped volatiles in the planetary interior's ice are released into the atmosphere (Tobie et al., 2006).

With such a relevant role for the study of planetary geochemical cycles in Titan-like icy moons and as a possible biosignature in rocky planets atmospheres, the search for CH_4 spectral features in exoplanet atmospheres became a key driver for the development of new Infrared observatories such as the James Webb Space Telescope (JWST) (Gialluca et al., 2021) or the future Atmospheric Remote-sensing Infrared Exoplanet Large-survey (ARIEL) mission (Tinetti et al., 2018). Ground-based visible high resolution spectroscopy of exoplanet atmospheres may provide complementary information from the one obtained by moderate resolution infrared observatories such as JWST and ARIEL, once detailed linelist for visible bands of CH_4 are available (Hargreaves et al., 2020). High resolution visible spectra of an atmosphere such as Titan's may allow the characterisation of the line by line nature of these bands, as methane is the sole major visible molecular absorber in Titan's atmosphere (McKay et al., 2001) (Sánchez-Lavega, 2011) . As a solar system, small planetary target with atmospheric methane, Titan offers a natural testing ground for future high resolution spectroscopy observations of small and cold exoplanet atmospheres.

1.2 Key Open Questions

The exotic icy world of Titan still holds a great deal of unsolved mysteries. Pursuing a better understanding of the physical and chemical phenomena occurring today in Titan may lead us to a more complete picture of not only the complex processes occurring in this exotic world, but also of the history of planetary evolution towards pre-biotic chemistry and the set of processes that may have led to the formation of life here on Earth - and perhaps elsewhere across the Universe.

1.2.1 Titan's Photochemistry and the search for C_3

We know today that the key to Titan's complex atmospheric chemistry is **photochemistry** (Ali et al., 2015). This process is driven by high energy photons and charged particles from the Sun and Saturn that interact with Titan's upper atmosphere gases - effectively dissociating atmospheric CH_4. The resulting free Carbon and hydrogen atoms recombine into a diverse array of hydrocarbons (Lunine et al., 2008) (Hörst, 2017), driving the production of more chemically evolved products of Titan's Methane cycle. Through subsequent dissociation cycles (that also include Nitrogen atoms resulting from higher energy dissociation of N_2) the upper atmosphere of Titan is able to generate significant amounts of hydrocarbons (C_2H_2, C_2H_4, C_2H_6, C_3H_8, C_6H_6 and many others (Hörst, 2017) (Lombardo et al., 2019)) and nitrile species (such as HCN, HC_3N or CH_3CN and more complex ones (Hörst, 2017) (Palmer et al., 2017)), effectively becoming a planetary-sized organic, pre-biotic chemistry reactor.

Given the similarities between Titan's atmospheric composition and surface features (including liquid

surface lakes and a methane cycle analogous to the water cycle on Earth) to those thought to have been present on Archean Earth (Hörst, 2017) (Thompson et al., 2022), it is possible that similar photochemical atmospheric pathways may have contributed to the endogenous production of organic matter on early earth, possibly contributing to the development of life on Earth (Hörst et al., 2012) (Ali et al., 2015). Hence, there has been a considerable interest within the modelling community to explain the chemical pathways behind this chemical complexity (Hérbad et al., 2013) (Dobrijevic et al., 2016) (Vuitton et al., 2019), with these models providing a set of observable predictions regarding the chemistry of Titan's upper atmosphere (fig. 1.4)

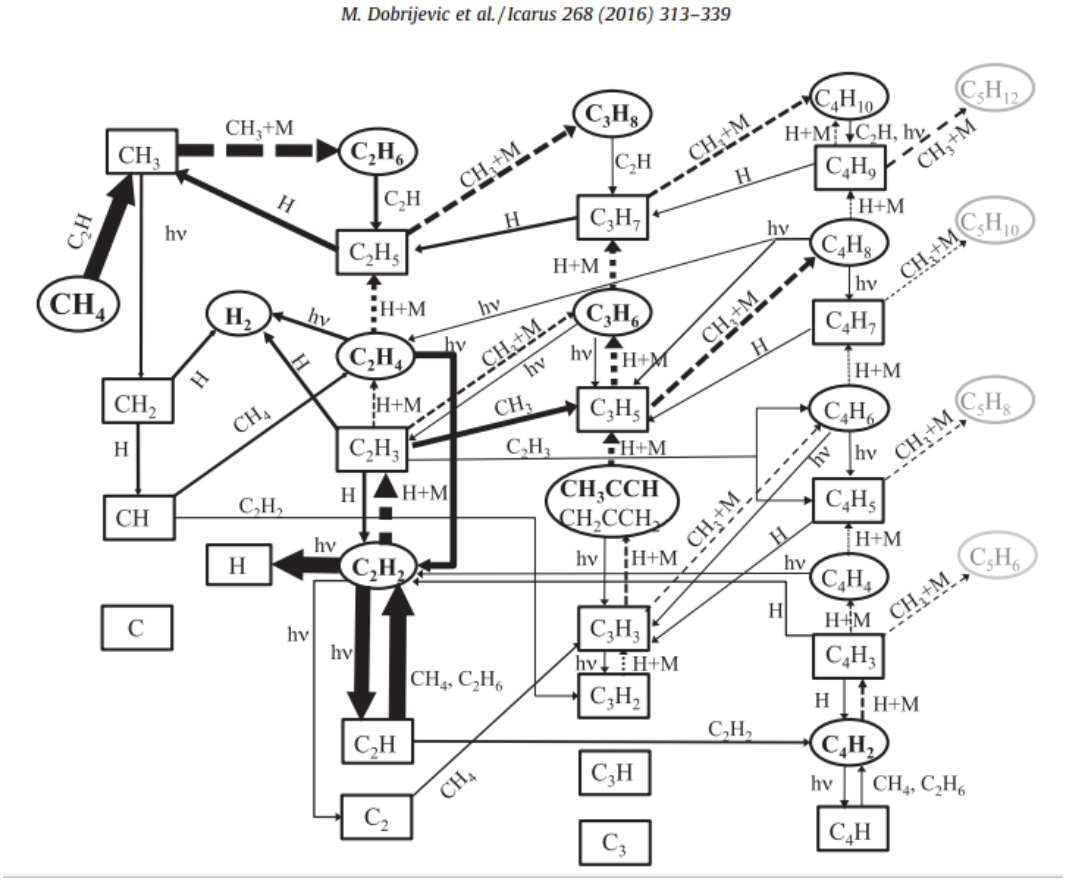

Figure 1.4: Complex photochemical pathways of hydrocarbon compounds on Titan's upper atmosphere, as modelled by Dobrijevic et al., 2016. Among the predicted species by these models appears the C_3 molecule, subject of this observational work.

Among the molecules predicted by the most recent photochemical models of Titan's atmosphere is the tricarbon molecule, C_3, which showcases its intense $\tilde{A}^1\Pi_u$ - $\tilde{X}^1\Sigma_g^+$ 000–000 (origin central band of this electronic transition) visible molecular band at 4051 Å. This molecule was firstly detected on a cometary coma (Gausset et al., 1965), subsequently found in circumstellar shells (Hinkle et al., 1988). More recently, it was detected in diffuse interstellar clouds by the high-resolution ground-based Very Large Telescope - UV-Visual Echelle Spectrograph (VLT/UVES) (Dekker et al., 2000), observing individual C_3 absorption lines part of the 4051Å band at an interstellar cloud (Roueff et al., 2002) (Schmidt et al., 2014). This species is also produced in Carbon-cluster experiments (Hinkle et al., 1988) (Schmidt et al., 2014). It has, nonetheless, never previously been detected on a planetary atmosphere (Hérbad et al., 2013).

Interest in this triatomic Carbon species on Titan's atmosphere emerged as Hérbad et al., 2013 introduced this species in a more complete model of C_3H_p (with p ranging from 0 to 8) hydrocarbon

photochemistry for Titan's atmosphere, in order to constrain heavier hydrocarbon chemistry on this environment. On their model, C_3 is mostly produced on Titan's upper atmosphere by the reaction of abundant acetylene (C_2H_2) with free atomic Carbon (Hérbad et al., 2013) as

$$C + C_2H_2 \longrightarrow C_3 + H_2 \tag{1.1}$$

The results obtained from these photochemical models predict that due to its relative stability, Carbon trimer C_3 should be one of the most abundant C_3H_p species on Titan's mesosphere and thermosphere alongside propyne (CH_3CCH), reaching molar fractions above 10 ppm at altitudes of 800km, (Hérbad et al., 2013) (Dobrijevic et al., 2016) as it is shown in Figure 1.5. Previous search for the C_3 4051Å band in solar ocultation mode archived Cassini/VIMS data had been conducted by D'Aversa et al., 2017. However, the low resolution of the VIMS instrument (∼7 nm at 400 nm) could not allow the study of individual absorption lines, in order to detect a trace chemical species such as C_3.

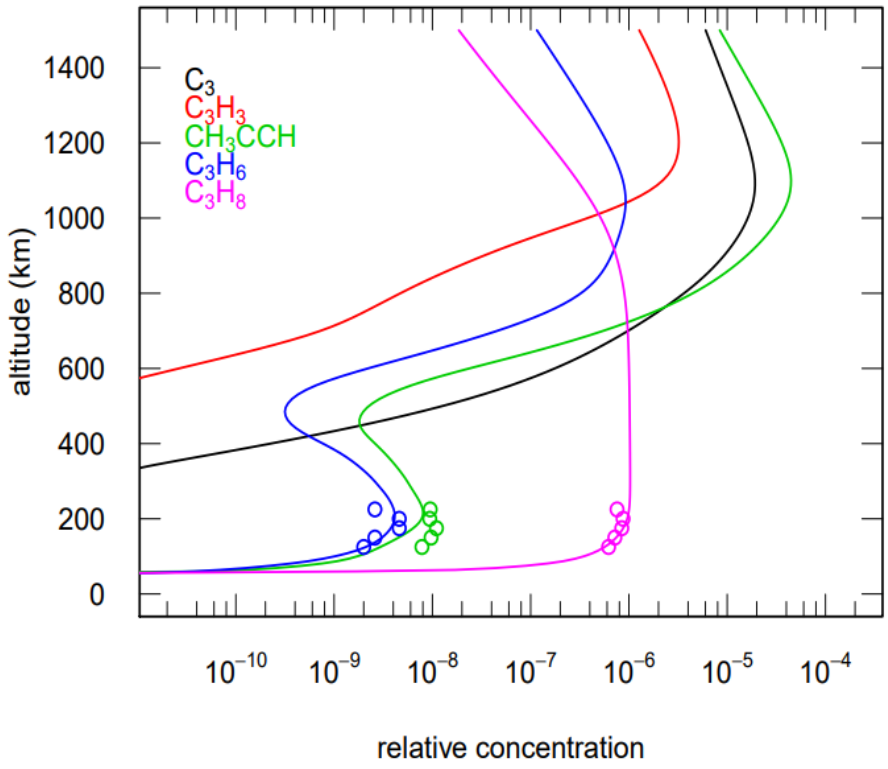

Figure 1.5: Molar fraction vertical profiles of the main C_3H_p species on Titan's Atmosphere - including Carbon trimer C_3, as one of the most abundant C_3H_p Carbon species above altitudes of 600km, following Hérbad et al., 2013 model. Comparison with Nixon et al., 2013 abundance retrievals of CH_3CCH, C_3H_6 and C_3H_8 Titan's stratosphere.

Hence, in this work I present the analysis of dedicated high spectral resolution observations of Titan with VLT/UVES in search for the 4051Å band of C_3. To confirm the presence (or infer the absence above a lower limit) of the photochemical product C_3 in the upper atmosphere of Titan would provide a rather significant observational constraint to the photochemical models used to explain the chemical pathways occurring on Titan's atmosphere. A better understanding of Titan's photochemistry may provide a clearer picture of the processes that lead to the formation of the complex organic molecules which cluster into the organic haze that covers Titan's globe (Ali et al., 2015) (Hörst, 2017), a process that shares similarities with some proposed mechanisms for endogenous atmospheric abiotic synthesis of organic molecules on early Earth (Hörst et al., 2012).

1.2.2 Atmosphere-Surface Interaction on Titan: The Photostability of Amino Acids on Titan's Icy Surface

The unsolved puzzles of Titan are not restricted to its atmosphere. Of particular interest is the study of how organic molecules produced on Titan's atmosphere interact with the solid water ice surface (Hörst, 2017). It is known that organics condensing on Titan's lower atmosphere have been deposited over geological timescales, forming vast equatorial organic dunes (Hörst, 2017) and possibly sedimentary deposits (Lunine et al., 2008) (Hörst, 2017).

On a study of Hörst et al., 2012, the conditions of the upper atmosphere of Titan have been replicated in laboratory (with enhanced CO levels), resulting in the production of all 5 nitrogenous nucleotide bases that comprise all of Earth's living organisms genetic code (in RNA and DNA molecules): Cytosine ($C_4H_5N_3O$), Uracil ($C_4H_4N_2O_2$), Thymine ($C_5H_6N_2O_2$), Guanine ($C_5H_5N_5O$), and Adenine ($C_5H_5N_5O$). Two of the simplest amino acids most widely used by all terrestrial life-forms, were produced, Glycine ($C_2H_5NO_2$) and Alanine ($C_3H_7NO_2$) (Hörst et al., 2012). Another study has shown that high-velocity impacts could spark the synthesis of amino acids on icy worlds' surfaces (Z. Martins et al., 2013).

Amino acid molecules are organic molecules characterised by containing a amine group (-NH_2) and a carboxyl group (-COOH) connected by a Carbon atom, referred to as the α-Carbon. Amino acids are distinguished by structure of their side chain which is also connected to the α-Carbon (Atkins et al., 2013). These biomolecules are fundamental to all life forms on Earth, as these are the building blocks of the proteins present in all living beings on Earth (Z. Martins et al., 2013). Hence, the question of how individual bio-molecules such as these, potentially produced in Titan's atmosphere, interact with the water ice matrix of Titan's solid surface was raised. Are these bio-molecules destroyed, preserved, or adsorbed? Could the interaction with the icy surface act as a catalyst for new, more complex, pre-biotic chemistry?

Alongside experimental laboratory work, molecular dynamics simulations provide a useful way to test how molecules interact with each other and with a surface matrix, allowing a meaningful and complementary comparison to laboratory experiments. In particular, I am integrated in a IST-CQE research group conducting laboratory work that simulates UV (Ultraviolet) irradiation of amino acids (in particular, Glycine ($C_2H_5NO_2$, Gly), Alanine ($C_3H_7NO_2$, Ala), and α-Aminobutyric acid, ($C_4H_9NO_2$, AABA), displayed in figure 1.6) on ice matrices under Titan conditions. Hence, another goal of this masters thesis project is to run Atomistic Molecular Dynamics Simulations (AMDS) to model these amino acid films structure and interactions under Titan conditions, to be compared with laboratory work results. The end goal here, would be to draw some conclusions or possible explanations for the new results observed during the complementary experimental work. Following Gómez-Zavaglia et al., 2003 and (Minkov et al., 2010), it is expected that on Titan's surface conditions (100K and 1,4bar) these amino acids acquire and preserve a zwitterionic form, whereby the proton attached to the carboxyl group is transferred to the amine group. This causes the amino acid molecule to contain positive (NH_3^+) and negative ions (COO^-) (Atkins et al., 2013), while remaining net neutral, as shown on the amino acid structures of figure 1.6.

The experimental work that serves as the main motivation for the molecular dynamics simulations can be briefly described as a follow-up study of amino acid photostability under Titan's surface conditions, following the example of UV-irradiation photostability studies of amino acids in space and planetary environments (Ehrenfreund et al., 2001) (Poch et al., 2013) (Poggiali et al., 2020). In this case, an experimental setup was prepared to conduct a similar type of photostability studies for possible amino acids deposited and buried on Titan's Ice Surface.

1. INTRODUCTION

During this master thesis work, atomistic molecular dynamics simulations of these thin amino acid films were run. Their goal was to study these film's simulated structure and probe the intermolecular forces between the different amino acids at play here, complementing the laboratory work and aiming to answer the following questions:

1. How different are the structures and interactions between molecules in pure film samples of these amino acids? Can different conformations and intermolecular forces provide an indication of relative photostability of glycine, alanine and α-aminobutyric acid when independently irradiated?

2. How do the studied amino acid molecules interact within a mixture film? Can this interaction between distinct molecules affect the amino acid's photostability when present in an amino acid mixture?

Understanding interactions within amino acid films with Molecular Dynamics Simulations under Titan-like conditions will allow not only to answer these questions, but also help constraining the potential for detectability of these bio-molecules species in the organic sediments we expect to be abundant at the surface of Titan - a study that is particularly relevant in the context of the development of NASA's future Dragonfly mission to Titan (Barnes et al., 2021), aimed precisely at detecting and characterising the chemical evolution and the fate of photochemically generated organic molecules on Titan's icy surface.

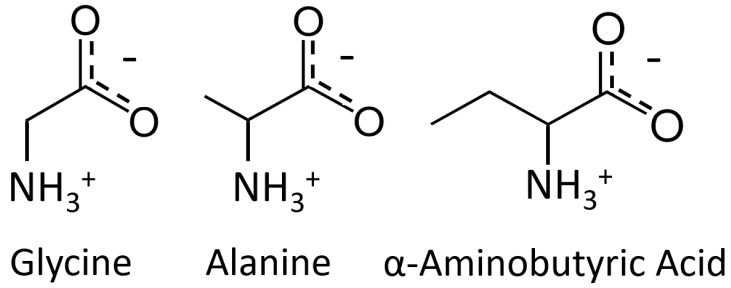

Figure 1.6: Molecular structure of the 3 amino acids of interest considered in this study, on their zwitterionic form. From left to right, Glycine ($C_2H_5NO_2$), Alanine ($C_3H_7NO_2$) and α-Aminobutyric Acid ($C_4H_9NO_2$). It is worth noticing that they are structurally similar, except for the variable chain, which grows as a saturated Carbon chain from being a single H atom (Glycine), to a single -CH_3 methyl group (Alanine), to a -C_2H_5 ethyl group (α-Aminobutyric Acid).

Chapter 2

Observational Data

2.1 The Instrument: Ultraviolet-Visible Echelle Spectrograph (UVES)

As mentioned in section 1.1, space missions to study solar system targets are fundamental to understand their nature and temporal evolution, in particular through high spatial resolution imaging and *in situ* spectroscopic studies (Coustenis et al., 2007) (Encrenaz et al., 2010) (Hörst, 2017) (Barnes et al., 2021). There are also, nonetheless, great advantages in the use of ground-based observatories in the study of planetary atmospheres within our solar system, in particular in the context of the very complementary information provided by High Resolution Spectroscopy (Encrenaz et al., 2010). Space telescopes or space missions, take advantage of the absence of the contamination of the Earth's atmosphere while observing targets in space (Tinetti et al., 2018) (Rigby et al., 2023). However, in order to retrieve spectra at high spectral resolutions, the stability that ground-based instruments provide is unmatched and key for high dispersion spectroscopy (Dekker et al., 2000) (Pepe et al., 2021). Furthermore, ground-based observatories present far less engineering challenges than space-based observatories, which allows the development of telescopes with much larger collecting areas, which is also key to increase Signal-to-Noise ratio (SNR) in high resolution spectroscopic observations (Dekker et al., 2000) (Pepe et al., 2021).

High resolution spectral observations are highly complementary to low resolution, space-based/*in situ* low resolution observations of planetary atmospheres, as while low-resolution spectral observations are able to constrain the general composition and structure of a planetary atmosphere (through the detection of broad molecular absorption bands or scattering effects) (Encrenaz et al., 2010) (Tinetti et al., 2018), high-resolution spectra can provide more detailed information about these atmospheres. This includes the search for trace compounds or isotopes molecular transition lines (only discernible at high resolution) (Lombardo et al., 2019) (Dias et al., 2022) or the retrieval of atmospheric dynamics by tracking the Doppler shift in backscattered solar absorption lines (also only traceable at high resolution) (Machado et al., 2014). For reference, James Webb Space telescope, mid-resolution NIRSpec spectrograph is able to reach resolving powers ($R = \lambda/\Delta\lambda$) up to 2000 (Gialluca et al., 2021), whereas high resolution ground-based spectrographs such as UVES are able to reach spectral resolutions up to 100.000 (Dekker et al., 2000) (Sbordone et al., 2023).

Since our aim here was to conduct a High Resolution Study of Titan's atmosphere in visible wavelengths, we resorted to archived data and dedicated observations of Titan at visible wavelengths with the European Southern Observatory (ESO) Very Large Telescope (VLT) UVES instrument, located at the Nasmyth B focus of Unit Telescope 2 of VLT (with 8,2m of diameter), at the Paranal Site, in the Chilean Atacama desert (Dekker et al., 2000). UVES stands for UV-Visible Echelle Spectrograph, describing not only the instrument's wavelength coverage, but also its dispersing component, a cross-dispersed echel-

logram. This element allows the collected light (entering the instrument through a variable width slit) to be cross-dispersed in very high resolution onto 2 instrumental arms - at the end of which stands a detector designed to collect light at each arm's wavelength range. The blue arm covers the wavelength range from 300 nm to 500 nm with maximum resolution ($\lambda/\Delta\lambda$) of 80.000, whereas the detector's red arm is designed to cover the wavelengths 500 nm to 1100 nm with maximum resolution ($\lambda/\Delta\lambda$) of 110.000. Each detector however, can only cover a wavelength range of up to 200nm for each observation (Dekker et al., 2000) (Sbordone et al., 2023). An illustration of a similar optical path to the one existing in VLT/UVES is shown in figure 2.1, from the newer generation VLT/ESPRESSO instrument (Pepe et al., 2021).

The instrument's resolution is highly dependent on the size of the slit used in the observations: smaller slit widths imply a higher spectral resolution (Dekker et al., 2000) (Sbordone et al., 2023), dropping from close to $\lambda/\Delta\lambda = 100.000$ at 0,3" slits to $\lambda/\Delta\lambda = 60.000$ at 0,7" width slits. This increased resolution at lower slit sizes comes with a trade-off of reducing the amount of light collected by the detector at a given observation time, implying higher exposure times in order to retrieve the same SNR (Sbordone et al., 2023).

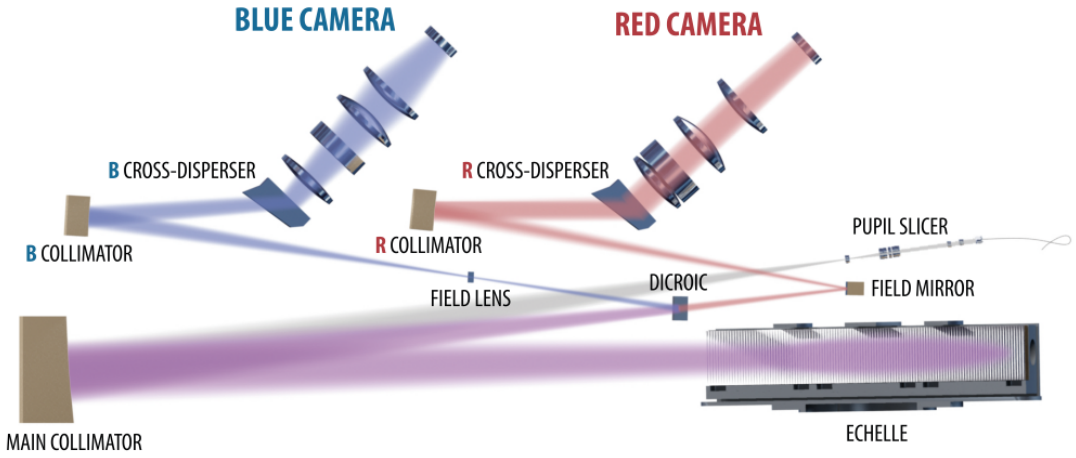

Figure 2.1: Schematic representation of an echelle spectrograph optical path (from VLT/ESPRESSO as described in Pepe et al., 2021), a similar design to the one used by VLT/UVES (Dekker et al., 2000) (Sbordone et al., 2023). It is worth noticing how the collected light can be split into 2 detector arms (blue and red), each directed to its own detector.

2.2 The Data: 2 High-Resolution Visible observation campaigns of Titan's Atmosphere

Dedicated observations of Titan with the Blue Arm of the UVES instrument at the 8.2m Unit 2 Telescope of the Very Large Telescope (VLT) (Dekker et al., 2000) were obtained on the night of 21/06/2018. A set of 22 science exposures of Titan were obtained in this night, with 400s of exposure each - alongside a set of calibration exposures throughout the night. The observations were conducted with a seeing limit of 0,80" and an instrument slit width of 0,7", implying a spectral Resolving power of $R \approx 60.000$ (Dekker et al., 2000) (Sbordone et al., 2023).

These observations were complemented in this study with archived observations (obtained through ESO's Science Archive) with the Red Arm of the same instrument from Luz et al., 2006 in 4 nights of January 2005, conducted with a seeing limit of 0,80". A total of 34 with exposures of 500s each was obtained during the 4 observations nights during the 2005 campaign (Luz et al., 2006). Since Titan's

apparent diameter was of 0,78" in the 2018 campaign and of 0,88" in the 2005 campaign (about the angular size of these night's seeing), we are limited in these observations to disk-averaged spectra. Still, due to the lower instrument width of 0,3", these VLT/UVES Red Arm 2005 observations should imply a spectral resolving power of $R \approx 100.000$ (Dekker et al., 2000) (Sbordone et al., 2023). Table 2.1 summarises some characteristics of the spectral observations of Titan used in this study, divided in 2005 UVES Red arm spectra (5200Å to 6200Å), (Luz et al., 2006) and 2018 UVES Blue arm spectra (3800Å to 4800Å), both with a wavelength spacing between 2 spectral bins of 0,015 Å. The wavelength intervals probed by each instrument arm are superimposed on a low resolution spectrum of Titan's atmosphere from McKay et al., 2001 on figure 2.2.

Table 2.1: VLT/UVES Observations of Titan used in the context of this work. The first rows corresponds to the ones obtained in 2005 by Luz et al., 2006 using UVES Red arm (5200Å to 6200Å), while the last row accounts for the dedicated observations of Titan with UVES Blue arm (3800Å to 4800Å). Titan-Earth and Titan-Sun Radial Velocity (RV) values were retrieved from NASA/JPL HORIZONS ephemeris calculator. Redshift of solar lines with respect to the solar rest frame on each spectrum, at Titan's rest frame were considered at 5000Å for Red arm observations and at 4000Å for Blue arm observations.

Date	Exposures	Titan-Earth RV (m/s)	Titan-Sun RV (m/s)	Solar Redshift (mÅ)
08/01/2005	8 (Red arm)	+4710 $\pm$ 30	-1500 $\pm$ 50	-25 $\pm$ 1
13/01/2005	9 (Red arm)	-4180 $\pm$ 120	-3740 $\pm$ 20	-62 $\pm$ 1
15/01/2005	8 (Red arm)	-610 $\pm$ 130	-160 $\pm$ 50	-3 $\pm$ 1
16/01/2005	9 (Red arm)	+3240 $\pm$ 160	+1920 $\pm$ 60	+32 $\pm$ 1
21/06/2018	22 (Blue arm)	+1040 $\pm$ 240	+4140 $\pm$ 70	+56 $\pm$ 1

A set of important information regarding these observations also shown on table 2.1 regards the relative radial velocity between Earth and Titan and Titan and the Sun at the time of each of the observations. As we intend to observe Titan absorption lines on their rest frame, it is key to correct the Doppler shift with which the spectrum of Titan reaches the observatory on Earth, due to the relative velocity between the 2 bodies (Luz et al., 2006). At the same time, the distinct Radial Velocity between Titan and the Sun is reflected upon the backscattered solar spectrum that constitutes the baseline of Titan's spectrum at optical wavelengths (Machado et al., 2014). Distinct solar redshifts cause solar absorption lines to move over different nights with respect to fixed rest-frame absorption lines of molecules on Titan's atmosphere. As we shall see below and in section 3.2, this variable solar redshift over observation nights presents both a challenge and a silver bullet for probing Titan's high resolution spectrum.

2.2.1 Observational Data Reduction: IA's High-Resolution Spectroscopy Pipeline

The data collected by the observatories is not ready to be analysed for science. A set of data processing steps are required to transform the data leaving the instrument into science spectra that can then be analysed. These VLT/UVES observations were therefore processed from its raw form (which was downloaded from ESO Science Archive, alongside the flat and dark exposures required to process the raw telescope data) using ESOReflex pipeline for VLT/UVES spectra. Each exposure is processed individually, following bias and dark removal as well as flat-fielding, as described in Luz et al., 2006. This process also allowed the flux and wavelength calibration based on the instrument's Th-Ar lamp exposures. This implies that rather than having fluxes and wavelengths measured in arbitrary detector units, these fluxes and wavelengths are now presented in physical units - wavelengths in units of Angstrom (Å)

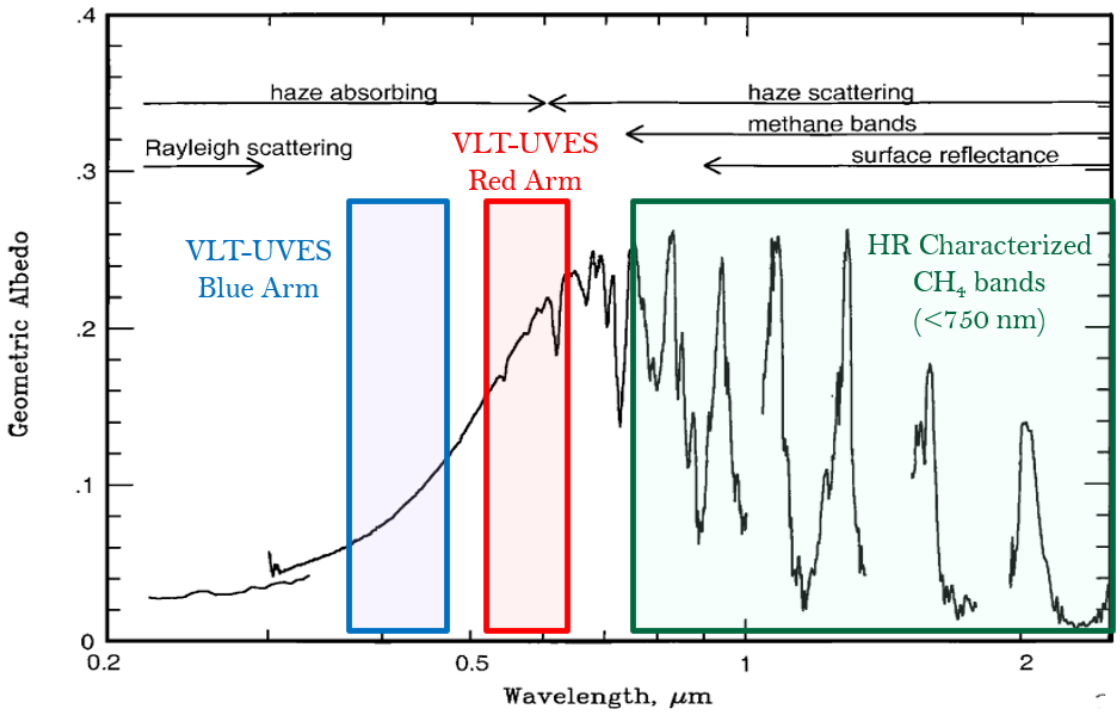

Figure 2.2: Low Resolution visible and Near IR Spectrum of Titan from McKay et al., 2001 with the indication of the main sources of opacity at each wavelength on Titan's atmosphere. Indication of the spectral regions of interest for this study: shaded in green, the lower wavelength limit of methane absorption bands already characterised at high resolution (HR) above 7500 Å. Shaded in Blue is the region of Titan's spectrum probed by the Blue arm VLT/UVES dedicated observations of the 2018 campaign (3800Å to 4800Å), which includes the 4051Å region where the C_3 band will be searched for. Shaded in Red is the region of Titan's spectrum probed by Luz et al., 2006 observation of Titan with VLT/UVES Red Arm (5200Å to 6200Å), including 4 weak uncharacterised CH_4 absorption bands.

and flux density units of erg.s^{-1}.cm^{-2}.Å^{-1} units.

As mentioned above, the high resolution VLT/UVES is an echelle spectrograph, which implies that its dispersing element, the echellogram, splits the spectrum into an array of spectral orders (Dekker et al., 2000). The distinct spectral orders obtained in each UVES echellogram exposure were combined into 2 2-D spectra of Titan, with both flux and flux error values associated, for each exposure. One of the matrix's axis (corresponding to the dispersion direction, alongside the slit's width) is associated with the wavelength axis. In the other direction, alongside the slit's length, each pixel corresponds to a distinct spacial position in the sky, with the edges showing background sky and the centre showcasing the disk of Titan, as is shown on figure 2.3. The EsoReflex interface outputted 2 such 2D spectral files per exposure: on one, the 2D matrix entry value corresponded to the detected spectral flux density per detector pixel (in erg.s^{-1}.cm^{-2}.Å^{-1} units). The other 2D spectrum outputted per exposure corresponded to the detector's error values per pixel, in the same spectral flux density units.

Up to here, the spectral processing was mostly automatic within the EsoReflex interface. However, to move from a 2D spectrum of Titan per exposure to a single science spectrum, I adapted the IA's High Resolution Spectroscopy Pipeline (a series of MATLAB-based codes) to these flux calibrated Titan spectra. The first step from here was to obtain a 1D spectrum per exposure - which implies removing the spatial dimension on these 2D spectral images. To do so, I obtained a disk-averaged spectrum of Titan by averaging the spectra that covered Titan's disk. With a pixel scale of 0,25" in the 2018 Titan observations, the disk of Titan covered about 3 pixels in the spacial direction of the 2D spectrum. Hence, a disk-integrated spectrum was obtained for the 2018 observations by averaging the 3 spectra covering the disk of Titan. Similarly, with a pixel scale of 0,18", disk-integrated spectra of 2005 observations implied

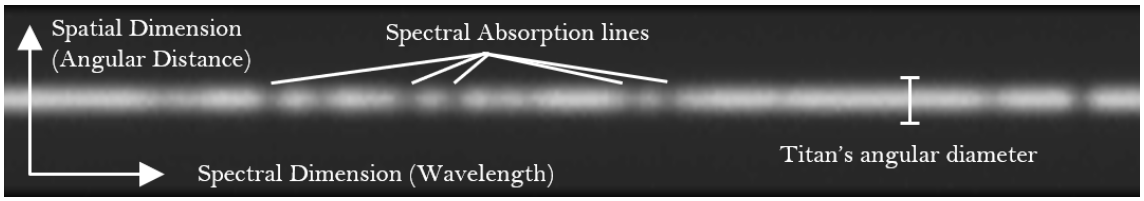

Figure 2.3: Section of a 2D VLT/UVES Spectrum of Titan from the 2018 observation campaign. A brighter colour corresponds to a higher flux density upon each pixel of the detector. Schematic representation of the 2 distinct dimensions in such a 2D spectrum: a spectral dimension (horizontal) upon which wavelength varies, and a spatial dimension (vertical) upon which the angular position in the sky varies. Thus, the bright horizontal stripe corresponds to the image of Titan observed at distinct wavelengths, and its vertical width corresponds to Titan's angular diameter in the sky. The darker sections of this bright stripe correspond to wavelengths where Titan's outgoing spectral flux is weaker: absorption lines on its spectrum.

averaging the 5 central spectra of the 2D spectrum that covered the entirety of disk of Titan. For each observation night, all disk-integrated exposures were also averaged into one single 1D disk-integrated spectrum of Titan per observation night.

Since each observation night corresponds to a distinct average radial velocity between the Earth and Titan (3rd column of table 2.1), a distinct Doppler shift correction was applied to each night's averaged 1D spectrum, correcting these spectra to the rest frame of Titan (rest-frame wavelength defined as λ_0) as a function of the radial velocity between these objects v_r, following equations 2.1.

$$\Delta\lambda = \lambda - \lambda_0 = \lambda_0 \frac{v_r}{c} \qquad\qquad \lambda = \lambda_0 \left(1 + \frac{v_r}{c}\right) \tag{2.1}$$

Unlike the 2005 Red arm observations, all of the 2018 Blue arm exposures were taken during the same night. This causes its processing and usage to be far more straightforward, since all the previously mentioned calibration steps can be conducted simultaneously for consecutive exposures within the same observation. Exposures taken in distinct observation nights, as those obtained in the 2005 campaign, require, however, independent calibration. Thus, we are left with 5 disk and night averaged visible spectra of Titan, Doppler shifted to Titan's rest frame: 1 spectrum combining all 2018 VLT/UVES Blue arm observations and 4 2005 VLT/UVES Red arm spectra, one per each observation night.

Due to the distinct radial velocities between the Sun and Titan on the distinct observation nights (4th column of Table 2.1), distinct Doppler shifts are observed in the solar absorption lines present on Titan's visible spectra (5th column of Table 2.1). This prevents us from combining nightly spectra into a single spectrum with increased signal to noise ratio (SNR), since solar absorption features appear significantly shifted with respect to each other (figures 4.2 and 4.3). However, as we describe in section 3.2 this distinct Doppler shift in solar lines over spectra obtained on several observing nights can actually present an advantage in line characterisation of visible spectra of planetary atmospheres.

Chapter 3

Methods and Tools

3.1 The Theory of Radiative Transfer

After processing and calibrating the spectral data obtained from astrophysical observations of planetary atmospheres, we are left with a science spectrum that can be interpreted using the knowledge of the nature of the physical processes shaping the interaction of electromagnetic radiation with the constituent particles in a planetary atmosphere (Sánchez-Lavega, 2011). Taking advantage of this theoretical knowledge of how light interacts with matter within a planetary atmosphere, we can produce synthetic, model spectra that can be compared with the observational spectra and provide a physical interpretation of the observed features present on the spectrum of a planetary atmosphere (Hanel et al., 2003) (Encrenaz et al., 2010).

3.1.1 The Equation of Radiative Transfer

The first step to understand the interaction between light and matter is through the study of the theory of radiative transfer, which I will briefly summarise here following Sánchez-Lavega, 2011. Let us picture electromagnetic radiation crossing an infinitesimal element of surface dS at an angle ϕ during an infinitesimal timestep dt, propagating into an infinitesimal solid angle $d\Omega$. The amount of energy crossing this differential surface within a frequency interval $d\nu$ is given by

$$dE_\nu = I_\nu \cos(\phi)\, dS\, dt\, d\Omega\, d\nu \tag{3.1}$$

I_ν is defined as "Specific Intensity" in SI units of J.s^{-1}.m^{-2}.str^{-1}.Hz^{-1}. An equivalent definition as I_λ is possible by replacing differential frequency interval, $d\nu$, by a differential wavelength interval, $d\lambda$. Integrating this specific intensity over a finite solid angle of sky, say, by obtaining a disk-integrated observation of a resolved source on the sky we obtain a Flux Density, F_ν:

$$F_\nu = \int_{\Omega\ source} I_\nu \cos(\phi)\, d\Omega \tag{3.2}$$

The calibrated value obtained by the spectrograph's detector shown in the previous chapter is indeed a disk-integrated flux density in the form of F_λ, but in erg.s^{-1}.cm^{-2}.Å^{-1} units rather than SI units. As mentioned above, the fundamental question behind the theory of radiative transfer is *how does the specific intensity of a radiation beam vary as it crosses matter?* A general approach to this question is to describe the differential of the specific intensity dI_ν along an infinitesimal path ($d\ell$) as the sum of processes that add to the radiation field propagating in that direction (emission of radiation in the $d\vec{\ell}$

direction) subtracted by the set of processes that remove energy from the radiation field propagating on the $d\vec{\ell}$ direction (such as absorption of radiation by the medium, as well as scattering of radiation towards other directions). This general approach can be summarised by the following equation, **The Equation of Radiative Transfer**:

$$\frac{dI_\nu}{d\ell} = j_\nu \rho - I_\nu \alpha_\nu \rho \text{ , with } \alpha_\nu = k_\nu + \sigma_\nu^{scattering} \tag{3.3}$$

Here, the emission component is defined as a mass emission coefficient (j_ν) multiplied by the mass density of the medium (ρ). At the same time, the mass absorption coefficient (α_ν) can be divided into scattering ($\sigma_\nu^{scattering}$) and "real" absorption by the gas phase medium (k_ν) mass coefficients (Sánchez-Lavega, 2011) (Hanel et al., 2003). These mass emission and absorption coefficients have units of distance^2 over mass. It is also possible to define absorption coefficients based on the number density of molecules of interest (known to absorb strongly at the wavelengths of interest) within the medium. In that case, rather than having these quantities (with units of distance^2 per molecule) multiplied by the mass density of the medium, they are multiplied by the number density of absorbing molecules within the medium (Sánchez-Lavega, 2011). We will represent the number-density based absorption coefficient by σ_ν^{abs}. As we shall see ahead in section 3.1.2 this is useful when considering the line absorption by molecules within an atmosphere.

It can be argued that all solar system planet's spectra can be divided into 2 components: given that solar system planets effective temperatures are scattered around a few hundred K, these planets' Blackbody emission peaks at thermal infrared wavelengths (roughly between 10 μm and 100 μm) (Sánchez-Lavega, 2011) (Hanel et al., 2003). This is the planetary thermal, long-wavelength emission spectrum. However, planets also backscatter some of the solar radiation they receive, which given the Sun's much higher surface temperature (of about 5700K), centres this Blackbody curve at far shorter wavelengths, between 300 nm to 3 μm, covering the visible and near Infrared (NIR) sections of the electromagnetic spectrum. All planets backscatter a fraction of this incoming solar spectrum - the short wavelength component of their spectrum. On it, planetary atmospheres and surfaces imprint not only the scattering coefficients of their distinct surfaces/hazes/clouds but also the characteristic absorption bands of gases within their atmospheres (Sánchez-Lavega, 2011) (Hanel et al., 2003).

In this work we are particularly focused on Titan's outgoing, short-wavelength (visible) spectrum, where emission features are, for the most part, negligible (Sánchez-Lavega, 2011). Considering therefore an approximation to a purely absorbing atmosphere, we can define a dimensionless quantity named the **optical depth**, τ_ν as the integral of the absorption coefficient $\alpha_\nu \rho$ along a path of light ℓ:

$$\tau_\nu = \int_\ell d\tau_\nu = \int_\ell \alpha_\nu(\ell)\rho(\ell)d\ell \tag{3.4}$$

The optical depth varies with wavelength and is a relevant scale of how much absorption occurs within a medium. For $\tau_\nu \ll 1$, we have an optically thin medium, where absorption of light is slight. For $\tau_\nu \approx 1$ or above, the medium is considered optically thick, since a great degree of absorption occurs. This definition can be used to rewrite the radiative transfer equation (eq. 3.3) on the purely absorbing medium case as follows:

$$\frac{dI_\nu}{d\tau_\nu} = -I_\nu \quad \text{which implies that} \quad I_\nu(\tau'_\nu) = I(\tau_\nu = 0)e^{-\tau'_\nu} \tag{3.5}$$

This equation has a simple solution form as a specific intensity that exponentially decreases with optical depth. This negative exponential of the optical depth factor, the factor by which spectral intensity

decreases as light travels through a medium is defined as the **Transmittance** of a medium, T_ν or T_λ. However, for the case of an external observer looking at a planetary atmosphere such as Titan's, what we see in visible wavelengths is the solar radiation that was backscattered at a an altitude on Titan's atmosphere where (due to haze scattering) it becomes optically thick (Sánchez-Lavega, 2011).

The intensity of absorption across the path of light, is dependent not only on the intrinsic absorption strength of each molecule, but also on the density of molecules in the medium crossed by light on its path along the atmosphere (Sánchez-Lavega, 2011). A key quantity that can be defined here is the **Column Density,** N, that, generally, corresponds to the integral of the molecular number density (n, with units of molecules per volume) along the direction of the path of light ($d\ell$), as shown in eq. 3.6, (with units molecules . distance^{-2}). This physical quantity can be further defined as a pathlength down from the top of a planetary down to the level of the atmosphere where it becomes optically thick, considering the spherical nature of a planetary atmosphere, on equation 3.21 (Lellouch et al., 2022).

$$N = \int n \cdot d\ell \tag{3.6}$$

The radius of a planet at which its atmosphere becomes optically thick is called its **optical radius** (Lorenz et al., 1999). Hence, the outgoing spectrum of Titan in visible wavelengths is affected by the wavelength-dependent albedo of the backscattering process happening at Titan's optical radius, and by the radiation absorption that occurs at the atmosphere layers above the optical radius. Thus, we can generically describe Titan's visible spectrum (I_ν) as the product of the incoming solar radiation ($I_{\nu,0}$) with the planetary, disk-integrated albedo at Titan's optical radius (A_ν) with the Transmission factor ($T_\nu = e^{-3\tau_\nu}$) caused by the optical absorption caused by haze and molecular species on the column of Titan's atmosphere crossed by light above its optical radius - as is shown on equation 3.7

$$I_\nu = I_{\nu,0} \; . \; A_\nu \; . \; e^{-3\tau_\nu} \tag{3.7}$$

The optical depth included in equation 3.7 is the one-way optical depth of Titan's atmosphere, from the edge of space down to Titan's optical radius. In order to account for the effect of both the downward and upward paths of the solar radiation across Titan's atmosphere, it would be reasonable to multiply by 2 this one-way optical depth. However, due to to the disk-integrated nature of this observation and the inherent geometrical corrections, it can be demonstrated that a factor of 3 is actually a better correction for this effect (Lellouch et al., 2022), hence its inclusion on equation 3.7.

3.1.2 Molecular absorption lines from first principles

The brief introduction to radiative transfer presented above describes it in a general way - such that the opacity that increases the optical depth within a medium could be produced by any kind of absorption mechanism. In the context of the search for high resolution molecular lines on Titan's atmosphere in visible wavelengths, it is key to understand how molecular transitions between energy states become sources of opacity within a planetary atmosphere.

We shall take as a starting point the physics of molecular ro-vibrational bands. Atoms within molecules are held by effective electrostatic potentials whereupon these vibrate and rotate - at the specific energies allowed by their quantum oscillator nature. Molecules absorb energy quanta as photons with the wavelength associated with the energy difference that is required to transition between distinct rotational or vibrational levels (Robinson, 1996) (Sánchez-Lavega, 2011). Independently, this set of allowed transitions between energy states produces the NIR to mid-Infrared vibrational molecular bands whose

energy levels can be described by eq. 3.8, as a function of the molecular bond's oscillator constant (K) and its reduced mass (μ_M). To these bands we must add the less energetic far-infrared to sub-mm rotational molecular bands that are described by eq. 3.9 as a function of their quantum number for angular momentum, J, and inertia moment of the system, I, (Sánchez-Lavega, 2011).

$$E_n = \hbar \sqrt{\frac{K}{\mu_M}} \left(n + \frac{1}{2}\right), \qquad \text{for } n = 0, 1, 2, ... \tag{3.8}$$

$$E_J = \frac{\hbar^2}{2I} J(J+1), \qquad \text{for } J = 0, 1, 2, ... \tag{3.9}$$

However, when the absorption of higher energy photons (such as those in visible wavelengths) allows the excitation of molecular electronic cloud electrons into more energetic electronic levels, the far less energetic vibrational and rotational transitions can be simultaneously excited, producing a combination called the ro-vibrational spectrum of a molecule, as seen in figure 3.1.

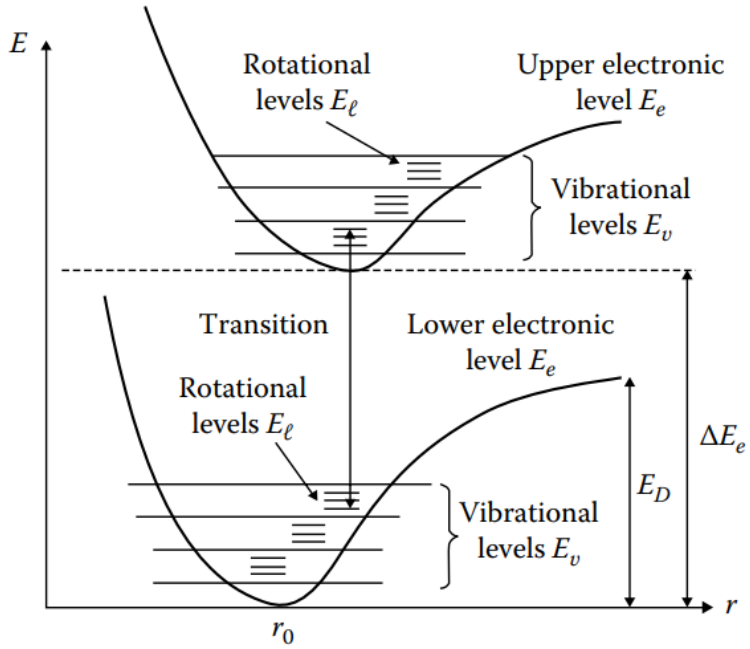

Figure 3.1: Ro-vibrational transition within a molecule as it undergoes a transition between electronic levels that also allows the simultaneous transition between less energetically demanding rotational and vibrational levels within a molecule. From (Sánchez-Lavega, 2011).

These transitions will create more complex molecular bands on visible frequencies associated with the sum of 3 transition energies as seen on eq. 3.10, whose transition frequencies, $\nu_{e,n,J}$, will scatter around the frequency associated to the energy of the pure electronic transition (ν_e).

$$\nu_{e,n,J} = \frac{\Delta E}{h} = \frac{\Delta E_e + \Delta E_n + \Delta E_J}{h} = \nu_e + \nu_n(n \to n') + \nu_J(J \to J') \tag{3.10}$$

The inner structure of these ro-vibrational molecular bands strongly depend on the symmetry of the molecule, but can generally be divided into several peaks (branches) based on the variation of the quantum number of angular moment, J: $\Delta J = 0$ transitions belong to the Q branch of the molecular band, $\Delta J = -1$ transitions belong to the P branch and $\Delta J = +1$ transitions to the R branch (Sánchez-Lavega, 2011).

How do we quantify the amount of energy absorbed by such a molecular transition? The degree of absorption by a given molecular line transition can be expressed by the integral of the absorption coefficient over the frequency (or wavelength) range in which the line transition occurs (Robinson, 1996). Due to the uncertainty principle of quantum physics, electronic transitions such as these do not occur at a single frequency, but rather in a short frequency range that can be broadened by several effects as we shall see (Robinson, 1996). Let us consider the integral in frequency (or wavelength) over a molecular transition of the number density-based absorption coefficient (σ_v^{abs}), a quantity which we shall call line strength (S_i) (Sánchez-Lavega, 2011). It can be proven that (following a comparison with a classical damped oscillator) the line strength of molecular transition is given by equation 3.11

$$S_i = \int_0^\infty \sigma_i(\lambda) d\lambda = \frac{e^2 \lambda_0^2}{4 m_e c^2 \varepsilon_0} . \mathrm{pop}(J) . f_J \tag{3.11}$$

Here, λ_0 is the central wavelength of the molecular line, e and m_e the charge and mass of the electron (respectively), c the speed of light, and ε_0 the vacuum permittivity. f_J denotes the oscillator strength, a key dimensionless quantity in molecular physics that determines the relative strength of each individual absorption line. Considering the usual distance^2 per molecule units of the absorption (cross-section) wavelength-based coefficient, wavelength-based line strength S_i shall have units of distance^3 per molecule. Wavenumber-based line strength shall have, on the contrary, distance per molecule units. It also is worth noticing that for wavelength-based measurements absorption coefficients' units are the inverse of column density units, whereas Line strength units are the inverse of molecular number density units.

The other relevant factor coming into play in this equation is pop (J). This is the population distribution function of angular momentum (J) states of a molecule at a temperature T, and is given, in 1st order approximation, by eq. 3.12. Here, k_B is the Boltzmann constant and B the rotational constant of the molecule (Tanabashi et al., 2005). For the case of the C_3 molecule, which shall be our case study here, $B = 0,431$ cm^{-1}, as obtained by Tanabashi et al., 2005.

$$\mathrm{pop}(J) = (2J+1) \exp\left[-\frac{hcBJ(J+1)}{k_B T} \right] \tag{3.12}$$

As mentioned above, line absorption in molecular bands occurs at a small wavelength range rather than at a specific wavelength. This implies a line profile, which defines the shape of the absorption line within a spectrum. The shape of an absorption line can vary according to the environment in which the absorption (or emission) is taking place. Due to the effect of pressure within a gaseous medium, a spectral line can be broadened, with the absorption coefficient dependence on wavelength maintaining its Lorentzian shape around central wavelength λ_0 given by 3.13, such that the integral in wavelength of this quantity along the entire line is equal to the line strength (Sánchez-Lavega, 2011). γ_L expresses the half width at half maximum (HWHM) of this lorentzian absorption line, which is dependent on pressure P and temperature T as $\gamma_L \propto P.T^{-1/2}$

$$\sigma_i(\lambda) = \frac{\gamma_L . S_i}{\pi \left[(\lambda - \lambda_0)^2 + \gamma_L^2 \right]} \tag{3.13}$$

However, in other environments, temperature may become a predominant effect altering the shape of spectral lines. This is due to the thermal agitation of molecules within a warm gas, which with an increased velocity dispersion causes significant Doppler shifts the wavelengths of some of the emitted or absorbed photons (Sánchez-Lavega, 2011). This effect (Doppler broadening of spectral lines) changes

line shapes towards a Gaussian-shaped line, as described by eq. 3.14:

$$\sigma_i(\lambda) = \frac{S_i}{\gamma_D\sqrt{\pi}} \exp\left[-\left(\frac{\lambda-\lambda_0}{\gamma_D}\right)^2\right] \tag{3.14}$$

The full width at half maximum (FWHM) of such a Doppler broadened line is related to the factor γ_D and dependent on the temperature of the gas in the absorbing/emitting medium (Sánchez-Lavega, 2011) following the relation in equation 3.15.

$$\text{FWHM} = 2\gamma_D\sqrt{\ln 2} = \frac{2\lambda_0}{c}\sqrt{\frac{2k_BT\ln 2}{m}} \tag{3.15}$$

Thanks to this set of relations, we can write the profile of the optical depth of an absorption line ($\tau_i(\lambda)$) from as shown in eq. 3.16. This equation is obtained by writing equation 3.4 while swapping the mass absorption coefficient (and mass density) by the absorption coefficient per molecule (and molecular number density, $n(\ell)$) along the light path ℓ. For an absorption coefficient of a single molecule of interest, $\sigma_i(\lambda)$, assumed constant along the light path, we can remove it from the path integral - which is now equal to the column density of the absorbing molecule along the light path.

$$\tau_i(\lambda) = \sigma_i(\lambda)\int_\ell n(\ell)d\ell = \sigma_i(\lambda)N = \frac{S_iN}{\gamma_D\sqrt{\pi}} \exp\left[-\left(\frac{\lambda-\lambda_0}{\gamma_D}\right)^2\right] \tag{3.16}$$

Following the definition of Transmittance of an absorption line ($T_i(\lambda)$) above, on eq. 3.7, we can express the total transmittance function of an absorption band, $T(\lambda)$ or T_λ, as the product of the individual transmission profile of all absorption lines according to eq. 3.17.

$$T(\lambda) = \prod_i T_i(\lambda) = \prod_i e^{-3\tau_i(\lambda)} = \prod_i e^{-3N\sigma_i(\lambda)} \tag{3.17}$$

One last fundamental definition for the study of high resolution spectral lines on a planetary atmosphere is the **Equivalent Width** (EW) of an absorption spectral line. This quantity is a measure of the relative intensity (which can be described by the Transmission profile, T_λ of a spectral absorption line) removed from the spectral continuum by the absorption line, given by eq. 3.18. Geometrically, it is equivalent to the width of a rectangle of spectral continuum with an area equal to that of the absorption line (Sánchez-Lavega, 2011). EW has wavelength (nm or Å) units for wavelength-represented spectra (and wavenumber or frequency units for spectra represented in those units).

$$\text{EW} = \int_0^\infty \left(1 - \frac{I_\lambda}{I_0}\right) d\lambda = \int_0^\infty (1 - T_i(\lambda))\, d\lambda \tag{3.18}$$

Replacing $T_i(\lambda)$ by the expression for the disk-integrated radiative field attenuation of a planetary atmosphere, backscattered from its optical radius (eq. 3.7, where $T_\lambda = e^{-3\tau_\lambda}$) we obtain the equivalent width of a spectral absorption line from a disk-integrated spectrum of a planetary atmosphere. For the optically thin ($\tau_\lambda << 1$) case, it is possible to apply a Taylor series approximation ($e^x \approx 1+x \Rightarrow e^{-3\tau_\lambda} \approx 1-3\tau_\lambda$), leading to eq. 3.19 (Sánchez-Lavega, 2011).

$$\text{EW} = \int_0^\infty \left(1 - e^{-3\tau_\lambda}\right) d\lambda \quad \Rightarrow \quad \text{EW} = \int_0^\infty 3\tau_\lambda\, d\lambda \quad (\text{for } \tau_\lambda << 1) \tag{3.19}$$

For this case (a disk-integrated spectrum of a planetary atmosphere backscattered from the atmosphere's optical radius) we can therefore use equation 3.16 to rewrite EW (under the optically thin limit)

in terms of column density of the absorbing molecule and its absorption coefficient. Removing out of the integral the wavelength independent column density N, we retrieve the line strength of this molecular transition from eq. 3.11

$$\mathrm{EW} = 3N \int_0^\infty \sigma_\lambda d\lambda = 3NS_\ell \quad \text{for } \tau_\lambda << 1 \tag{3.20}$$

Based on this understanding of the basic principles of the theory of radiative transfer and on the nature of ro-vibrational molecular spectral lines, it is now possible to use - and even to build - more sophisticated models that replicate the spectra retrieved from the astrophysical observations, in order to be able to interpret the these observations properly.

3.1.3 The Search for minor atmospheric compounds using high-resolution spectroscopy - The case of C_3 in Titan

The search for the 4051Å absorption band of C_3 in Titan was conducted on the 2018 VLT/UVES Blue Arm observations as these cover the spectral region of interest. We shall call this calibrated and processed spectrum the "science-ready spectrum". Since all exposures were obtained in the same night, the novel method described in section 3.2 is not applicable in the 2018 data.

Dias et al., 2022 describe a simple and straightforward method of detection of minor chemical species using NASA's radiative transfer suite Planetary Spectrum Generator (PSG) (Villanueva et al., 2018). PSG is an online interface that simulates distinct planetary atmospheres spectra - allowing the user to vary gas, aerosol and cloud concentrations and composition as well as vertical structure of a planetary atmosphere, alongside a set of planetary, stellar, orbital parameters and even the characteristics of the observing instrument (Villanueva et al., 2018). Based on a large dataset of spectral information about distinct molecules, it allows a fast and user-friendly simulation of what the outgoing spectrum of a planetary atmosphere should look like as viewed at a given geometry from the chosen instrument (Villanueva et al., 2018). As Dias et al., 2022 describes, by simulating atmospheric spectra with variable abundances of the molecule of interest, it is possible to compare spectral features caused by this molecule in the conditions of the observed planetary atmosphere with observational spectra. This allows the detection of this chemical species on that planetary atmosphere, as well as estimating its abundance. In Negative detection cases, this method allows to estimate upper-limits for the studied species' abundance in the observed atmospheric layers.

This very useful tool, has, nonetheless its drawbacks, the main of which being its closed system nature, not allowing the input of any external spectral information of molecules missing on its large, but understandably incomplete catalogue (Villanueva et al., 2018). This proved to be a problem when searching for C_3 spectral signatures on the science-ready spectrum of Titan, as this exotic, transient molecule has not yet been detected in any planetary system atmosphere - and therefore, was excluded of the molecule spectral catalogue of PSG. Without this spectral information of our molecule of interest, it became impossible to use PSG to model the effect of C_3 on the spectrum of Titan. It soon became clear that this was just a consequence of a problematic issue with the molecular spectrum of C_3. The lack of high-resolution k-tables (containing high resolution spectral information required to model the absorption spectrum of a molecule) implied that it was impossible to automatically generate a synthetic Titan spectra with C_3. This is true for PSG and for other radiative transfer suites such as the less "blackbox" and more complex NEMESIS radiative suite (Irwin et al., 2008).

The transmittance spectrum of C_3 under the conditions of Titan shall therefore be obtained in an approximated way, based on the C_3 (000)-(000) 4051Å band oscillator strength and expected column

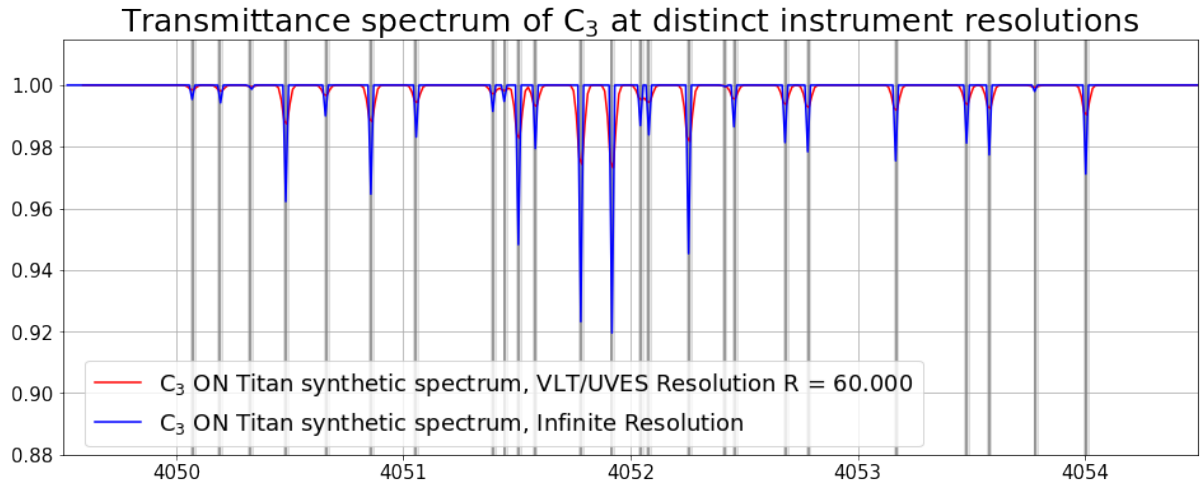

Figure 3.2: C_3 synthetic transmission spectra of its 4051Å $\tilde{A}^1\Pi_u$ - $\tilde{X}^1\Sigma_g^+$ 000-000 vibronic band at column density N = 5,0 $\times 10^{13}$ cm^{-2} for distinct spectral resolutions: Blue spectrum corresponds to an infinite spectral resolution whereas the Red spectrum corresponds to a transmission spectrum at the spectral resolution of VLT/UVES, of R = $\lambda/\Delta\lambda$ = 60.000. It is worth noticing that reducing spectral resolution implies a reduction in spectral line depth, as well as the merger of nearby spectral lines.

density retrieved from the literature. Previous photochemical modelling work on Titan's atmosphere have predicted a C_3 column density on Titan's upper atmosphere to be $N = 5{,}6 \times 10^{13}$ cm^{-2}, with a minimum expected column density extending down to $N = 5{,}0 \times 10^{12}$ cm^{-2} (Hérbad et al., 2013) (Dobrijevic et al., 2016). The valuable information regarding the spectroscopic proprieties of C_3 4051Å band was retrieved from the empirically obtained line list of high resolution observations of this band with VLT/UVES by Schmidt et al., 2014 (table 3.1). Schmidt et al., 2014 empirically retrieved the central wavelengths and oscillator strengths of the absorption lines on this C_3 band.

Resorting to this column density prediction by Hérbad et al., 2013 and Dobrijevic et al., 2016 and the Schmidt et al., 2014 spectral band data, first approximation synthetic C_3 transmittance spectra for Titan were obtained (figure 3.3). To do so, I followed the physical relations between spectroscopic quantities and the theory of radiative transfer: Individual C_3 oscillator strengths, f_J, on table 3.1, were firstly multiplied by the population distribution in rotational energy levels, J, as a function of temperature, which in a first approximation is provided through equation 3.12, where, for C_3, $B = 0{,}431$ cm^{-1}, from Tanabashi et al., 2005. From this product, it is possible to obtain each individual line's strength (S_i) at their central wavelength value (λ_0) within the (000)-(000) C_3 visible band from eq. 3.11, equivalent to the spectral integral of each individual transition's cross-section, $\sigma_i(\lambda)$. Using each line's intrinsic strength value, S_i, a profile for each line's cross-section, $\sigma_i(\lambda)$, is obtained assuming a Doppler broadened, or Gaussian profile (eq. 3.14).

Finally, it is possible to obtain the optical depth profile ($\tau_i(\lambda)$) as well as the spectral Transmission profile ($T_i(\lambda)$) for each spectral line through equations 3.7, 3.16 and 3.17. These individual spectral line profiles are then multiplied, allowing a spectral model of the C_3 band to be simulated as a function of one-way C_3 column density (N) as is shown in figure 3.3, for a disk-integrated, airmass = 3, atmosphere of Titan. All spectral lines are simulated with the same FWHM due to Doppler Broadening (eq. 3.14), which, for $\lambda_0 \sim 4050$ Å and T $\sim$ 150 K at altitudes of 1000 km in Titan's atmosphere - where C_3 abundances are predicted to be higher (Hérbad et al., 2013). This accounts for a Doppler broadened C_3 line FWHM of $\sim$ 0,006Å.

This step showcases the approximate way through which this synthetic spectrum is being obtained,

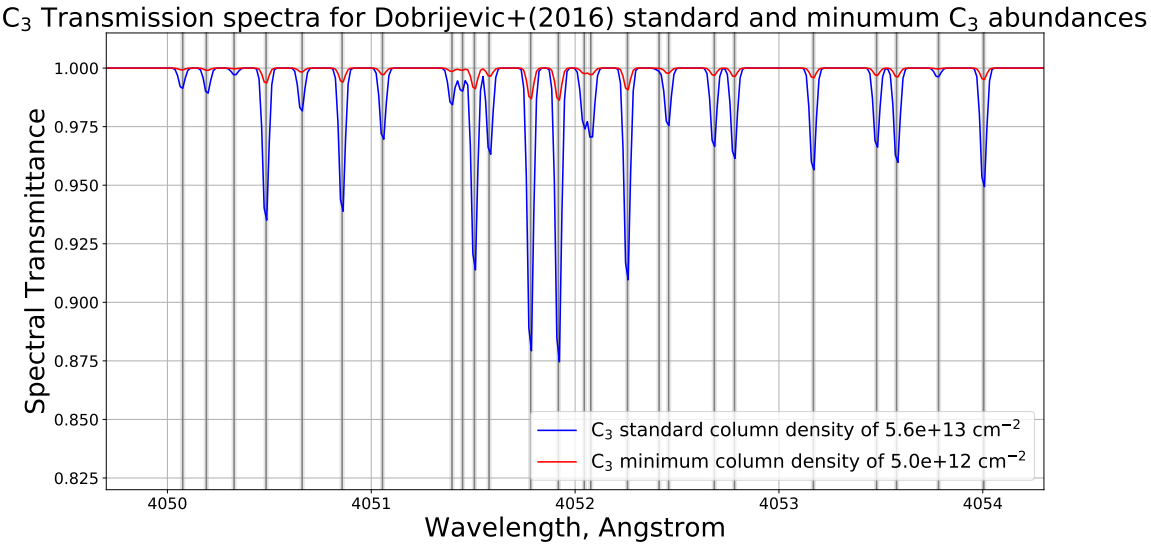

Figure 3.3: C_3 synthetic spectra of its 4051Å $\tilde{A}^1\Pi_u$ - $\tilde{X}^1\Sigma_g^+$ 000-000 vibronic band. The blue spectrum corresponds to a C_3 column density in Titan's upper atmosphere of 5,6 $\times$ 10^{13} cm^{-2} equal to the median value predicted by Dobrijevic et al., 2016 photochemical model. Red spectrum corresponds to the minimum value for C_3 column abundance expected by the same photochemical model, 5,0 $\times$ 10^{12} cm^{-2}. Vertical grey lines correspond to C_3 line centres and respective uncertainty of $\pm$0,01Å identified in Schmidt et al., 2014.

as a **one-layer approximation**. This means that Titan's upper atmosphere was modelled as a single, uniform, atmospheric layer that contains all the molecular absorber of interest (C_3) rather than a set of distinct layers each with its own C_3 abundance, Temperature and Pressure (Hanel et al., 2003) (Sánchez-Lavega, 2011) which would present a more realistic picture of Titan's mesosphere and thermosphere. This approximation was chosen to avoid creating by scratch a multi-layered radiative atmospheric transfer model, that due to its much more complex nature (requiring the application of the above mentioned methods for each atmosphere layer) would be far beyond the scope of this work (Irwin et al., 2008). Nonetheless, since Titan's mesospheric Temperatures are relatively stable as height increases, we have considered that treating Titan's C_3 atmospheric distribution as a single layer is a valid approach.

At this point comes into play the effect of the detector's resolution onto the observed spectrum. The above estimated FHWM of C_3 lines on Titan's spectra corresponds to spectral lines observed with an *infinite spectral resolution* - which, in practice, is not physical. Hence, we must take into consideration the the resolving power of the VLT/UVES detector, which at these observations was of $R = \lambda/\Delta\lambda \approx$ 60.000 (Dekker et al., 2000). This implies that with the spectrograph used in these observations, we expect a spectral resolution (in wavelength) no better than $\Delta\lambda = \lambda/R \approx 0,07$Å. Therefore, to account for this effect, we convoluted the synthetic spectra with a Gaussian filter with 0,07Å as its FWHM, in order to obtain a synthetic spectrum with the same spectral resolution as the VLT/UVES spectra of Titan. Examples of 2 synthetic spectra, one at infinite resolution and another at the VLT/UVES resolution are shown in figure 3.2. Examples of 2 synthetic transmittance spectra for C_3 at VLT/UVES spectral resolution are compared in figure 3.3 - one for the Dobrijevic et al., 2016 model standard one-way column density value ($N = 5,6 \times 10^{13}$ cm $^{-2}$) and another for its minimum predicted column density value ($N = 5,0 \times 10^{13}$ cm $^{-2}$).

To be able to interpret Titan's spectrum and assess the presence (or not) of C_3 in Titan, it is not sufficient to model only the C_3 transmittance spectrum. It is also key to model the actual outgoing spectrum of Titan to understand the impact that the possible absorption lines of C_3 would have on Titan's spec-

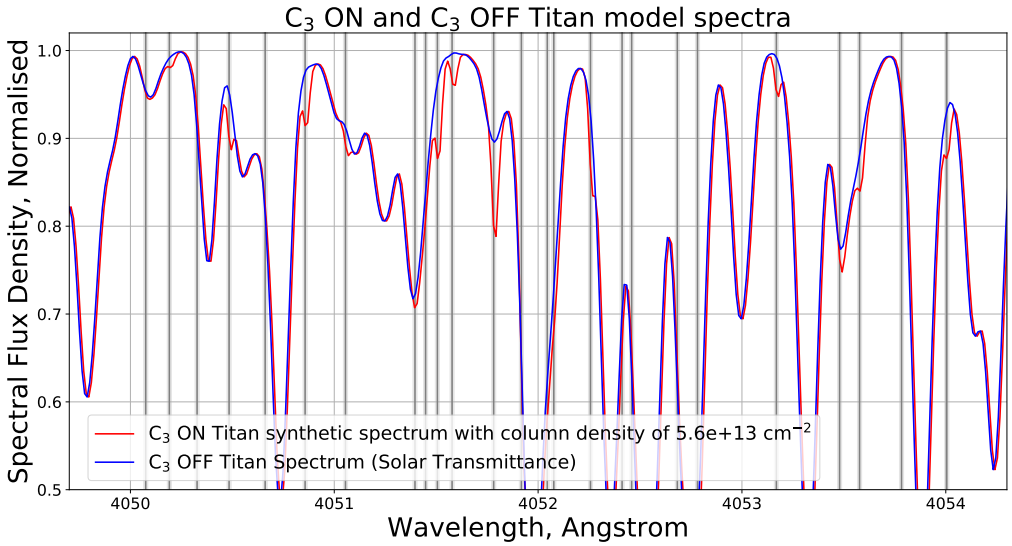

Figure 3.4: Synthetic spectra of Titan, with models with C_3 ON and C_3 OFF, covering the region of interest of the 4051Å $\tilde{A}^1\Pi_u$ - $\tilde{X}^1\Sigma_g^+$ 000-000 vibronic band. Blue spectrum corresponds to the C_3 OFF synthetic spectrum of Titan - full of deep solar absorption lines. Red spectrum corresponds to C_3 ON synthetic spectrum of Titan - obtained by multiplying the Doppler shifted solar spectrum with C_3 transmittance spectrum - at Dobrijevic et al., 2016 standard expected column density of C_3 on Titan's mesosphere of $5{,}6 \times 10^{13}$ cm^{-2}. Vertical grey lines correspond to C_3 line centres and respective uncertainty of $\pm$0,01Å identified in Schmidt et al., 2014.

trum. Following literature and analysis of Titan's simulated spectrum with PSG for these wavelengths, it is possible to consider that it is mostly devoid molecular absorption lines below 500 nm (McKay et al., 2001) with the spectrum consisting in a backscattered solar spectrum with Rayleigh scattering and haze absorption (Lorenz et al., 1999). Since both Rayleigh scattering and haze absorption evolve slowly with wavelength (Sánchez-Lavega, 2011), probing a small wavelength range of interest of about 10Å within the 405nm region of interest at very high resolutions, we shall expect Titan's spectrum to be of a flat backscattered solar continuum filled with solar absorption lines.

Hence, a high resolution solar spectrum that includes these solar absorption lines is required, in order to be able to model properly the visible, backscattered spectrum of Titan. We have used the very high resolution, BASS2000 normalised solar spectrum obtained by the large solar spectrometer of the International Scientific Station of the Jungfraujoch (Aboudarham et al., 2020), allowing a spectral resolution of 0,002Å. Nonetheless, in order to allow a direct comparison, this high resolution solar spectrum was, just like the transmittance model spectrum, also convoluted into the spectral resolution of the VLT/UVES instrument, $R \approx 60.000$.

Using the solar spectrum as a proxy of Titan's spectrum implies still a further correction in terms of Doppler shift: In order to be directly comparable with Titan's backscattered solar spectrum, the solar spectrum is Doppler shifted by a radial velocity equal to the radial velocity between Titan and the Sun at the moment of observation. To allow a direct comparison, we have also normalised the flux density values (and associated error bars) measured by the instrument's detector by the maximum flux value on the spectral region of interest (4045 to 4055Å) so that this observational spectrum can be directly compared with the modelled Titan spectrum. Hence all comparisons between model and observations (in particular, line depth measurements) will be relative - as model and observed spectra values will vary between 0 and 1.

Finally, in order to obtain a synthetic spectrum of Titan with expected C_3 absorption lines, the trans-

mittance spectrum of C_3 (that is a function of the C_3 one-way column density on Titan's atmosphere, N) is multiplied by the Doppler shifted solar spectrum. Therefore, we are left with 2 possible spectra of Titan: One of them is the Doppler shifted and convoluted to VLT/UVES resolution solar spectrum template (without any non-solar absorption line) which we will refer to from now on as **C_3 OFF Titan spectrum**. The other is the Doppler shifted solar spectrum multiplied by the transmittance spectrum of C_3 for a C_3 one-way column density of N - which we will refer to from now on as the **C_3 ON Titan spectrum**. These 2 possible spectra are compared on the plot of figure 3.4. Following Dias et al., 2022, when comparing these spectral models with observations, the model's sole free parameter N (the one-way column density of C_3 on Titan's mesosphere) can be adjusted while producing C_3 ON synthetic Titan spectra. By comparing model and observational spectra molecular line depths, an estimation of the abundance of C_3 on Titan's upper atmosphere can be retrieved.

From the comparison of C_3 ON and C_3 OFF model spectra of Titan it is evident that, for the standard predicted column density of C_3 on Titan's mesosphere by Dobrijevic et al., 2016, measurable differences exist between the 2 model spectra at the wavelengths of C_3 absorption lines. This is not true, however for all C_3 lines: The lines that coincide in wavelength to the much deeper solar absorption lines backscattered from Titan's atmosphere do not produce measurable differences in the spectrum of Titan, due to the coincidence in position with much deeper solar lines. From here it becomes clear that any detection of C_3 lines on Titan's atmosphere will necessarily have to occur on wavelengths in between the much deeper solar absorption lines. Furthermore, due to the distinct relative radial velocities between Titan and the Sun and inherently distinct Doppler shifts, in distinct observation nights, distinct spectral absorption lines will overlap deeper solar features. Taking all these aspects into consideration, we compare the synthetic spectral models with the observations on section 4.2.

3.2 The Doppler Method for spectral line identification

The wavelength range covered by the 2005 VLT-UVES Red arm observations of Titan (5200Å-6186Å) is known to cover a set of weak methane absorption bands, such as the 6190Å, 5970Å, 5760Å and 5430Å CH_4 bands (Giver et al., 1978). Although these absorption bands have been known for decades (Giver et al., 1978), and their presence identified in all of the solar system gas giant atmospheres (Karkoschka, 1994) (Sánchez-Lavega, 2011), these bands' high resolution, line-by-line nature is not yet known, unlike what happens with infrared CH_4 bands (Hargreaves et al., 2020). This molecule's line-by-line, high resolution spectrum has been characterised solely down to wavelengths above 746 nm (Hargreaves et al., 2020) and hence, the only currently available information regarding methane's visible bands is its low resolution band absorption coefficients (Smith et al., 1990).

Titan has the peculiarity of possessing the only planetary atmosphere in the solar system where CH_4 is the sole main molecular visible absorber on its atmosphere - unlike what happens in the giant planets' atmosphere, where H_2O, NH_3 or Collision-Induced Absorption by H_2-He are also important parts of the planetary spectrum (McKay et al., 2001) (Sánchez-Lavega, 2011). This lack of other major molecular visible absorber allows the detection and characterisation of the individual CH_4 lines that compose these visible absorption bands - as we can be sure that deep absorption lines to be found on Titan's high resolution spectrum methane bands are, indeed, CH_4 lines.

Although the sole major absorbing molecule in Titan's visible spectrum is CH_4, when observed in high resolution, its absorption lines appear amid significantly deeper solar absorption lines in Titan's visible spectrum (Luz et al., 2006). Thus, when aiming to characterise new CH_4 absorption lines on Titan, **it is imperative to distinguish between Titan's atmosphere absorption features and solar**

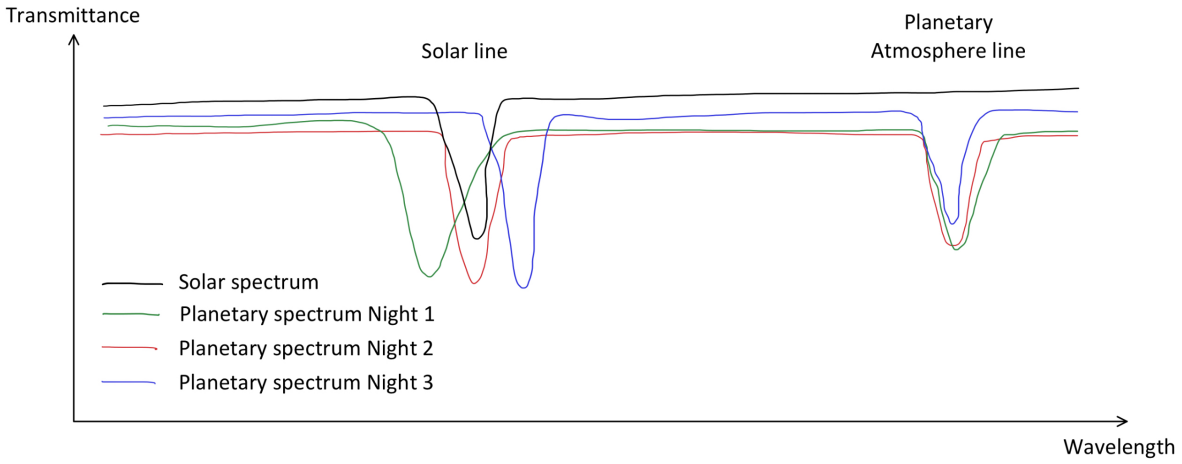

Figure 3.5: A schematic representation of the Doppler Method for line identification, allowing a clear distinction between lines of solar and planetary origin from an outgoing visible planetary spectrum. Different nightly spectra shall showcase a distinct Doppler shift when compared with the rest-frame solar spectrum and other nightly spectra, whereas planetary absorption lines conserve their rest-frame wavelength over observation nights, while also not coinciding with the position of solar lines.

absorption lines. This can be done by comparing Titan's spectrum with a detailed, high resolution solar spectrum, such as the BASS2000 solar spectral database (Aboudarham et al., 2020). However, given the large number of possible new CH_4 to be characterised in this unexplored region of Titan's spectrum, alternatives to a visual comparison between Titan and solar spectra were sought as a faster and more efficient way of distinguishing between solar and Titan spectral features.

The key motivation behind the Doppler line characterisation method described on this chapter is to accurately and efficiently distinguish between solar and planetary spectral high resolution lines in a backscattered high resolution spectrum of a planetary atmosphere. To do so, we have taken advantage of the 4 distinct nights of observation of Titan and their relative solar Doppler shift (which seemed to present a problem at first for not allowing to stack these observations and increase SNR) to distinguish between solar and Titan absorption lines.

The physical rationale behind this idea is grounded in the fact that Titan's atmospheric spectrum in visible wavelengths contains a mixture of spectral features originating in distinct frames of reference - corresponding precisely to the 2 origins, Sun and Titan, we intend to automatically distinguish. Many of the spectral absorption lines in Titan's high resolution outgoing spectrum correspond to solar absorption lines present in the backscattered solar radiation that constitutes the bulk of Titan's visible spectrum (Sánchez-Lavega, 2011). However some of these lines (in this case, the CH_4 high resolution lines that cause the low-resolution CH_4 visible absorption bands known for many decades) are originated on Titan's frame of reference.

The origin on the solar frame of reference of many observed absorption lines implies that, across different nights of observation, as the radial velocity between the Sun and Titan varies, so does the Doppler shift of solar absorption lines backscattered from Titan's atmosphere. As a result, **when comparing distinct nightly spectra, Solar lines will appear moved with respect to their rest-frame wavelength, due to their distinct Doppler shifts, whereas Titan lines will remain still on their rest-frame wavelength**. For reference, in our 4 nightly 2006 spectra of Titan by Luz et al., 2006, the maximum Doppler shift between 2 observation nights is of 94 mÅ (see table 2.1). This separation is larger than the expected line width at the instrument's resolution of $R \approx 100.000 \rightarrow \Delta\lambda = \lambda/R \approx 60$mÅ. A schematic representation of this effect is shown in figure 3.5.

We propose to use this fact to detect absorption lines originated on Titan's atmosphere in a visible spectrum crowded with solar lines. To do so, it is only necessary to possess several spectra of the atmosphere of interest observed at times when the planet's radial velocity with respect to the sun is different. For this, we retrieved the continuum component of the observational spectra, by applying a median filter to each spectral point, assigning it the median value of it and its 300 nearest neighbours. Next, we have normalised sections of interest of Titan's spectra by dividing the night and disk-integrated spectra by this continuum, preparing for our Doppler Line Identification method to be applied. Assuming a single reflecting layer model of Titan's atmosphere (Lorenz et al., 1999), this normalised by the continuum spectrum provides Titan's atmosphere high resolution transmittance spectrum, $T(\lambda)$, down to an optically thick reflecting layer.

Applying this Doppler method for line detection, the first step was obtaining a list of all absorption lines in each normalised nightly spectrum, by finding the inversion points (of derivative 0) in each spectra. Then, all points on all these 4 spectral line lists were compared, automatically **selecting only spectral lines whose line centres on all 4 observation nights are not separated by more than 1/4 of the maximum solar Doppler shift between daily spectra (approximately 25mÅ)**. All detected lines whose dispersion across nightly spectra was larger than 25mÅ were discarded as solar lines. The remaining lines are to be considered "detected" lines originated on Titan's rest frame.

Each of the "detected" (non-Doppler shifted) line's position was calculated from the mean of the 4 respective line positions in the 4 observation nights - with this measurement's uncertainty being the standard deviation of the 4 line position measurements. For each detected line, its relative depth with respect to its immediate neighbourhood continuum and its full width at half maximum (FWHM) was also estimated. In addition, we have considered only detected lines with a relative depth of at least 2% of the continuum, as we shall discuss further ahead.

This final, retrieved linelist, of all spectral lines whose central position has not shifted by more than 25mÅ over the course of different nights of observation, shall correspond to absorption features originating from the rest frame of Titan - which at these visible wavelengths (5200Å to 6186Å) are expected to be new, previously undetected CH_4 absorption lines. A list of corresponding line depth (with respect to the continuum) for selected lines has also been obtained from the mean of line depth from the distinct nights of observation. On the next 2 sections, it is described how the characterisation of these newly detected lines can take an extra step, towards retrieving specific line strengths of these new visible CH_4 lines.

3.2.1 Estimating CH_4 column density on Titan

A key step towards characterising the intrinsic strength of the newly detected CH_4 lines is to estimate the column density of CH_4 molecules interacting with the radiation field, shaping Titan's outgoing planetary spectrum. To do so, we shall once again have to consider a simplified model of Titan's atmosphere, since these previously unknown high resolution CH_4 lines are not included in any available k-tables to be implemented on radiative transfer suites such as PSG or NEMESIS.

We shall therefore consider a simplified model of radiative transfer on Titan's atmosphere, once again, based on the 1-layer reflecting model described on the previous section. In a brief way, in such a simplified model, it is assumed that the solar radiation field penetrates on Titan's atmosphere down to its optical radius (the atmospheric layer at which Titan's atmosphere becomes optically thick (Lorenz et al., 1999)), before being backscattered back into space. Hence, the one-way column density, N, of CH_4 that is imprinting the absorption lines on Titan's visible spectrum corresponds to the column density of this

gas from the top of the atmosphere down to the optically thick radius of Titan.

Measurements of the optical radius of Titan showcase significant temporal variability (from Lorenz et al., 1999) ranging from 150km to 300km at 6000Å, with the majority of the measurements clustering around an optical radius of 200km, which is the value we have considered for this study. Hence, based on Teanby et al., 2006 vertical profiles of chemical species on Titan's atmosphere (figure 3.6) the one-way column density of CH_4 was obtained by summing all the way down to the optical radius altitude (z = 200km) the discrete values of column density for each altitude bin, $n(z)$. This sum (or discrete integration) of CH_4 molecular abundance in altitude was corrected for the spherical geometry of the atmosphere (function of Titan's radius, R_{Titan}), following the example of Lellouch et al., 2022, as expressed on equation 3.21.

$$N = \int_z^{\infty} n(z') \left(1 + \frac{z'}{R_{Titan}}\right)^2 dz' \tag{3.21}$$

From this column density integration down to Titan's optically thick radius, we have estimated a 1-way column density of CH_4 molecules of $N_{CH_4} = 4{,}4 \times 10^{21}$ molecules.cm^{-2}.

3.2.2 Measuring line strength of newly identified lines

At this point, the original method of new line detection on visible planetary spectrum has been described. I intended however, to take this new line characterisation effort one step further, and retrieve physical quantities that describe the spectroscopic nature of the absorption lines within these bands, by estimating these lines' characteristic line strength, S_i. The 2 methods through which I estimated the line strength of the newly discovered spectral lines in Titan's spectrum are described as follows.

S_i **measurement based on line-retrieved EW**: Measuring the average FWHM for each of Titan's spectral lines, and a assuming a Gaussian line profile, for optically thin lines, it is possible to estimate each detected Titan line's Equivalent Width (EW) from each line's relative depth and FWHM as follows: Equation 3.20 relates EW and line strength S_i. At the same time, relative line depth (LD) is given, following the optically thin approximation, by combining equations 3.17, 3.14 and 3.14, at the line centre, when $\lambda = \lambda_0$, such that relation of eq. 3.22 arises. From here, and knowing that EW = $3NS_i$ from equation 3.20, we reach eq.3.23 that allows to estimate the equivalent width of an optically thin spectral absorption line.

$$LD = 1 - T(\lambda_0) \approx 3N\sigma_i(\lambda_0) = 3S_iN\frac{2\sqrt{\ln(2)}}{\text{FWHM}\sqrt{\pi}} \tag{3.22}$$

$$\text{EW} = \text{LD} \cdot \frac{\sqrt{\pi}}{2\sqrt{\ln(2)}} \cdot \text{FWHM} \tag{3.23}$$

Again, assuming optically thin spectral lines, EW is related to the line's intrinsic strength S_i, as well as to the 1-way column density of the absorbing gas molecules down to the optically thick reflecting layer, N, by EW $= 3NS_i$. From here, we are at last able to estimate the detected novel CH_4 visible absorption line's intrinsic strength, S_i, in cm^{-1}/(molecule.cm^{-2}) units, by equation 3.24. We shall call this intrinsic line strength estimation method the "**Equivalent Width Method**".

$$S_i = \frac{EW}{3N} = \frac{\text{LD} \cdot \text{FWHM}}{3N} \cdot \frac{\sqrt{\pi}}{2\sqrt{\ln(2)}} \tag{3.24}$$

S_i **measurement based on Modelled Line Profiles:** An alternative method also used in this study

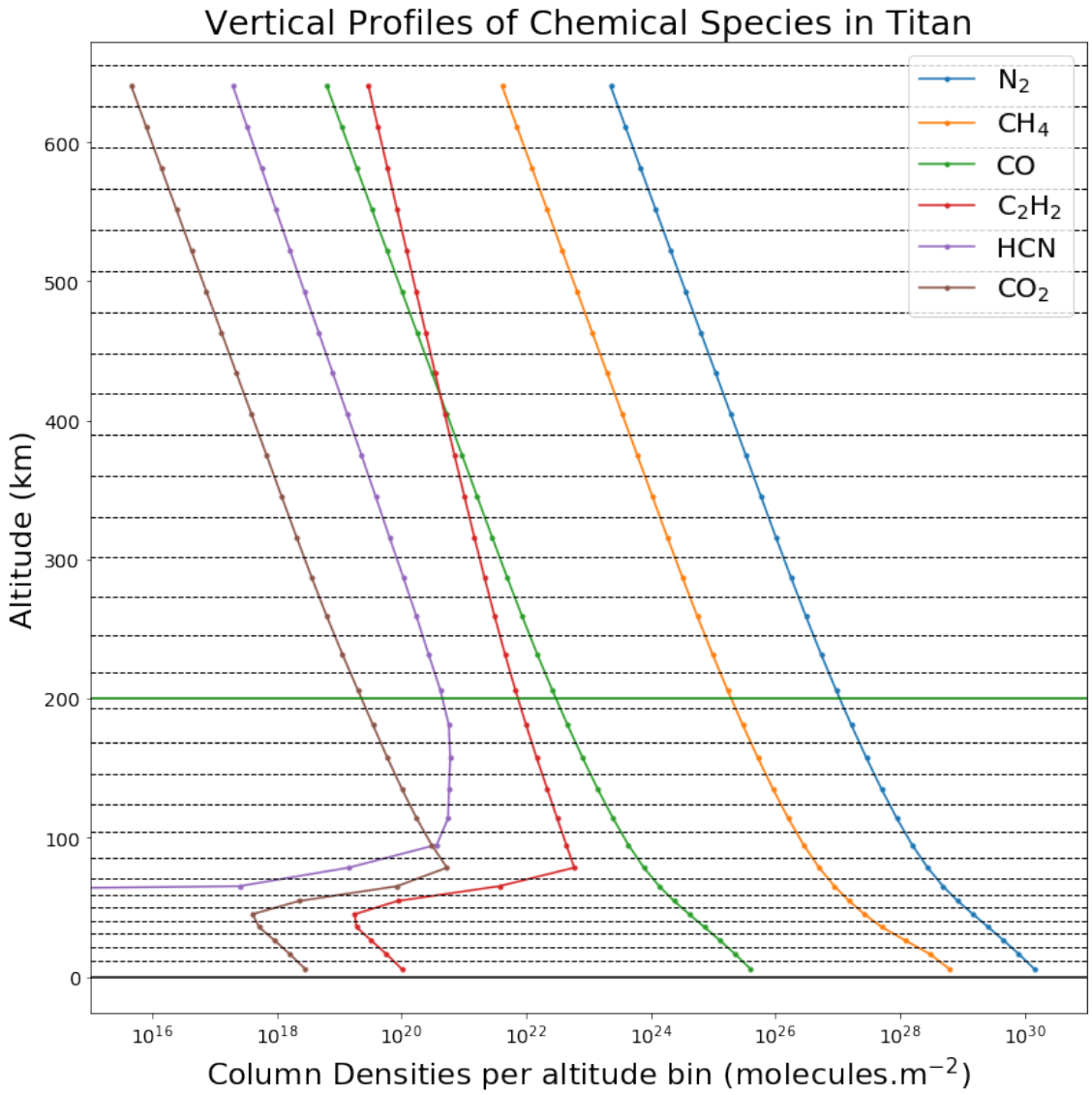

Figure 3.6: Plot of Vertical Profiles of main atmospheric chemical compounds in Titan's atmosphere, produced during the context with data from Teanby et al., 2006. Abundance values are provided in column densities per altitude bin, which are delimited by black dashed horizontal lines. Horizontal green line corresponds to Titan's optical radius at 6000Å (from Lorenz et al., 1999) down to which CH_4 column density profile (orange) was integrated.

to estimate the intrinsic line strength of each detected line, S_i, in cm^{-1}. (molecule. $cm^{-2})^{-1}$ units, was the comparison of the observed spectra to a set of synthetic spectra of Titan, whereupon these newly detected lines are simulated with different intrinsic line strengths. To do so, we have considered that CH_4 lines are approximated by a Gaussian profile, whose cross-section as a function of wavelength, given by equation 3.14, is then multiplied by the retrieved column density N_{CH_4} and retrieved as a transmission profile following equations 3.16 and 3.17. A set of 18 distinct models with line strength, S_i, values varying from 5.0×10^{-26} cm/molecule to 9.0×10^{-25} cm/molecule were simulated and compared with the observations.

As a first approximation, all spectral lines are simulated with the same Full Width at Half Maximum (FWHM) due to Doppler Broadening (eq. 3.14) for a temperature equal to that of the altitude with the highest CH_4 abundance above Titan's optical radius (of 180K at 200km of altitude). This implies a Full Width at Half Maximum of CH_4 absorption lines of 15mÅ.

This set of synthetic transmittance spectra of CH_4 lines are convoluted by a Gaussian profile (corresponding to a detector resolution of $R \approx 100.000$ or $\Delta\lambda = \lambda/R = 0.06$Å) to match the detector's resolution. Then, they are multiplied by an average spectrum of the VLT-UVES Red arm observations where the new CH_4 spectral lines identified by this Doppler Method have been removed (in a neighbourhood of 0.1Å of the line centre, replaced by a 1st order polynomial that connects with the rest of the unaltered spectrum). This allows to compare the line bottom of these newly detected lines in VLT-UVES spectra of Titan to the line bottom in several synthetic spectra of varying intrinsic line strength - providing an estimate of the detected CH_4 lines' strength based on the best match between VLT-UVES lines' and synthetic lines' bottom, as can be observed in figure 4.4 of the results section. We shall call this intrinsic line strength estimation method the "**Model Fit (MF) Method**".

The final list of the detected Titan CH_4 absorption lines and respective line depth, EW and Intrinsic Strength (measured by both methods), as well as a set of plots showcasing the detection of these new lines estimation will be presented in the results section 4.1, and assessed at the discussion section 5.1. That assessment of the results and methods that includes as well the comparison between the 2 distinct S_i retrieval methods.

3.3 Atomistic Molecular Dynamics Simulations

3.3.1 GROMACS, the simulation suite: The Computational Approach to Chemistry

With the goal of understanding the nature of the interactions between organic molecules under Titan's conditions, a computational approach to chemistry was taken during the course of this work, to model the intermolecular interactions between amino acids in Titan-like conditions. The goal here was to run molecular dynamics simulations that replicate for very short timescales ($< 1\mu$s) the interactions of several hundred molecules - so that statistical proprieties of the molecular distribution and interactions could be retrieved, and possibly hint at an explanation for the ongoing laboratory results.

Distinct types of Molecular Dynamics simulations can probe very different orders of magnitude of length and timescales - for which distinct simulation methods are more suitable to (Allen et al., 1991). For the context of the timescales we are interested in probing, intermolecular interactions (from ps up to a few ns) and up to a few hundred molecules, the most suitable type of simulations are **Atomistic Molecular Dynamics Simulations** (Allen et al., 1991)(Abrahams et al., 2015b). The software used to run such type of simulations is GROMACS which is an open-source and free software that enables high-performance simulations of chemical systems. It provides a very useful way to test inter-molecular interactions, be

it, for instance, as a way to predict the behaviour and physical characteristics like solubility, diffusion coefficients or viscosity of fluid mixtures or as a way to model the dynamics of bio-molecules (Célia-Silva et al., 2020) (Morgado et al., 2020).

Atomistic Molecular Dynamics Simulations run by GROMACS are simulations where each atom in a molecule is modelled as an individual force field (Abrahams et al., 2015a). This force-field takes its form from a simple dispersion potential (Lennard-Jones potential between 2 interactive centres, i and j, eq. 3.25) for electronically neutral atoms. It is also combined with an electrostatic potential of partial charge q (eq. 3.26) for the atomic permanent dipoles of a polar molecule (Abrahams et al., 2015a). These electric dipoles cause many of the most intense inter-molecular interactions such as hydrogen bonds.

$$V_{LJ}(r_{ij}) = 4\varepsilon_{ij}\left[\left(\frac{\sigma_{ij}}{r_{ij}}\right)^{12} - \left(\frac{\sigma_{ij}}{r_{ij}}\right)^{6}\right], \quad \text{with} \quad \sigma_{ij} = \sqrt{\sigma_i\sigma_j}\ ,\ \varepsilon_{ij} = \sqrt{\varepsilon_i\varepsilon_j} \tag{3.25}$$

$$V_e(r_{ij}) = k_e\frac{q_iq_j}{r_{ij}} \tag{3.26}$$

In order to create a model of a type of molecule within this software, as a preparation for the simulations to be run, atomic parameters such as the interactive centre size (σ), its dispersion energy (ε) and partial charge (q_i) must be provided for each distinct atom within a molecule. Alongside these atomic potentials, the stretching of each molecular bond between 2 atoms of the same molecule is modelled by a classical harmonic potential (eq. 3.27), with a bond equilibrium length (b_{ij}) and spring constant (k^b_{ij}) that must also be defined for each bond (Abrahams et al., 2015a).

$$V_b(r_{ij}) = \frac{1}{2}k^b_{ij}(r_{ij} - b_{ij})^2 \tag{3.27}$$

Similarly, for any group of 3 consecutive atoms (i, j, k) in a molecule, an harmonic angle potential must be defined to account for angle vibrations around an equilibrium angle θ^0_{ijk},3.28 while for any group of 4 consecutive atoms a dihedral oscillation can also be modelled by a harmonic potential (Abrahams et al., 2015a).

$$V_\theta(\theta_{ijk}) = \frac{1}{2}k^\theta_{ijk}(\theta_{ijk} - \theta^0_{ijk})^2 \tag{3.28}$$

For larger molecules and to make simulations less computing demanding, some simplifications can be included, such as applying cutoffs to potentials, so that interactions between more distant atoms are neglected. Periodic boundary conditions at the simulation boxes are also used to avoid any interactions with a wall (Abrahams et al., 2015a).

Hence, to run a simulation, all the previously mentioned parameters must be accounted for to model individual molecules. In the case of the molecules simulated in this work (Glycine, Alanine and α-Aminobutyric acid) an atomistic model for each molecule was obtained using the LigParGen web interface. It retrieves a molecular model in the format required by GROMACS, as an Optimized Potential for Liquid Simulations - All Atoms (or OPLS-AA) with all the atomistic parameters required to simulate an interactive force field of the molecules in study (Dodda et al., 2017).

Then, a simulation box is created and the intended number of molecules is distributed randomly in its interior. However, before the simulation "proper" is run, a set of energy minimisation steps are run, to make sure the molecules start the "proper" simulation with "reasonable" energies. This is done to attenuate non-physical mechanical energies in the system caused by the random distribution of molecules - some of which may have begun unrealistically too close to one another. In order to reduce the com-

putational power required to run the simulations, a Verlet-type cut-off radius is used for short-range interactions such as the Lehnard-Jones dispersion potential. A Verlet cut-off radius of 1.4 times the effective particle size (σ_i) is considered, so that short-range interactions are only considered between particles within this dispersion "sphere of influence" (Abrahams et al., 2015b).

Only after this energy minimisation step can the "proper" simulation be run at the chosen thermodynamic ensemble - NPT for constant pressure and NVT for constant volume (with constant particle number and temperature) (Abrahams et al., 2015a). The set of physical conditions in which the simulations will be run, alongside the intended time of simulation, is also provided to the simulation program. This allows, for instance, a set of thermodynamic processes to take place onto the simulation box such as Temperature or Pressure variation following a provided functional form over the course of the simulation. These processes are regulated over the course of the simulations through inbuilt thermostats and barostats such as the Berendsen and the Bussi-Donadio-Parrinello thermostats and the Parrinello-Rahman barostat used over the course of these simulations (Abrahams et al., 2015b). The necessity of and specificities of the use of these distinct Temperature and Pressure regulators will be discussed alongside the description of the kinds of simulations used to model the nature of amino acid interactions, on Section 3.3.2.

3.3.2 Amino-acid interaction simulations

In order to probe the nature of intermolecular interactions between amino acids under Titan's conditions, 2 distinct types of simulations were designed to probe different aspects of their interaction. On the first set of simulations, described at Subsection 3.3.2.1, the goal was study the structure of an amino acid thin film, both in the case of pure amino acid samples, and in the case of equimolar mixtures of two amino acids. For the second set of simulations, described at Subsection 3.3.2.2, the goal was to quantify the intermolecular interactions - in particular the amount of Hydrogen bonds - established between amino acids in a pure samples or within equimolar mixtures, away from film interfaces, in what we refer to as "film bulk".

3.3.2.1 Thin film amino acid simulations

Amino acid thin film simulations were run with the goal of modelling the interface of a thin amino acid film with a vacuum, so that the interface organised structure of an amino acid film under such conditions could be retrieved, since these could impact the interaction of incident radiation perpendicularly to the thin film's surface. 6 distinct simulations were run: one for each individual pure amino acid sample, and one for each pair of equimolar amino acid mixtures.

To model these thin films, 400 amino acid molecules were input into a cubic simulation with periodic boundary conditions of 4 nm sides (values chosen so that the simulation box would contain amino acids at their solid phase density) and an energy minimisation pre-run was conducted under NVT conditions, with a Berendsen thermostat. This thermostat is a very efficient method of relaxing a system's mechanical energy, as, by factoring particle velocities by a factor λ (given by eq. 3.29), at each timestep Δt, the system's Temperature difference to the expected temperature ($T - T_0$) exponentially decreases within a timescale close to τ (Berendsen et al., 1984). The temperature chosen for the energy minimisation was the temperature at which the density of the amino acids was calculated: 25ºC or 298,15K.

$$\lambda = \left[1 + \frac{\Delta t}{\tau}\left(\frac{T_0}{T(t - \frac{1}{2}\Delta t)}\right)\right]^{1/2} \tag{3.29}$$

Following energy minimisation, the box size was expanded in one of the directions - from 4nm to 10 nm, leaving a simulation box of 4nm x 4nm x 10 nm dimensions. This is such that the energy minimised clustered molecules maintain a cubic shape with 4 sides still subject to periodic boundary conditions, but with other 2 sides exposed to the vacuum in the direction of the simulation box extension, as can be seen on the simulation snapshot captures showcased in figure 3.7.

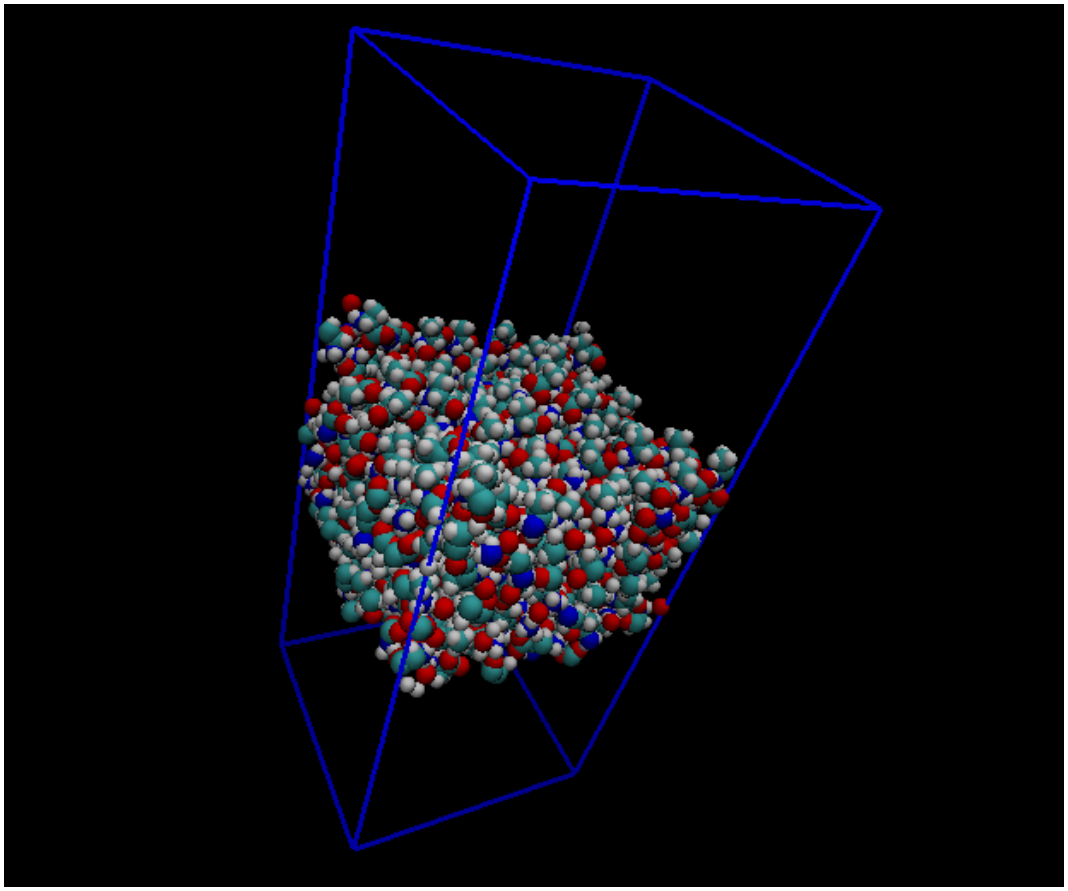

Figure 3.7: Snapshot of a thin film simulation of a pure sample of 400 alanine molecules at a 4nm x 4nm x 10nm periodic boundary box, at a temperature of 600K, run with GROMACS and visualised with VMD software. White atoms correspond to hydrogen, red to Oxygen, green to Carbon and blue to Nitrogen. It is worth noticing that 2 of the interfaces of this thin alanine film are facing not other alanine molecules (as is the case in periodic boundary conditions) but a vacuum, towards the direction of the longest side of the simulation box.

At this point, it was possible to run the simulations proper. While it was attempted to model this system at Titan's surface temperature of about 90K, this idea was abandoned due to its inability to provide statistically meaningful results regarding the structural distribution of amino acids within a film. This is since at 100K, the thermal movements of particles within the simulated film are very reduced. This causes the explored phase space of positions and velocities within the 400 molecules system to be very reduced, even for considerably long simulation times at this scale, of up to 10nm. The lack of mobility of particles within the simulation box causes the amino acid density plot of to be very noisy and full of spikes - corresponding to the initial positions where molecules started the simulation at, and from where they barely moved.

One possible solution to this effect was to run several identical simulations with distinct initial positions of the molecules, as a way to explore the phase space. However, this would imply a significantly more computer time demanding - and hence, less time efficient - set of simulations, since for all new initial configuration simulations a new set of energy minimisation steps would have to be taken. There-

fore, the solution that was chosen to this problem involved, instead, to provide more mobility to the simulated amino acid molecules. For this, the simulations were run at 600K, a temperature above all the amino acids in study melting point. In a molecular dynamics simulation of a liquid sample, it is possible to probe very efficiently a wide region of parameter space given the larger mobility of the constituent molecules of the liquid (Abrahams et al., 2015b).

It could be argued, nonetheless, that simulating the amino acids at temperatures 500K above the simulated on the laboratory experiments would not replicate the physical conditions and mechanisms through which these molecules interact. However, given that the experimental work being conducted by the Astrobiology group at Instituto Superior Técnico (IST) included deposited amino acids into a thin film through vacuum sublimation, they should present a mostly amorphous solid form, as similar amino acid deposition experiments reported a lack of long-range crystal structure (Maté et al., 2011) (Rodrígez-Lazcan et al., 2012). Hence, such an increase in temperature into their liquid state should not, in theory, alter the nature of the amorphous structure of the amino acid films. Hence, modelling the functional groups distribution along a simulated thin liquid amino acid film through their density profile along the film can be considered a valid 1st order approach to unveiling the structural nature of the thin amino acid films studied in laboratory.

Our goal was therefore to retrieve atomic/functional group density distribution profiles within the amino acid films, in order to qualitatively assess whether some sort of structure arises within the film from the interactions between the molecules. For this, the 6 distinct sets of amino acid film simulations were run for 10 ns of simulation time (after 5 ns of constant temperature increment and 1 ns of equilibration time) under NVT conditions regulated by a Bussi-Donadio-Parrinello thermostat (Bussi et al., 1984). This thermostat is very similar to Bersendsen's thermostat, but unlike this latter one, a stochastic term has been added, so that, just like what happens in a physical system, the total kinetic energy of the particle system (K) is subject to stochastic variability around an average value (K_0). This thermostat follows equation 3.30, where N_f is the number of degrees of freedom and dW is a Wiener process (Bussi et al., 1984) (Abrahams et al., 2015a).

$$dK = (K - K_0)\frac{dt}{\tau} + 2\sqrt{\frac{KK_0}{N_f}} \cdot \frac{dW}{\sqrt{\tau}} \tag{3.30}$$

The film density profiles resulting from these simulations - calculated by the GROMACS "-density" function (Abrahams et al., 2015a) are presented at the section 4.3. This function provides a very efficient way of averaging out all atoms positions along all simulation timesteps, and dividing the direction perpendicular to the film (measuring 10nm) into 1000 bins (each corresponding to a 0.01nm slice of the simulation box along its longest side). It is so that a density profile of all atom types and functional groups along the film can be drawn from this time average over box slices of atom's positions (Abrahams et al., 2015a).

3.3.2.2 Film bulk amino acid simulations

The second type of molecular dynamics simulations aim at retrieving the nature of intermolecular interactions within the liquid film bulk, following the example of Célia-Silva et al., 2020, Morgado et al., 2020 and L. Martins et al., 2021. On these studies, intermolecular interactions between solutes and solvents are tracked by retrieving the Radial Distribution Function (RDF) of a solute with respect to distinct functional groups within a solvent. In our case, and similarly to the thin film scenario, simulations were also started with an energy minimisation process at a 4 nm x 4 nm x 4 nm periodic boundary

conditions box coupled to a Berendsen thermostat. However, in this case, after energy minimisation, the box was not expanded, so that the box remains cubical with all sides subject to periodic boundary conditions without an interface with vacuum. Thus, we expect to be able to simulate the bulk of the thin amino acid film, so that effects of its interface organisation are no longer important and the simulated sample corresponds to a well mixed liquid.

In this film bulk we intended to measure the radial distribution function of given atoms with respect to others in distinct molecules, to account for intermolecular interactions (Célia-Silva et al., 2020). Of particular interest within these zwitterionic amino acids with a very polar character were the Hydrogen bonds. These intermolecular bonds are expected to occur between the partial positive charges of the 3 Hydrogen atoms within the amine group and the negative partial charges of the Oxygen atoms at the carboxyl group. Hence, the goal of these film bulk simulations shall be to obtain radial distribution functions of hydrogen atoms of other amino acids molecules around all Oxygen atoms within the 400 molecules of the simulation (Morgado et al., 2020).

For this, a constant increase of temperature from 298,15 K to 600 K (over 5 ns) and a subsequent equilibration period (1 ns) were simulated before 10 ns of simulation proper, in which calculations of radial distribution function (RDF) shall be performed (Morgado et al., 2020). The main difference between these simulations and the prior thin film simulations is the cubic nature of the box and its NPT conditions. Unlike the previous case, here it is important to preserve the pressure of the system, rather than its volume, since the molecules are immersed in bulk of the liquid, in which box size is no longer relevant, as we are no longer interested in modelling interfaces. Keeping the liquid bulk's pressure is important so that no interface with a vacuum appears. To do so, a Parrinello-Rahman barostat was used, maintaining the pressure of the system constant by adapting the size of the simulation box over the course of the simulation (Parrinello et al., 1981).

Obtaining the desired RDF profiles of hydrogen atoms in spheres around the Oxygen atoms in the simulated molecules requires counting the number of hydrogen neighbours to an Oxygen atom within spherical shells of inner radius r and outer radius $r+dr$, which will be denoted by $N(r, r+dr)$. The Radial Distribution Function (RDF(r)) is then obtained by calculating the density of hydrogen neighbours $N(r, r+dr)$ within the volume of the spherical shell between r and $r+dr$, and dividing this density by the averaged number density of hydrogen atoms within the simulation box n_H, following eq. 3.31:

$$\mathrm{RDF}(r+dr) = \frac{N(r, r+dr)}{V_{shell}(r, r+dr) \cdot n_H} \tag{3.31}$$

The calculus of RDFs is automatically conducted by the GROMACS function "-rdf", over radius bins of 0,002 nm (Abrahams et al., 2015b). From the calculated curves of H atoms radial distribution functions surrounding a O atom, it was possible to quantify the average number of H neighbours within the first RDF peak by inverting equation 3.31 and integrating $N(r, r+dr)$ up to the first local minimum (Morgado et al., 2020). This is since for each amine Hydrogen in the neighbourhood of an Oxygen atom, 2 other Hydrogen atoms present in the same amine group will necessarily occur slightly further away from the O atom than the first one - not due to the establishment of an hydrogen bond, but rather due to the molecule's geometry - imprinting a shallower secondary peak on the calculated RDF.

These GROMACS density and radial distribution functions do not provide, nonetheless, uncertainties or errorbars from their measurements, causing it to be impossible to have a precise uncertainty or errorbar for the retrieved measurements. On section 5.3 we provide, however, an estimation for the typical uncertainty of these average number of neighbours measurements, alongside the comparison between the RDFs from a pure amino acid sample and an amino acid mixture.

Table 3.1: C_3 $\tilde{A}^1\Pi_u$ - $\tilde{X}^1\Sigma_g^+$ 000-000 vibronic band line list (at 4051Å) as obtained in laboratory by Schmidt et al., 2014. Line position uncertainty is smaller than 0,01Å and line names are associated to the P,Q and R branches of this molecular band. Oscillator Strengths for each transition (f_J) are also shown. Perturbed lines are marked with an asterisk. Based on this linelist from Schmidt et al., 2014, we obtained the synthetic first approximation spectra of this C_3 visible band of Figure 3.3.

Wavelength (Å)	Line	Oscillator Strength, f_J ($\times 10^3$)
4050.075	R(14)	3.49
4050.191	R(12)	3.58
4050.327	R(10)	3.73
4050.401*	R(6)	0.58
4050.484	R(8)	3.95
4050.567*	R(4)	0.49
4050.661	R(6)	4.21
4050.746*	R(2)	0.45
4050.857	R(4)	4.44
4051.055	R(2)	3.78
4051.190*	R(2)	2.08
4051.255	R(0)	4.22
4051.396*	R(0)	10.58
4051.448	Q(2)	6.87
4051.506	Q(4)	7.70
4051.578	Q(6)	7.89
4051.782	Q(10)	7.96
4051.820	P(2)	1.06
4051.918	Q(12)	7.97
4052.045	P(4)	1.57
4052.077	Q(14)	7.98
4052.122*	P(6)	0.28
4052.180*	P(4)	0.86
4052.257	Q(16)	7.98
4052.412	P(6)	2.56
4052.459	Q(18)	7.99
4052.521*	P(8)	0.39
4052.683	Q(20)	7.99
4052.782	P(8)	2.82
4053.169	P(10)	2.87
4053.479	Q(26)	7.99
4053.577	P(12)	2.87
4053.783	Q(28)	8.00
4054.005	P(14)	2.86

Chapter 4

Results

4.1 High-resolution line detection on visible CH_4 bands on Titan's atmosphere

The previously described Doppler Method for Spectral line identification was applied to observations of Titan in 4 spectral regions that are known to contain weak CH_4 absorption bands whose individual lines were yet to be characterised in high resolution (Karkoschka, 1994). In figure 4.1, is showcased the entirety of the observed spectrum of Titan by the Red Arm of VLT/UVES on the night of 08/01/2005 by Luz et al., 2006, from 5250Å to 6186Å. This spectrum showcases many deep solar absorption lines and 4 visible absorption bands of CH_4, spectral regions with reduced spectral continuum, due to overlap of many weak CH_4 absorption lines.

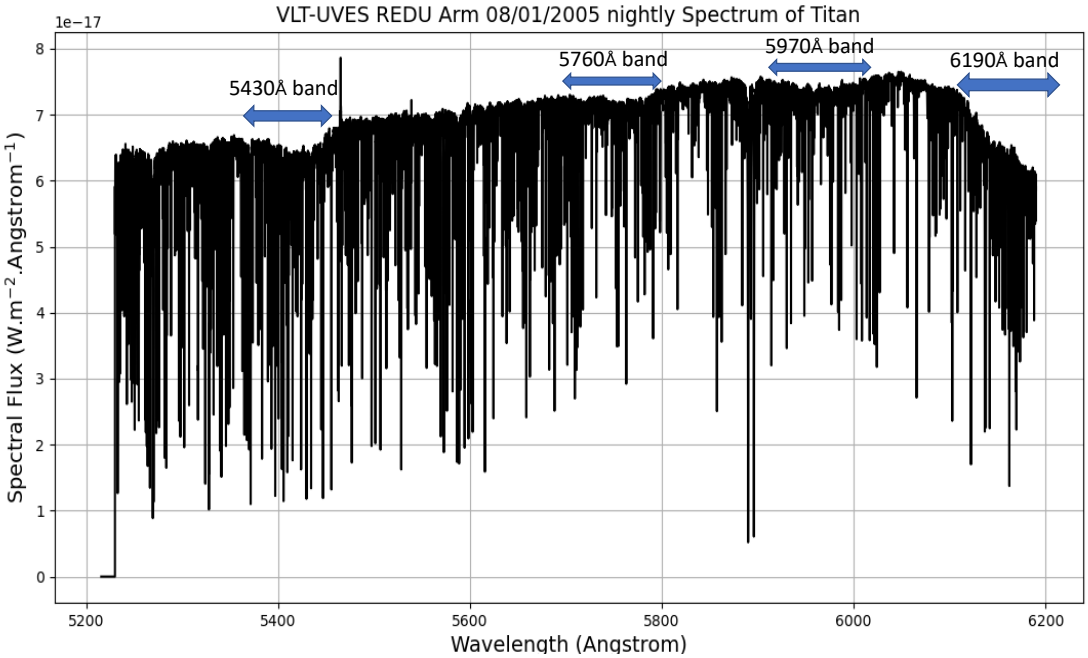

Figure 4.1: VLT-UVES REDU disk-integrated, night-averaged spectrum of Titan from Luz et al., 2006, from the 08/01/2005 observation night. This spectrum covers the wavelength range from 5250Å to 6186Å, with 4 CH_4 absorption visible bands (5430Å, 5760Å, 5970Å, 6190Å). The 6190Å is the most intense visible absorption CH_4 band in this wavelength range as described in Giver et al., 1978 and Karkoschka and Tomasko, 2010.

Our 2 key detection threshold parameters were: Maximum line centre distance of 25mÅ between

all distinct observation nights (all line positions in different observation nights shall fall within a span of 25mÅ) and a minimum relative line depth value of 2%. The detection threshold distance between line positions on different nights was chosen to be about 1/4 of the expected maximum solar Doppler shift between the most redshifted and the most blueshifted observation nights (between 13/1/2005 and 16/1/2005, with a maximum separation of 94mÅ). For spectral lines with separations larger than these between distinct nights, we assume a solar origin, whereas for fixed line positions up to this threshold we consider an origin from Titan's rest frame. An analysis of the impact of the line depth threshold is presented in the Discussion section 5.1. These are strict criteria that may exclude some potential non-solar lines, with our main concern being to avoid false positive non-solar line detections.

On figures 4.2 and 4.3 we compare sections of the 4 normalised nightly spectra (containing the most intense detected Titan absorption features) with a normalised solar spectrum - and mark with black triangles the lines detected by our method. Figure 4.2 shows line detections at the 5430Å CH_4 band whereas figure 4.3 showcases line detections at the relatively stronger 6190Å CH_4 band. These plots clearly showcase the distinct Doppler shifts of solar absorption lines (coinciding with deep features on the solar spectrum, in black) across observation nights, while unshifted lines across observation nights also do not coincide with spectral features on the solar spectrum, hinting at their origin as absorption lines from Titan's atmosphere. The lack of other main visible molecular absorbers in Titan's atmosphere, as well as their presence upon the spectral regions coinciding with CH_4 known absorption bands (Karkoschka, 1994) (Sánchez-Lavega, 2011) strongly indicates that these detected high resolution lines are previously undetected CH_4 visible absorption lines.

A total of 87 non-solar lines were found on the region covered by the 6190Å CH_4 band, while only 8 non-solar lines were detected at the region covered by the 5430Å CH_4 band. On Tables 4.1 and 4.2 we showcase examples of non-solar line detections, as the top 5 deeper absorption lines detected by our Doppler Line identification method at 2 regions of interest, near 5430Å and 6190Å bands. These tables also showcase the calculated EW for each line (in cm^{-1} units), as well as the estimation for intrinsic line strength, S_i, in cm/molecule units, for both line strength estimation methods (Equivalent Width method and Model Fitting method).

Table 4.1: List of 5 deeper detected lines by our method at the spectral section comprising the weak CH_4 5430Å absorption band. Presented Line Strength, S_i, measurements are retrieved from the Equivalent Width (EW) and the Model Fit (MF) method. Many of these lines are shown detected at the spectral plot of figure 4.2. These spectral lines are likely part of the $6\nu_1+\nu_3$ CH_4 band as described by Giver et al., 1978. The supplementary information table A.1 is a complete table with all 8 detected non-solar lines at the weak CH_4 5430Å absorption band.

Line	Wavelength (Å)	Line Depth (%)	Line EW (cm^{-1})	S_i, EW, (cm/molec)	S_i, MF, (cm/molec)
1	5427.01 ± 0.02	3.8 ± 0.3	0.011 ± 0.003	$(8.5 \pm 2.3) \times 10^{-25}$	$(2.5 \pm 0.5) \times 10^{-25}$
2	5449.49 ± 0.02	2.4 ± 0.4	0.007 ± 0.002	$(5.0 \pm 1.8) \times 10^{-25}$	$(1.0 \pm 0.5) \times 10^{-25}$
3	5430.75 ± 0.02	2.4 ± 0.3	0.009 ± 0.004	$(7.0 \pm 3.0) \times 10^{-25}$	$(1.5 \pm 0.5) \times 10^{-25}$
4	5433.99 ± 0.01	2.3 ± 0.6	0.005 ± 0.003	$(4.0 \pm 2.0) \times 10^{-25}$	$(1.5 \pm 0.5) \times 10^{-25}$
5	5427.49 ± 0.02	2.1 ± 0.1	0.006 ± 0.002	$(4.4 \pm 1.2) \times 10^{-25}$	$(1.5 \pm 0.5) \times 10^{-25}$

Although this detection method was also applied to the even weaker 5760Å and 5970Å CH_4 absorption bands, the relatively smaller line depth of absorption lines on these bands cause its detection to be more challenging. Our algorithm detected only 1 absorption line at each of the 2 CH_4 bands. The complete list of all 97 detected lines at the 4 regions of interest are displayed as supplementary materi-

Table 4.2: Most of these lines are shown detected at the spectral plot of figure 4.3. Presented Line Strength, S_i, measurements are retrieved from the Equivalent Width (EW) and the Model Fit (MF) method. These spectral lines are likely part of the $5\nu_1+\nu_3$ CH_4 band as described by Giver et al., 1978. The supplementary information table S5 is a complete table with all 87 detected non-solar lines at the weak CH_4 6190Å absorption band.

Line	Wavelength (Å)	Line Depth (%)	Line EW (cm^{-1})	S_i, EW, (cm/molec)	S_i, MF, (cm/molec)
1	6182.21 ± 0.01	13.8 ± 0.3	0.033 ± 0.007	(24.7 ± 5.0) x 10^{-25}	(8.5 ± 0.5) x 10^{-25}
2	6183.91 ± 0.01	10.6 ± 0.4	0.020 ± 0.005	(15.5 ± 4.1) x 10^{-25}	(6.5 ± 0.5) x 10^{-25}
3	6177.73 ± 0.00	8.5 ± 0.3	0.017 ± 0.004	(13.1 ± 3.2) x 10^{-25}	(4.5 ± 0.5) x 10^{-25}
4	6184.39 ± 0.01	7.9 ± 0.9	0.018 ± 0.005	(13.5 ± 4.1) x 10^{-25}	(4.0 ± 0.5) x 10^{-25}
5	6183.01 ± 0.01	7.3 ± 0.8	0.023 ± 0.006	(17.7 ± 4.4) x 10^{-25}	(4.5 ± 0.5) x 10^{-25}

als in the Appendix section A: the complete detected line-list for the interest region of 5430Å band is found in table A.1, for the 5760Å interest region in table A.2, for the 5970Å interest region in table A.3, and for the 6190Å interest region in table A.4. Applying our method to the entirety of the VLT-UVES Red arm Titan spectrum (from 5250Å - 6186Å), no extra non-solar absorption line was detected using our method beyond the predicted range of CH_4 bands. This demonstrates the ability of the developed method and algorithm to clearly recognise the difference between the very abundant solar lines and the weaker, unshifted, CH_4 originated on Titan's atmosphere, which are solely found precisely at the regions of interest corresponding to the previously known CH_4 absorption bands.

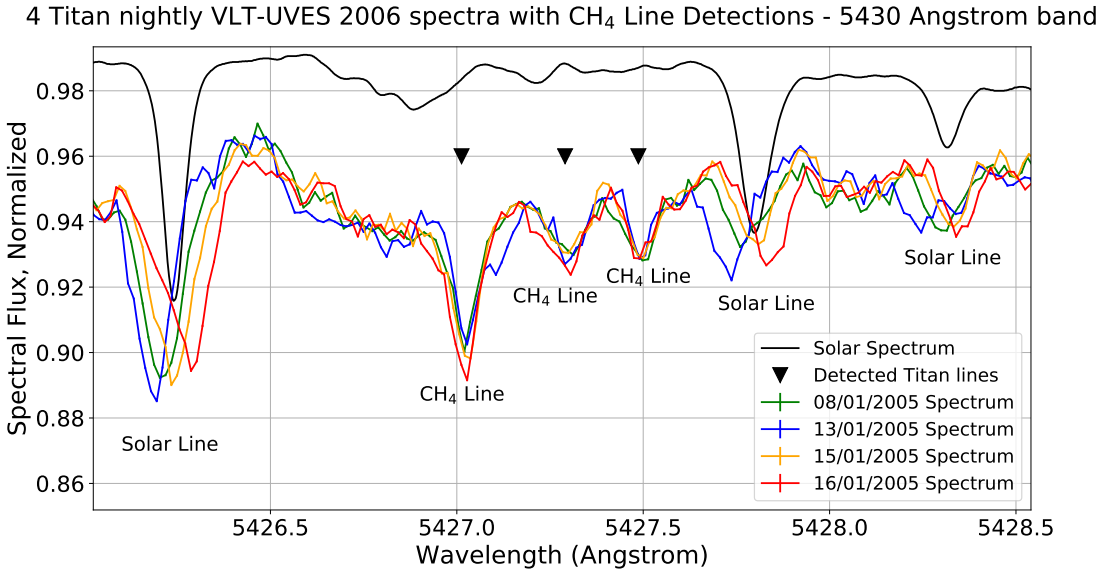

Figure 4.2: Line detection with the Doppler Method for Spectral line identification at a section of the weaker 5430Å CH_4 band, with identification of detected Titan absorption lines with black triangles. In this spectral section we showcase the detection of 3 non-solar features (most likely Titan CH_4 absorption features) next to 3 solar lines of similar depth in accordance with the solar spectrum (in black), which, unlike Titan rest frame absorption features, are Doppler shifted due to the relative motion of the Sun and Titan in different observation nights.

At figure 4.4 is showcased the model fitting method for the measurement of the newly detected spectral lines' Line Strength, S_i. On it we showcase the distinct models in which all newly detected spectral lines are simulated as Gaussian transmittance curves of constant S_i. This S_i value is varied across different models, in order to find the one which better fits (in terms of relative depth) the observed new

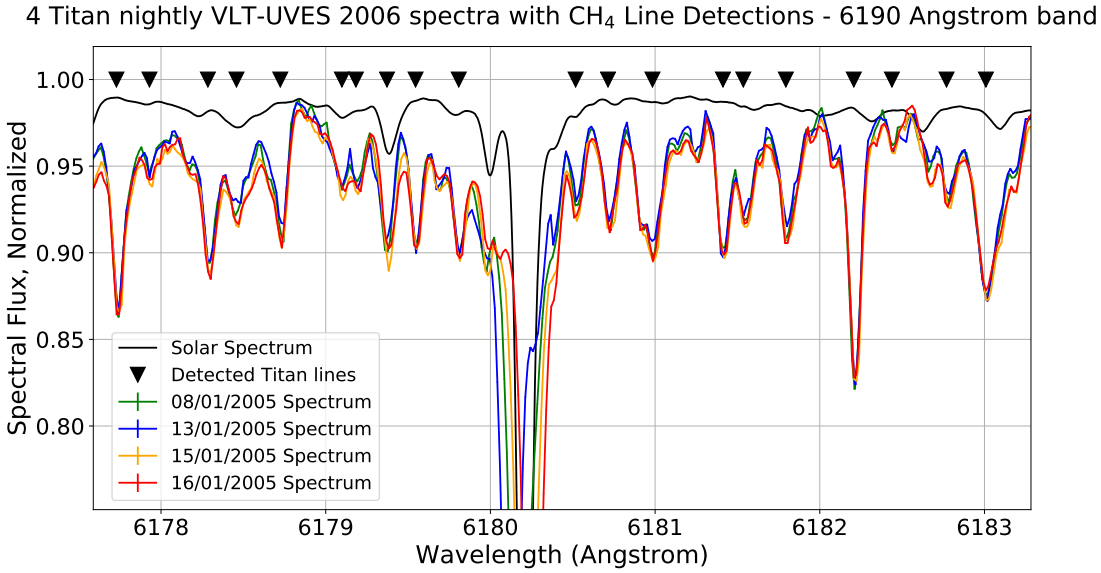

Figure 4.3: Line detection with the Doppler Method for Spectral line identification at a section of the 6190Å CH_4 band. From different nightly spectra with distinct Titan-Sun radial velocities, Solar lines (at 6180.2Å or at 6183.5Å) appear shifted in distinct nights of observation, while lines originating from absorption by Titan's atmosphere (uncorrelated to the solar spectrum) do not appear shifted, allowing their detection through our method (marked with black triangles).

CH_4 absorption line. This fitting is done following Dias et al., 2022 approach, but rather than adjusting gas abundance for known absorption lines (to retrieve the molecular abundances), in this work the line's strength is varied for a fixed, known, column density of CH_4 in the atmosphere, to retrieve the unknown value of each individual line strength, S_i.

An interesting feature of these Gaussian fits is the observation that not all newly detected spectral lines follow a Gaussian-shaped transmission curve at the resolution provided by the 2005 observations of Titan with VLT-UVES. This very evident on the case of the lines observed on figure 4.4 (a zoom in wavelength of the section covered by figure 4.3) well within the CH_4 6190Å absorption band. Very evidently, the absorption lines at 6181.0Å and 6183.0Å are not symmetrical and are far wider than surrounding detected CH_4 absorption lines. This hints at the fact that these observed lines may be, in fact, the result of a sum of 2 or more CH_4 lines that are centred in wavelengths closer than the resolution allowed by the observations of Titan. In some other cases, there may also occur an overlap between Titan CH_4 lines and solar lines (at least for some of the nightly spectra).

We must, therefore, be aware of this limitation of our observations while deriving linelists and line strengths of these newly detected CH_4 lines by observing another planetary atmosphere such as Titan's. A more thorough comparison, analysis and discussion of these results follows, on section 5.1.

4.2 Search for C_3 Absorption Features on Titan's atmosphere

We shall now compare 2018 VLT-UVES Titan spectrum with the solar spectrum (a proxy for Titan's backscattered OFF spectrum, with no molecular absorption) and with the synthetic Titan spectrum combining backscattered solar radiation with synthetic C_3 absorption lines (ON spectrum), to search for C_3 absorption features in the observed spectrum of Titan. In this first case, we considered a C_3 column density in Titan's upper atmosphere equal to the predicted 5.6×10^{13} cm^{-2} by Hérbad et al., 2013 and Dobrijevic et al., 2016 photochemical model, shown in figure 4.5.

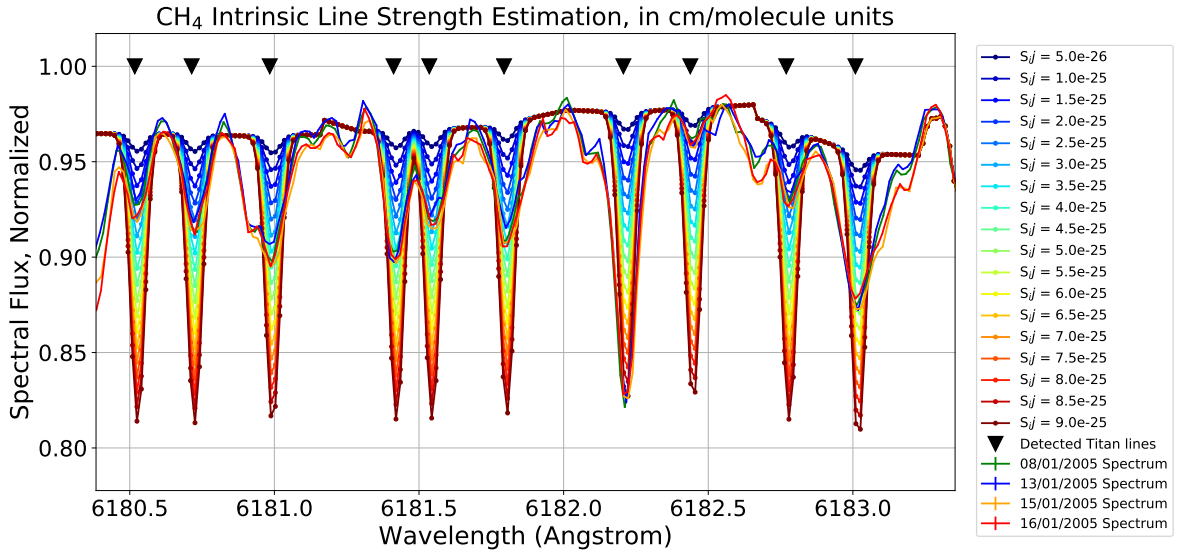

Figure 4.4: Example of intrinsic line strength (S_i) estimation by the Model Fit method for the detected CH_4 lines at the 6190Å CH_4 band by comparing 4 VLT-UVES nightly spectra of Titan with a set of synthetic spectra of Titan with CH_4 lines of constant intrinsic line strength intensity. The estimated value for each line's intrinsic strength value is the S_i value for which the synthetic line better matches the average line obtained from the 4 nightly VLT-UVES spectra of Titan.

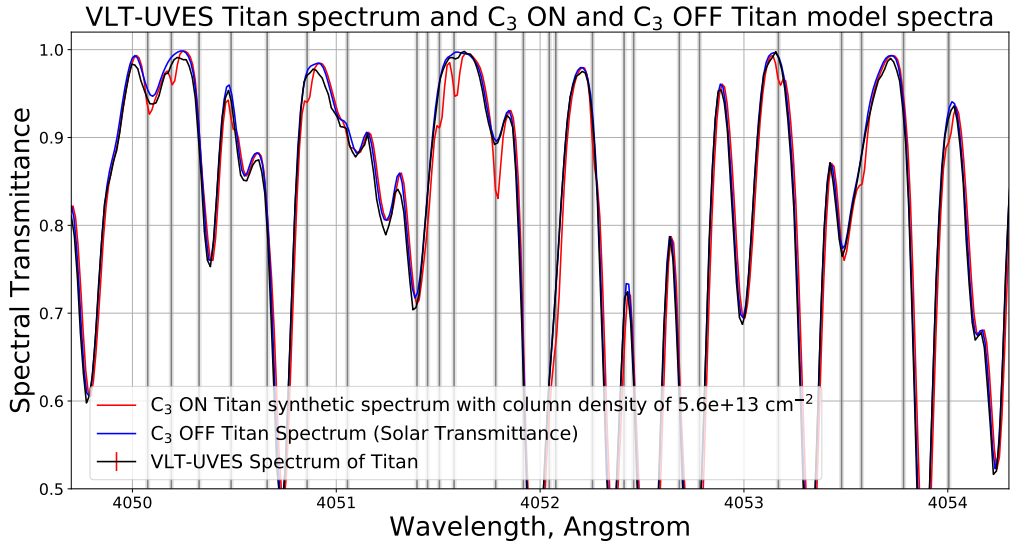

Figure 4.5: Normalised Spectrum of Titan (black) compared with a synthetic normalised spectrum of Titan with a C_3 column density of 5.6×10^{13} cm^{-2} (red) and a normalised solar spectrum (blue) as a proxy for a synthetic spectrum of Titan without C_3 absorption features. Vertical grey lines correspond to C_3 line centres and respective uncertainty identified in Schmidt et al., 2014. No observed spectral features appear to match C_3 absorption lines for the standard abundance of this gas predicted by the Hérbad et al., 2013 and Dobrijevic et al., 2016.

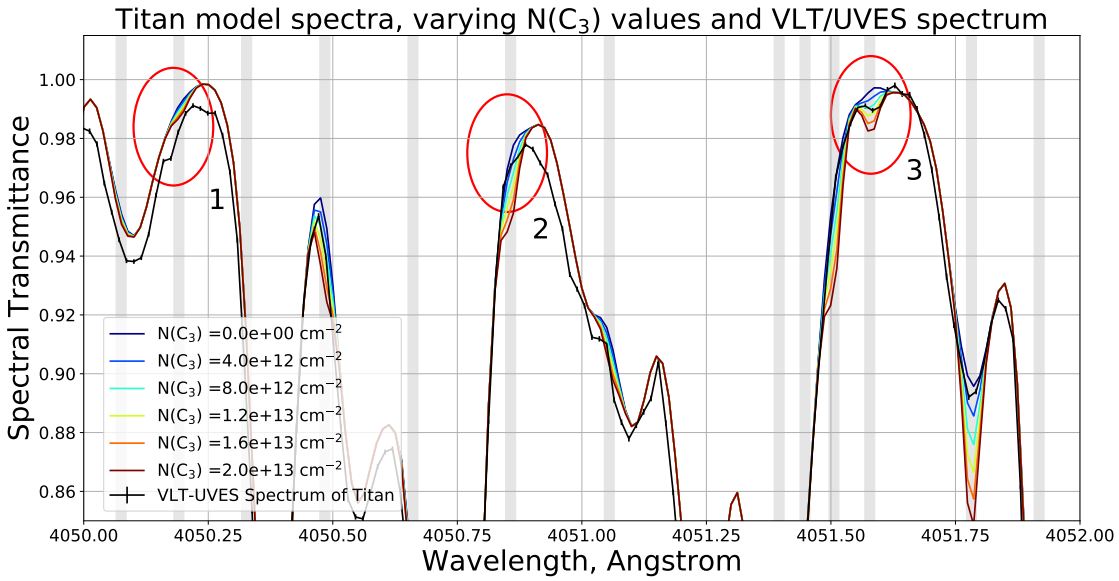

Figure 4.6: Normalised Spectrum of Titan (black) compared with synthetic normalised spectra of Titan for several C_3 column densities, N(C_3), sweeping from 0 to 2.0×10^{13} cm^{-2}, with steps of 4.0×10^{12} cm^{-2}. Vertical grey lines correspond to C_3 line centres and respective uncertainty identified in Schmidt et al., 2014. Red ellipses evidence three possible detections of absorption lines in Titan spectrum that are not explained by backscattered of solar radiation alone — but instead match the expected wavelengths of C_3 absorption lines. Errorbars of 3σ are shown in observational data, with typical width of 0.2% of the continuum.

From this comparison, it is clear that the deep expected spectral absorption features for this C_3 abundance in Titan's atmosphere (in red) are not present in the VLT-UVES disk-integrated spectrum of Titan (black). No comparable absorption features unexplained by solar absorption features appear to be explained by this synthetic spectrum for an upper atmosphere of Titan with the Dobrijevic et al., 2016 predicted C_3 standard abundance. Instead, observations follow much closely the backscattered solar spectrum (blue) at this $\approx 10\%$ absorption line depth scale.

Similar comparison plots between observational, solar and synthetic spectra of Titan were obtained by sweeping through lower column densities values of C_3 abundance in Titan's upper atmosphere, within the range of values predicted by the aforementioned photochemical model Dobrijevic et al., 2016. We have sweept over lower C_3 column density values (between 0 and 2.0×10^{13} cm^{-2}, spaced by intervals of 4.0×10^{12} cm^{-2}) as shown in Fig. 4.6, with the $N(C_3) = 0$ cm^{-2} synthetic spectrum corresponding to the aforementioned C_3 OFF, normalised solar spectrum. There appears to be a match between non-solar features in the observational spectrum and the C_3 absorption features of the synthetic spectrum. These modelled C_3 absorption features appear to match at least three weak absorption features at the VLT-UVES spectrum that are not solely explained by solar absorption lines (marked by three red ovals). These absorption features are statistically significant as all of them hold relative depths 5 to 10 times higher than spectral measurements errorbars (present in the plot with typical values of about 0.2% of the continuum).

Following the example of Dias et al., 2022 detection of of chemical species through chemical retrieval of planetary atmospheres, table 4.3 lists the wavelength centres of the 3 absorption features which do not appear to be explained by solar absorption features. It also compares their positions to the expected centre of Schmidt et al., 2014 C_3 absorption lines, whose positions these observed absorption features appear to match. Titan's backscattered spectral features 1 and 3 appear to closely match in position and

shape the modelled C_3 lines corresponding to transitions R(12) and Q(6), respectively, of C_3 4051Å band - whereas spectral feature 2 correlates in position with line C_3 band R(4) transition, although its shape differs from the modelled C_3 spectral feature. Generally speaking, the VLT-UVES spectrum seems to be better fit by C_3 column densities within the $N(C_3) = (1,0 \pm 0,6) \times 10^{13}$ cm^{-2} range.

Table 4.3: Non-solar absorption features observed in VLT-UVES Blue arm 2018 spectrum of Titan at the spectral range of interest to search for absorption lines part of C_3 4051Å band (left column) with possible correspondence to known lines of the $\tilde{A}^1\Pi_u$ - $\tilde{X}^1\Sigma_g^+$ 000–000 absorption band of C_3, from Schmidt et al., 2014 on the central column. This table also includes the intrinsic line strengths (S_i) of the expected C_3 absorption lines that match the position of the 3 non-solar spectral features, also from Schmidt et al., 2014 (right column).

VLT-UVES Line Centre (Å)		C_3 Line Centre from Schmidt et al., 2014	S_i, (cm/molec)
Line 1:	4050.18 ± 0.02	R(12) @ (4050.191 ± 0.010)Å	1.32×10^{-21}
Line 2:	4050.87 ± 0.02	R(4) @ (4050.857 ± 0.010)Å	1.03×10^{-21}
Line 3:	4051.58 ± 0.02	Q(6) @ (4051.578 ± 0.010)Å	2.42×10^{-21}

At the same time, since all other synthetic C_3 spectral lines fall within deep solar absorption lines, they do not showcase other easily identifiable spectral features of C_3 on the rest of its 4051Å absorption band. This is shown in figure A.1 on the Appendix section, equivalent to the comparison of VLT-UVES spectrum with the solar and synthetic Titan spectrum with a column density of 1.0×10^{13} cm^{-2} of figure 4.6 but covering the rest of the C_3 4051Å absorption band. On this wavelength range of 4052Å to 4055Å, none of the expected C_3 absorption lines appears in a spectral region devoid of much deeper solar spectral lines.

Overall, it is very interesting that on the sole short wavelength ranges where C_3 absorption lines could produce measurable differences on Titan's outgoing spectrum (due to the absence of solar absorption features on those short spectral regions), small measured differences are observed. This hints at the presence of C_3 on Titan's atmosphere, at an abundance within the range predicted by Hérbad et al., 2013 and Dobrijevic et al., 2016 models. On discussion section 5.2 we assess these results in a critical way, and discuss whether they may reliably indicate the discovery of a new molecule on the atmosphere of Titan.

4.3 Thin film simulations of amino-acids - The search for intermolecular structure

After retrieving density profiles of the functional groups within the molecules, these have been plotted together for each set of molecules, shown in the figures below: 3 of these include the functional groups distribution within pure films of the 3 amino acids considered (Gly, Ala, and AABA) and 3 more plots showcase the functional groups distributions of 3 distinct amino acid mixtures (Gly + Ala, Gly + AABA, Ala + AABA).

For the case of glycine - the simplest amino acid with no side chain - only the amine and the carboxyl groups are tracked for the calculation of density profiles, and hence, for this amino acid, only the Nitrogen and the Oxygen atoms positions are tracked. For the case of Oxygen atoms, the average position between the 2 Oxygen atoms is considered, and its retrieved density is scaled down by a factor of 2, so that provided density values are per atom, as shown in the plot of figure 4.7.

The same applies to alanine, but in this amino acid the constituent Carbon on this amino acid's methyl side chain (the β-Carbon) is also tracked, as shown in the plot of figure 4.8. In this plot, the

density distribution of the neutral methyl side chain of alanine appears to be anticorrelated with that of positive and negatively charged amine and carboxyl groups (respectively). This anticorrelation appears to be the starkest at the film-vacuum interface, as, on this time average over a liquid film, the neutral methyl groups cluster outwards with respect to the film. This average alanine molecule orientation of neutral methyl groups pointing outwards and facing the vacuum allows the subsequent concentration of positively and negatively charged amine and carboxyl groups inwards, within the thin film.

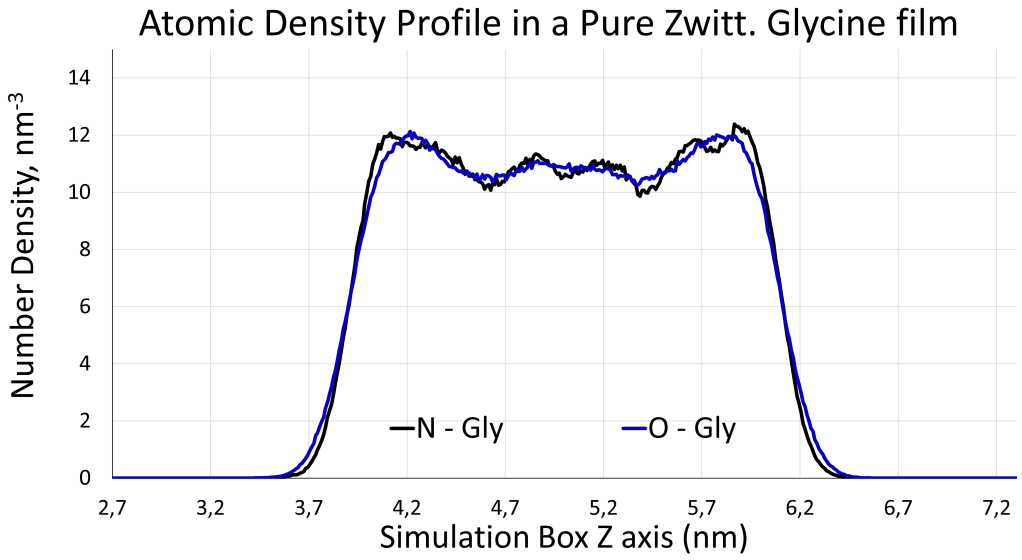

Figure 4.7: Atomic Density Profile of the simulated Glycine thin film (in the zwitterionic state), tracking the time-averaged atomic density in 0.01 nm bins along the 10 nm length of the simulation box. The positions of the Nitrogen atoms (in Nitrogen, proxy for the positive amine group) and of the Oxygen atoms in glycine (in blue, proxy for the partially negative carboxyl group).

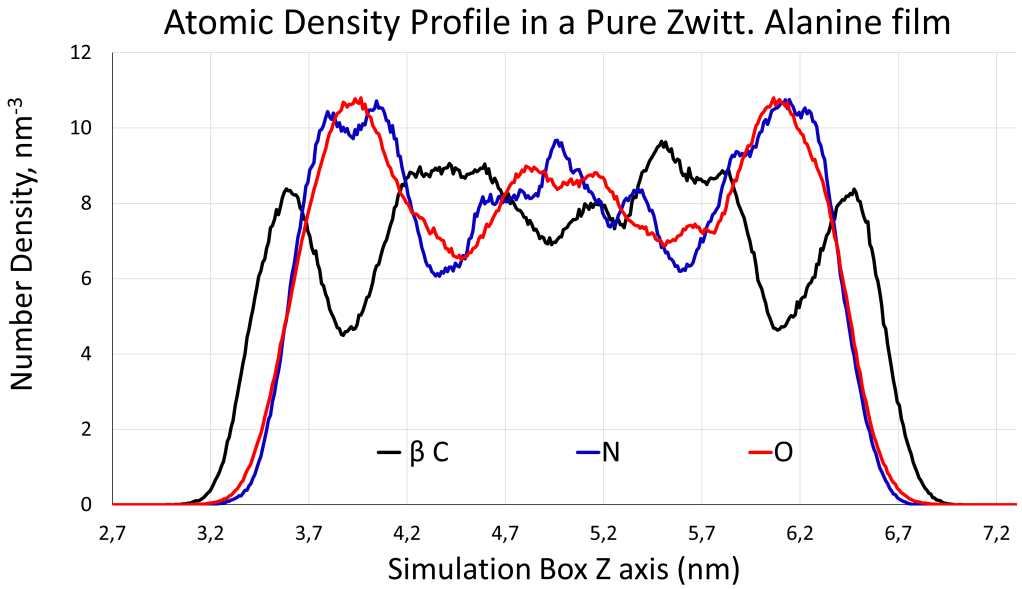

Figure 4.8: Atomic Density Profile of the simulated Alanine thin film (in the zwitterionic state), tracking the time-averaged atomic density in 0.01 nm bins along the 10 nm length of the simulation box. The positions of the Nitrogen atoms (in blue, proxy for the positive amine group), of the Oxygen atoms in glycine (in red, proxy for the partially negative carboxyl group), and of the β-Carbon that comprises the simplest side chain form of any amino acid (in black, a simple, electrostatically neutral methyl group). It is worth noticing that the neutral β-Carbon density profile anticorrelates with the N and O profiles, appearing to form a layer of neutral functional methyl groups on the interfaces with the vacuum.

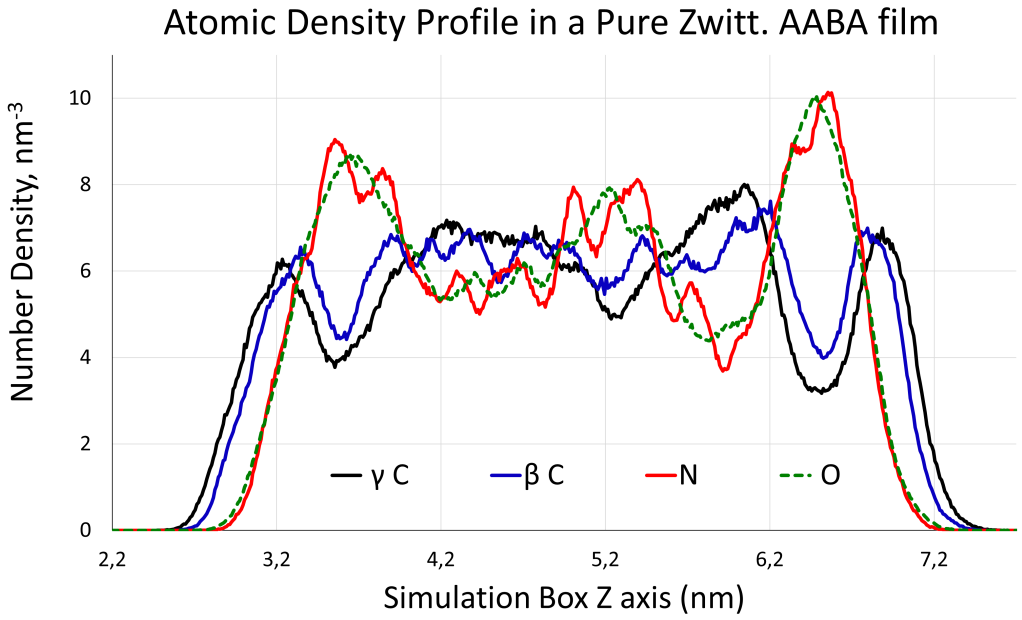

Figure 4.9: Atomic Density Profile of the simulated AABA thin film (in the zwitterionic state), tracking the time-averaged atomic density in 0.01 nm bins along the 10 nm length of the simulation box. The positions of the Nitrogen atoms (in red, proxy for the positive amine group), of the Oxygen atoms (in green dashed lines, proxy for the partially negative carboxyl group), and of the β-Carbon (blue line) and γ-Carbon (black line), that comprise the ethyl side chain . It is worth noticing that the neutral side chain atoms (β-Carbon and γ-Carbon) density profiles anticorrelate with the N and O profiles, appearing to form a layer of neutral functional ethyl groups on the interfaces with the vacuum - with the outermost atom in the film being the end Carbon of the side chain, γ-C.

As for the atomic density profile of the α-aminobutyric acid liquid thin film, shown on figure 4.9, both amine and carboxyl group density are tracked through their Nitrogen and Oxygen atoms (in red and green, respectively). For this case, the neutral ethyl side chain atom's positions were also tracked, by following the β-Carbon (connected to the α-Carbon, central to the amino acid structure) and the γ-Carbon (the final Carbon on the side chain), drawn in blue and black, respectively, at the atomic density profile shown in figure 4.9.

Also on this plot, in particular for the case of the interface regions, there appears to be an anticorrelation between the distribution of the atoms of the neutral side chain (β-Carbon and γ-Carbon) and the charged amine and carboxyl groups. Again, there appears to exist organisation within the liquid film, whereby the electrically charged ends of the zwiterionic amino acids are brought together in the interior of the liquid film, turning its neutral side chains to face the vacuum. This idea is corroborated by the fact that the distribution of the final Carbon atom of the amino acid side chain (γ-C) appears slightly outwards towards the vacuum interface than the innermost atom of the side chain, (β-C).

As for the amino acid mixture film density plots, the same general tendency of having the neutral side chain Carbon atoms clustering outwards on the interface remains, whereas electrically charged amine and carboxyl groups are clustered together on the film's interior, as is showcased on figures 4.10, 4.11 and 4.12. This implies that on a mixture, the molecules with the longest side chains are moved further outwards whereas the amino acid with no side chain (glycine) is concentrated at the film's interior. The organisation also appears to be the greatest in mixture films with molecules with larger side chains, as seen on figure 4.12. This plot showcases an equimolar mixture of Alanine and AABA, where some degree of structure within the whole liquid film is observed, stemming from the film's interfaces with the vacuum all the way across the interior of the liquid film.

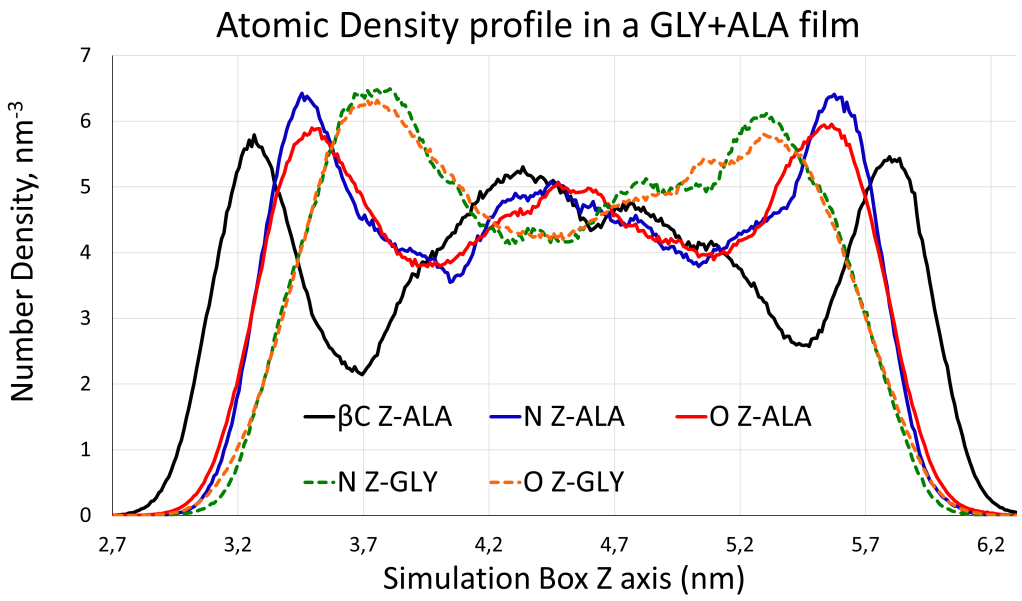

Figure 4.10: Atomic Density Profile of the simulated thin film of an equimolar mixture of Glycine and Alanine molecules (in the zwitterionic state), tracking the time-averaged atomic density in 0.01 nm bins along the 10 nm length of the simulation box. The plot showcases the density profiles of the glycine Nitrogen and Oxygen atoms (green and orange dashed lines, respectively), and of alanine Nitrogen, Oxygen and β-Carbon (blue, red and black thick lines, respectively). It is worth noticing that the alanine β-Carbon, N and O profiles appear to be anticorrelated with the glycine functional groups, clustered further inward on the film. The alanine β-Carbon atoms appear to form a layer of neutral functional methyl groups on the interfaces with the vacuum.

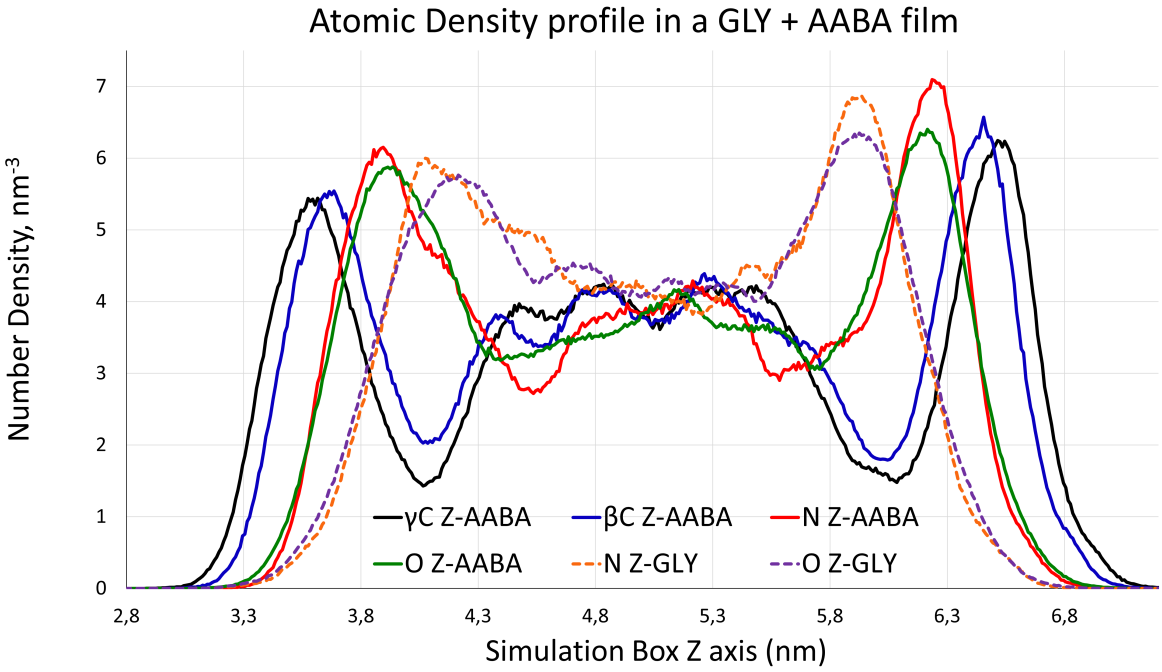

Figure 4.11: Atomic Density Profile of the simulated thin film of an equimolar mixture of Glycine and AABA molecules (in the zwitterionic state), tracking the time-averaged atomic density in 0.01 nm bins along the 10 nm length of the simulation box. The plot showcases the density profiles of the glycine Nitrogen and Oxygen atoms (orange and purple dashed lines, respectively), and of AABA's Nitrogen, Oxygen, β-Carbon and γ-Carbon (red, green, blue and black thick lines, respectively). It is worth noticing that AABA's γ-Carbon and β-Carbon appear to form a layer at the film interfaces, followed by AABA's Nitrogen and Oxygen, and finally glycine's functional groups, clustered further inward on the film.

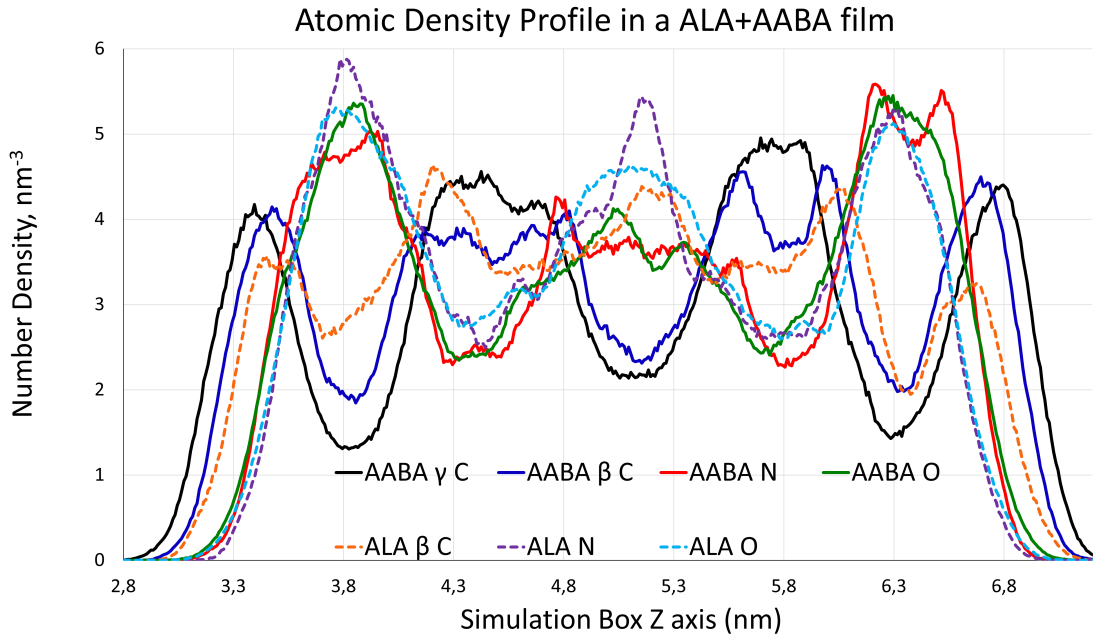

Figure 4.12: Atomic Density Profile of the simulated thin film of an equimolar mixture of Alanine and AABA molecules (in the zwitterionic state), tracking the time-averaged atomic density in 0.01 nm bins along the 10 nm length of the simulation box. The plot showcases the density profiles of the Alanine β-Carbon, Nitrogen and Oxygen atoms (orange, purple and cyan dashed lines, respectively), and of AABA's Nitrogen, Oxygen, β-Carbon and γ-Carbon (red, green, blue and black thick lines, respectively). There appears to arise an anticorrelation between the density profiles of the neutral side chain Carbons on both molecules and the density profiles of electrically charged Nitrogen and Oxygen atoms in both amino acids.

4.4 Film bulk simulations of amino-acids - The search for intermolecular interactions

After conducting the liquid film bulk simulations at NPT conditions of constant temperature T = 600K, the radial distribution function (RDF) of the amine hydrogen atoms with respect to carboxyl oxygen atoms has been retrieved. This profile has been retrieved for atomic distributions in a pure amino acid film bulk for the 3 studied amino acids (Gly, Ala, AABA), but also for simulated equimolar amino acid mixtures. As mentioned in Section 3.3.2, the physical meaning of an RDF corresponds to how much higher the average density of a given atom at a certain radial distance of another interactive centre is with respect to that atom's average density within the entirety of the film bulk (Morgado et al., 2020).

Regarding the amino acid mixtures, it is worth noticing that on these simulations we shall account for the RDF of 2 distinct types of oxygen atoms (from either simulated amino acids) as well as the 2 hydrogen atoms - and hence, for each amino acid mixture simulation, we retrieve 4 RDF from the possible combinations of different amino acid oxygen atoms with distinct amino acid hydrogen atoms. This distinction is important since we aim at understanding how distinct amino acid functional groups interact with each other through Hydrogen bonds (Morgado et al., 2020) - and whether differences in their affinity for intermolecular interactions may explain the distinct reactivity observed in laboratory.

The resulting RDFs are plotted and compared in figures 4.13 (for a Glycine-Alanine mixture), 4.14 (for a Glycine-AABA mixture) and 4.15 (for a Alanine-AABA mixture). As expected, due to the amine group's symmetrical distribution of its 3 Hydrogen atoms, on the RDF plots we observe 2 peaks: firstly a larger and steeper peak near 0,2 nm, corresponding to the typical distance between accepting and donating atoms at an Hydrogen bond (Morgado et al., 2020) - followed by a second shallower peak

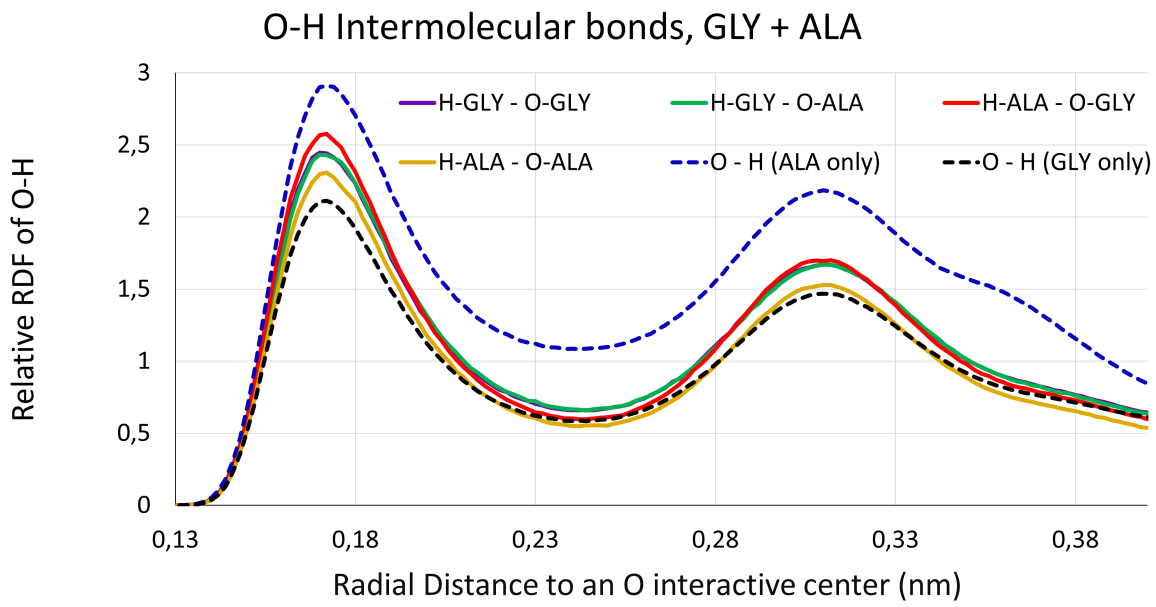

Figure 4.13: Radial Distribution Function (RDF) of Hydrogen atoms with respect to Oxygen atoms at a liquid bulk simulation of an equimolar mixture of Glycine and Alanine (thick lines). Here we showcase the RDF of Glycine Amine Hydrogen atoms and Alanine Amine Hydrogen atoms with respect to Glycine's Oxygen atoms (purple and red, respectively) and the RDF of Glycine Amine Hydrogen atoms and Alanine Amine Hydrogen atoms with respect to Alanine's Oxygen atoms (green and yellow, respectively). These are compared to RDF of pure Glycine and pure Alanine liquid bulk simulations (black and blue dashed lines, respectively).

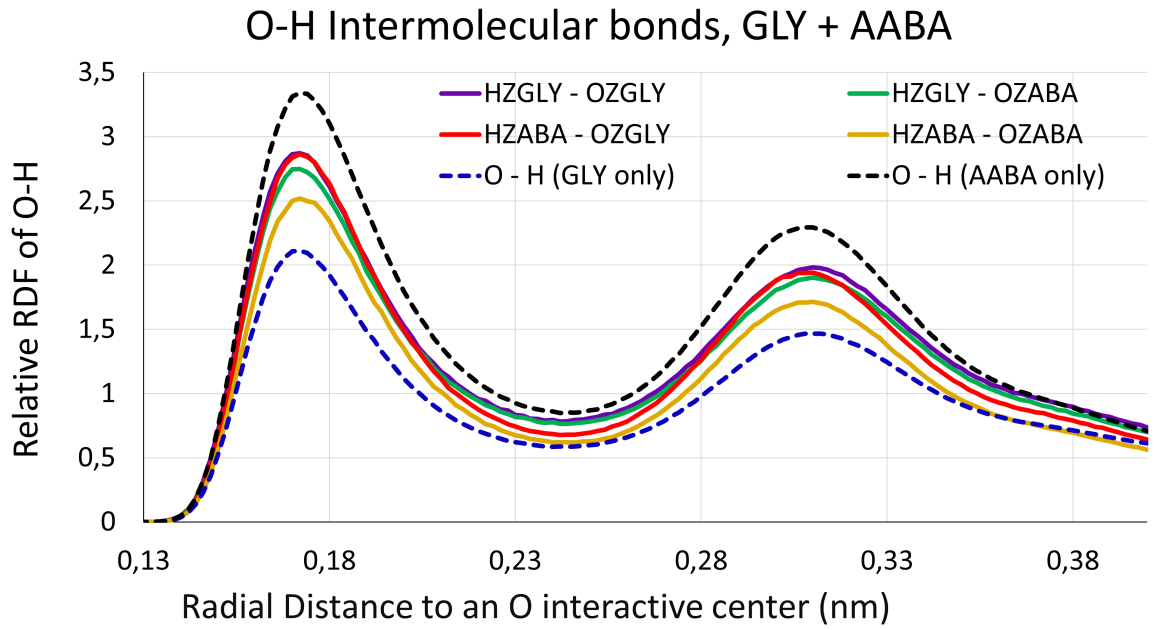

Figure 4.14: Radial Distribution Function (RDF) of Hydrogen atoms with respect to Oxygen atoms at a liquid bulk simulation of an equimolar mixture of Glycine and AABA (thick lines). Here we showcase the RDF of Glycine Amine Hydrogen atoms and AABA Amine Hydrogen atoms with respect to Glycine's Oxygen atoms (purple and red, respectively) and the RDF of Glycine Amine Hydrogen atoms and AABA Amine Hydrogen atoms with respect to AABA's Oxygen atoms (green and yellow, respectively). These are compared to RDF of pure Glycine and pure AABA liquid bulk simulations (black and blue dashed lines, respectively).

corresponding to the radial distance to the remaining hydrogen atoms within the same amine group as the atom undergoing an Hydrogen bond. We shall focus our analysis precisely upon this first peak, since

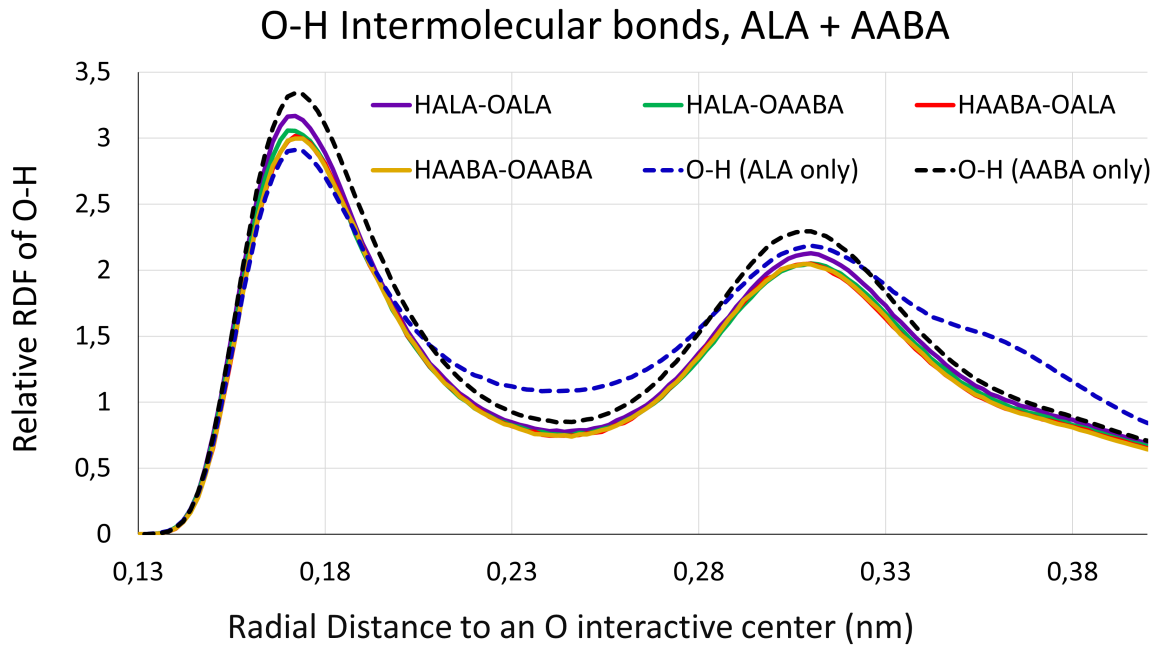

Figure 4.15: Radial Distribution Function (RDF) of Hydrogen atoms with respect to Oxygen atoms at a liquid bulk simulation of an equimolar mixture of Alanine and AABA (thick lines). Here we showcase the RDF of Alanine Amine Hydrogen atoms and AABA Amine Hydrogen atoms with respect to Alanine's Oxygen atoms (purple and red, respectively) and the RDF of Alanine Amine Hydrogen atoms and AABA Amine Hydrogen atoms with respect to AABA's Oxygen atoms (green and yellow, respectively). These are compared to RDF of pure Alanine and pure AABA liquid bulk simulations (blue and black dashed lines, respectively).

it is the one that reflects the nature of the Hydrogen bonds.

Interestingly, regarding the first peak, we observe that the 4 distinct radial distribution profiles of H atoms around O atoms appear to represent intermediate curves between the two curves corresponding to the radial distribution functions of isolated amino acid simulations. This is expected since such an equimolar mixture of 2 polar compounds produces a well mixed liquid with intermediate proprieties regarding their intermolecular interactions (Morgado et al., 2020). We do not appear to observe, nonetheless, a functionally distinct behaviour on any of the mixture RDFs with respect to the other mixture RDF plots - nor with respect to the pure amino acid samples case, that could explain any distinctive photostability differences between mixtures and pure amino acid samples.

At the discussion section 5.3, we perform a further analysis regarding the effective number of close Hydrogen neighbours of Oxygen interactive centres on these simulations so that the average number of Hydrogen bonds per atom can be quantified. Combined with ongoing laboratory experiments, these molecular dynamics simulations will allow us to test our hypothesis that intermolecular interactions may affect the photostability of amino acid molecules under Titan-like conditions.

Chapter 5

Discussion

5.1 High-resolution visible CH_4 line identification in Titan's atmosphere

Motivated by the current lack of high resolution line lists for visible methane absorption bands below 7460Å (Giver et al., 1978) (Hargreaves et al., 2020), during this work a method was developed to identify such CH_4 on Titan spectra. Taking advantage of the Doppler shift affecting solar lines on 4 different nightly high resolution visible spectral observations of Titan, this method distinguishes between shifted solar lines and unshifted (hence non-solar) lines on Titan's rest frame - on parts of Titan's spectrum known to contain CH_4 absorption bands.

Using threshold criteria for detection (maximum line position shift of 25mÅ between all 4 observation nights, as well as minimum line depth of 2% of the spectral continuum) a total of 97 non-solar lines were detected at the 5250Å-6186Å spectral range, all of them within the expected spectral sections corresponding to CH_4 visible absorption bands. The vast majority (87) of these lines is concentrated at wavelengths above 6100Å, precisely at the location of the deeper CH_4 visible absorption band (Giver et al., 1978). In order to assess how detected line depth is distributed as a function of wavelength at the vicinity of this 6190Å band, the plot in figure 5.1 was obtained.

Here we observe that deeper lines progressively cluster closer to the CH_4 band 6190Å centre, while lines below the 2% relative depth threshold appear more dispersed in wavelength. These shallow lines' reduced contrast with respect to the continuum, may indicate that the line detection algorithm may create spurious line detections - some of which will fit the 1st criteria of proximity in position across nightly spectra. Hence the decision of including a minimum line depth threshold of 2% for line detection, a conservative limit ensuring that detected lines are indeed visually unshifted across nightly spectra, as well as visually discernible from the solar spectrum.

Due to the lack of other known relevant molecular absorbers of the spectral section observed by Luz et al., 2006 on Titan's atmosphere apart from methane (McKay et al., 2001), and given the lack of correspondence between the detected line absorption lines present in the solar spectrum (figures 4.2 and 4.3) we conclude that the detected lines are not only non-solar and originated in Titan's atmosphere rest frame, but indeed part of the previously uncharacterised visible absorption bands of CH_4. Given the measurements of isotopic ratios of CH_4 in Titan's atmosphere as retrieved by Niemann et al., 2010, of the $^{12}C/^{13}C$ ratio value of ≈ 90, it is not unreasonable to assume that any $^{13}CH_4$ lines to also be present on these wavelength ranges would be 90 times smaller than equivalent $^{12}CH_4$ lines. It is thus reasonable to consider that the Titan-originated absorption lines detected by our method correspond to previously unknown and uncharacterised visible $^{12}CH_4$ absorption lines.

Indeed, our observations allow to associate and explain some low resolution features of the overtone-

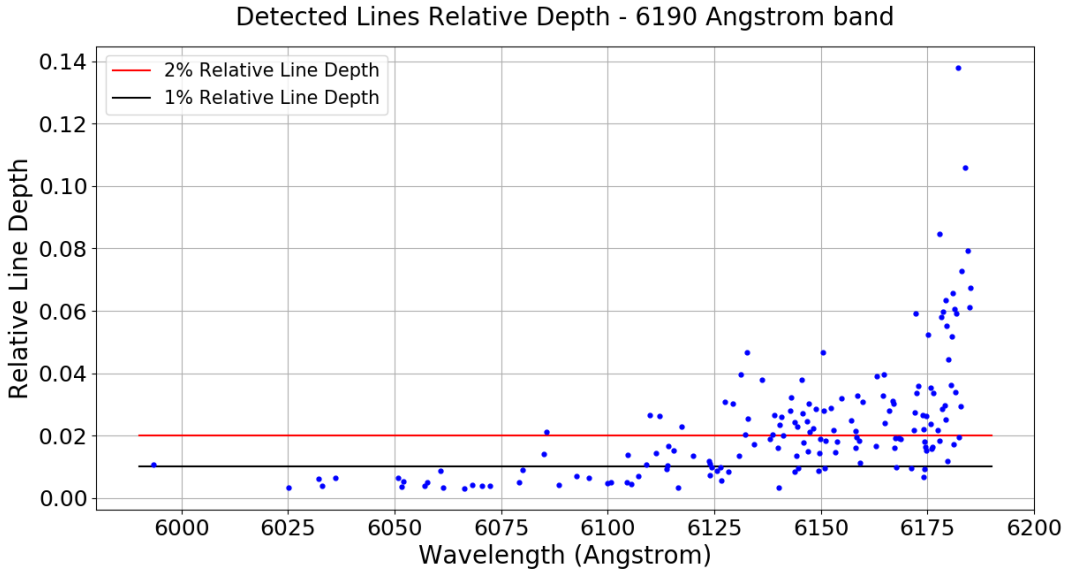

Figure 5.1: Detected line depth as a function of wavelength at the region covering the most intense visible CH_4 band (6190Å band) between 6090Å and 6186Å(with errorbars removed for clarity). Deeper detected lines cluster towards the central wavelength of the methane band at 6190Å (beyond the limits of our spectrum). Weaker lines with depths below 2% of the continuum do not share this clustered nature, suggesting some of them could be spurious line detections. Line detections were therefore considered only for line depths above 2%.

combination bands $5\nu_1+\nu_3$ (6190Å), $4\nu_1+2\nu_3$ (5970Å), $5\nu_1+\nu_3+(\nu_2$ or $\nu_4)$ (5760Å) and $6\nu_1+\nu_3$ (5430Å) previously described in the literature (Giver et al., 1978) (Smith et al., 1990). One such example is the low resolution absorption coefficient "shoulder" feature at $\sim$ 6175Å, described in the $5\nu_1+\nu_3$ band by Smith et al., 1990, and portrayed on figure 5.2. This low resolution feature of sudden decrease of the absorption coefficient κ_{CH_4} at 6175Å, following a less step decrease between 6125Å and 6175Å is replicated in the line depth distribution plot of figure 5.1. Here, maximum line depth appears to stagnate between 6125Å and 6175Å - with a secondary clustering of more intense lines - and increase significantly after 6175Å, where the deeper detected lines seem to cluster, closer to the band centre. Such high resolution line distribution explains the asymmetrical nature of this CH_4 absorption band as had been seen in low resolution by Giver et al., 1978 and Smith et al., 1990.

Another key issue regarding the measurements made during the characterisation of the newly detected CH_4 absorption lines on Titan is the comparison between the two methods for Line Strength, S_i, estimation. On figure 5.3 are shown the measurements of Line Strength through the Equivalent Width Method as a function of line centre wavelength for the Titan lines detected at the 6190Å CH_4 band. A similar plot is shown on figure 5.4 but for Line Strength Measurements obtained via the Model Fitting method. It is interesting that the same "shoulder" pattern observed at figure 5.1 is reflected upon the estimation of Line Strength by both methods - once again allowing to explain the low resolution features on past studies of this CH_4 absorption band (Smith et al., 1990). This tendency is also reflected upon the plot of Model Fitting Line Strength estimation although less evident than in the Equivalent Method estimation, given the discrete nature of the set of models that were fit to the set of lines (each with a fixed value of simulated line S_i).

Interestingly, when directly comparing the estimation of Line Strength from both methods, a systematic difference between the 2 estimation method's results becomes evident, as shown in the plot of figure 5.5. The scattered line strength values showcase a significant shift from a distribution without a systematic difference between estimation methods, which should follow a $y = x$ curve (black line at the

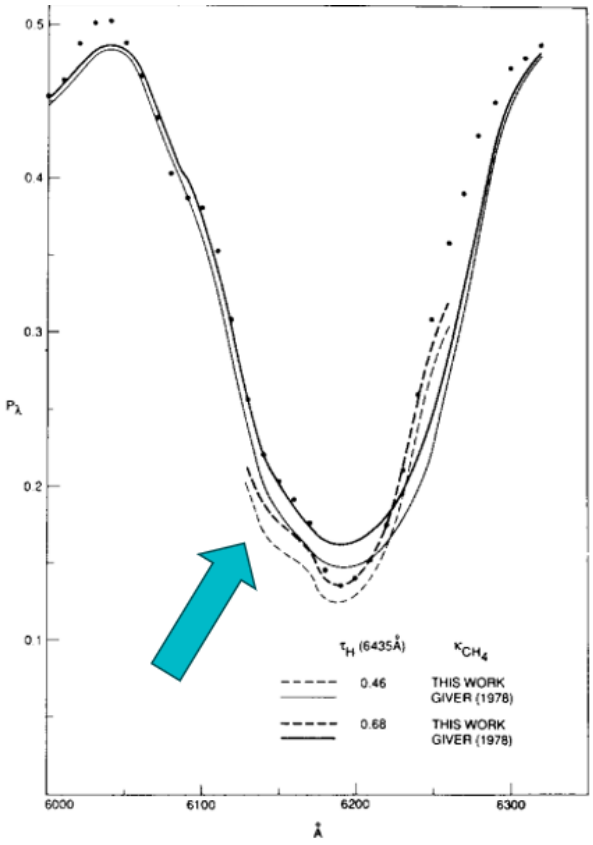

Figure 5.2: Synthetic spectrum of the CH_4 6190Å band in low resolution (as a measurement of continuum absorption) taken from Smith et al., 1990. As it is mentioned on their work, it is possible to observe an absorption "shoulder" between 6125Å and 6175Å, which causes this absorption band to have a markedly asymmetric shape (pointed at by the blue arrow). For the first time, the present work allows the explanation at high resolution of this absorption band's shape, by comparison with a line depth or estimated line strength plot, in which a secondary concentration of more intense lines is observed precisely at 6175Å.

plot of figure 5.5). In fact, for every detected new CH_4 line, the estimated value of Line Strength by the Equivalent Width method is always larger than the value retrieved by the Model Fit method, a difference by a factor ranging from about 1.5 to as high as 6.

It is worth understanding what might be causing such a systematic disparity in results between estimations methods. One possible explanation may be associated with the aforementioned set of unresolved CH_4 lines within the observational set and that may affect differently the measurements done by the two methods. This is since the observation of 2 or more unresolved lines will be observed as a wider, but not proportionally deeper absorption line. Hence, when estimating its Line Strength with the Equivalent Width method and algorithm, the estimated value, proportional to the Equivalent Width, will be far larger than the expected value given the line's depth (assessed by the model fitting method). This is since such lines' equivalent width may actually correspond to the equivalent width of 2 different but unresolved spectral lines. This effect may explain much of the overestimation of line strength using the equivalent width method when compared to model fitting measurements.

It is also observed that the strongest detected CH_4 lines are the ones where the difference between Line Strength estimations by both methods is larger, in particular with respect to the estimations' errorbars. This may hint at another effect that might further explain the deviation between the values obtained by the 2 methods: Unlike the Model Fitting method, the Equivalent Width method builds on the assumption that the probed molecular transitions are optically thin, which allows the simple calculation relating EW and S_i of equation 3.23. For the most intense lines, however, this approximation may no longer be

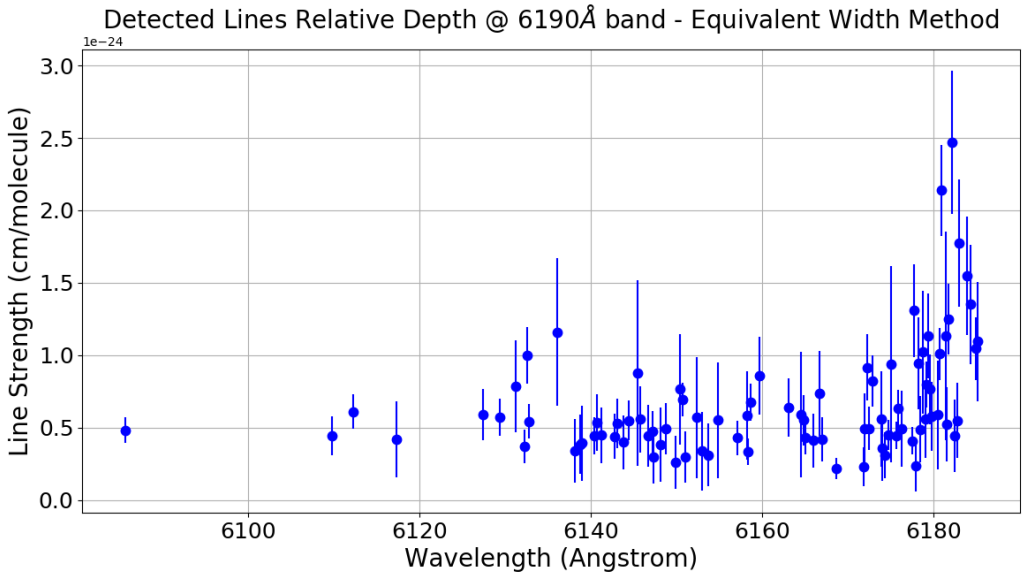

Figure 5.3: Measured Line Strength, S_i, (with the Equivalent Width Method) of detected CH_4 lines as a function of wavelength for the 6190Å CH_4 absorption band.

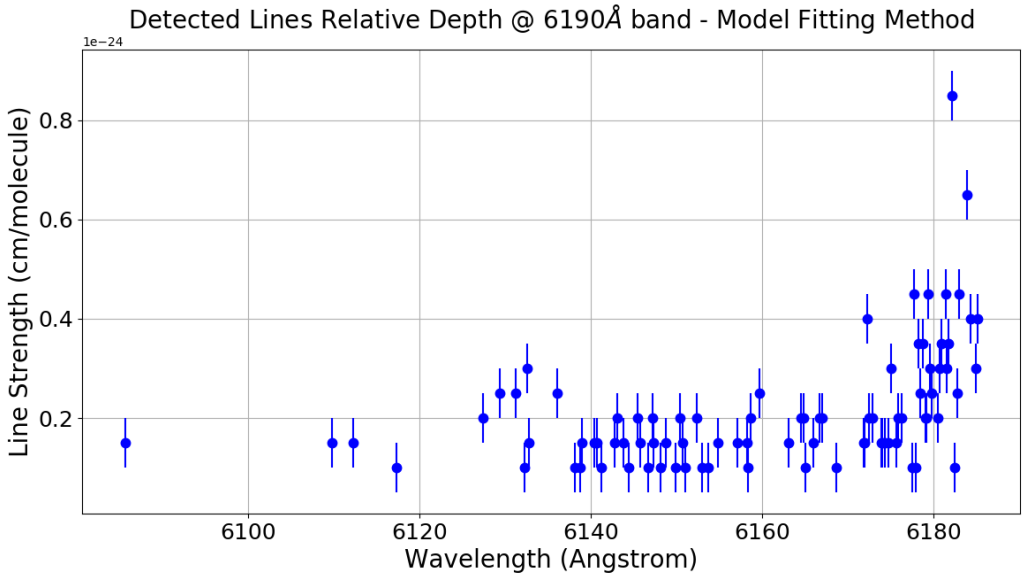

Figure 5.4: Measured Line Strength, S_i, (with the Model Fitting Method) of detected CH_4 lines as a function of wavelength for the 6190Å CH_4 absorption band. It is worth noticing that line strength estimation though the model fitting method necessarily implies a finite set of models, each with its own Line Strength value. Hence, retrieved values shall correspond to the line strength value of the model that was matched the most closely the depth of each line.

valid, as we observe drops of more than 10% in transmittance at this finite resolution. This implies that for the most intense absorption lines, the optical depth could become considerable and not much smaller than 1 as should be the case for the optically thin approximation to stay valid. Hence, it can be argued that the Model Fitting method provides a more accurate approach to the estimation of line strengths for new, previously unknown absorption lines without a sturdy theoretical prediction of its high resolution structure. (Hargreaves et al., 2020).

Although empirical work such as this is not able to deliver the complete picture of the complex nature of the visible, high-energy CH_4 bands, by using high-resolution astrophysical spectroscopy combined to

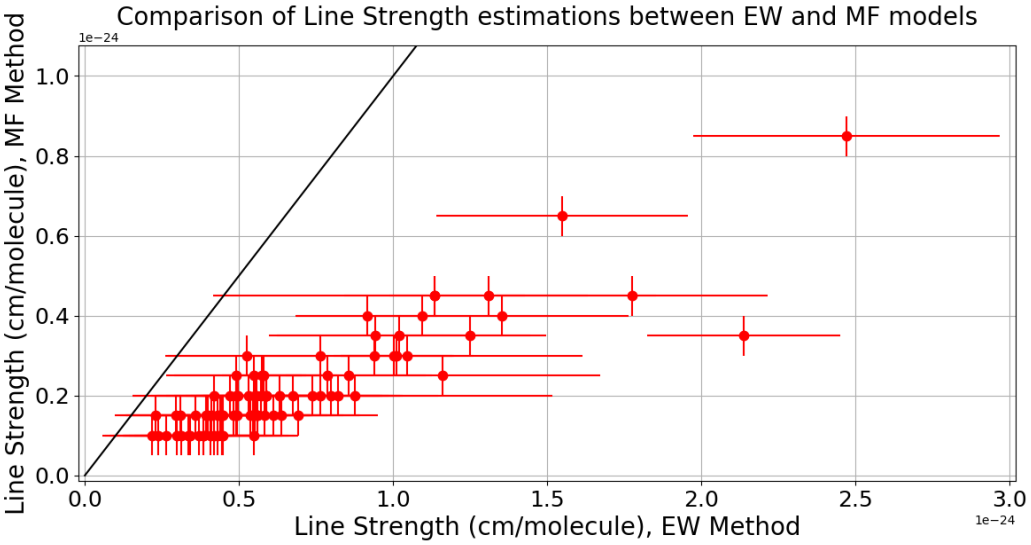

Figure 5.5: Comparison of Measured Line Strength, S_i of detected CH_4 lines as a function of wavelength for the 6190Å CH_4 absorption band by both models used during this study. The x axis corresponds to the Line Strength values estimated by the Equivalent Width (EW) method, whereas the Y axis value corresponds to the Line Strength measured with the Model Fitting (MF) with respective errorbars. These point distribution is compared to a $y = x$ curve, which the measurements should follow if there were no systematic differences between the 2 estimation methods. There is however, a clear deviation from this line, indicating that the values estimated by the EW method are systematically larger than the ones estimated by the MF method.

our simple line Doppler characterisation method, we have been able to gather a high-resolution low Temperature (T < 200 K) line-list of close to 100 CH_4 absorption lines between 5250Å and 6186Å. These results may become a helpful base of comparison for future expansions of CH_4 *ab initio* line-lists into shorter wavelengths. This is of particular importance, given the aforementioned geochemical and astrobiological relevance of CH_4 in current and future studies of exoplanet atmospheres, which at extremely very high resolutions are still circumscribed to ground-based visible observatories.

5.2 C_3 spectral features on Titan's Atmosphere

Following the prolific discovery of new Carbon-based species on Titan, and the predictions from new photochemical models (Hérbad et al., 2013) (Dobrijevic et al., 2016), in this work were analysed dedicated VLT-UVES Blue arm observations in search for the absorption lines of Carbon trimer, C_3 4051Å band on Titan's atmosphere. Comparing the observed Titan spectrum with a solar spectrum and a synthetic Titan spectrum with C_3 between 4050Å and 4055Å, has provided an upper-limit for C_3 column density on Titan's upper atmosphere below the model-predicted $5{,}6\times10^{13}$ cm^{-2}. However, for synthetic spectra of Titan with C_3 column densities within the range of $(1{,}0 \pm 0.6) \times10^{13}$ cm^{-2}, within the model-predicted range of C_3 column densities (Hérbad et al., 2013) (Dobrijevic et al., 2016), it was possible to assess the correspondence between 3 non-solar spectral features on VLT-UVES Titan spectrum and the shape and central wavelengths of 3 C_3 lines from Schmidt et al., 2014.

All 3 assessed spectral features correspondences occur at the small spectral windows where solar transmittance is flat and close to 1, and therefore relatively free from solar spectral features. This is expected since the detection of such weak absorption features (of about 1% of the continuum) requires the absence of other stronger spectral features, particularly as strong as the solar lines found in this spectral region of interest. It is therefore not surprising that other, possibly stronger, C_3 absorption lines are not found in this spectral range of interest due to the overlap with deeper solar lines - given that these

3 regions free of solar lines where tentative detections were obtained are among the sole solar line free spectral ranges found in this region of the spectrum, matching the wavelengths of possible C_3 lines.

Apart from solar features, another possible non-C_3 origin for these spectral features could be other molecular absorber in Titan's atmosphere, for instance uncharacterised high energy CH_4 absorption features. The current nonexistence of line-by-line lists for CH_4 at these wavelengths makes it impossible to completely discard CH_4 weak lines as the source of these observed features near 4051Å. However, it is possible to compare measured line depths at the 5430Å CH_4 band with lower resolution ($\approx$10 Å) absorption cross-section spectra of methane, for instance, He et al., 2021. This comparison allows us to infer the maximum expected depth of CH_4 lines near 4051Å, given methane's absorption measured low-resolution cross-section at this wavelength.

The low resolution CH_4 absorption coefficient (κ_{CH_4}) is of 5×10^{-26} cm/molecule for 5430Å, and of 2×10^{-27} cm/molecule for 4050Å, (He et al., 2021). Hence we can infer a maximum line depth of eventual CH_4 lines at the same wavelengths of the C_3 band to be 25 times lower than that of its 5430Å band. This estimation leads us to expect a maximum line depth of putative CH_4 lines at 4050Å of 0.15%, which is significantly lower than the 0.5% and 1% depths of the non-solar features in figure 4.6. This comparison highlights the importance of the characterisation of CH_4 high resolution visible spectrum when searching for faint visible high resolution molecular absorption features of other molecules in Titan's atmosphere.

Although we cannot claim the detection of C_3 in Titan's atmosphere from these observed spectral features, these results are encouraging and compatible with the existence of C_3 in Titan's upper atmosphere with a column density of about 1×10^{13} cm^{-2}, which is in accordance with previous photochemical models predictions from Hérbad et al., 2013 and Dobrijevic et al., 2016.

Thus, further observations are required to propose a sturdy C_3 detection claim. In case this claim is confirmed, it provides a stringent constraint on one of the photochemical products expected to be found on Titan's upper atmosphere above 600km, as opposed to most sub-mm and infrared spectroscopy detections, which have mostly probed Titan's stratosphere (Lombardo et al., 2019). Ultra-high resolution observations of Titan, at distinct times, when Titan-Sun relative velocities shift differently the deeper solar lines with respect to Titan's rest frame may allow a definitive confirmation of the presence of C_3 absorption features in Titan's spectrum. This could be done by taking advantage of our Doppler Line Identification Method presented above in this work, at the characterisation of weak CH_4 lines.

5.2.1 Preparing new observations

Precisely in order to confirm these tentative detections of 3 C_3 absorption lines in the 2018 VLT/UVES spectrum of Titan, during the context of this Master thesis work, new spectral observations of Titan were prepared for higher resolution visible spectrographs. The chosen instrument was VLT/ESPRESSO, a very high resolution visible spectrograph at the European Southern Observatory Very Large Telescope which is able to reach resolutions of $R \approx 190.000$ with its Ultra High Resolution (UHR) mode (Pepe et al., 2021). This is more than 3 times higher than the resolution achieved by VLT/UVES during its 2018 observations of Titan (Dekker et al., 2000).

Crucially, it was decided that the radial velocity between Titan and the Sun during the observation allowed a Doppler shift that maximised the number of intense C_3 lines coinciding with flat, solar line free sections of the backscattered solar spectrum. Titan's radial velocity with respect to the Sun varies periodically over the course of an orbit from approximately -6km/s to +6km/s. As can be seen on figure 5.6, for a synthetic spectrum of C_3 transmittance obtained at the UHR of VLT/ESPRESSO ($R \approx 190.000$),

a Doppler shift corresponding to a radial velocity of -5km/s between the Sun and Titan should allow a clear detection of 9 deeper C_3 lines due to the displacement of the solar absorption lines. The much higher resolution of VLT/ESPRESSO instrument causes the expected C_3 lines to appear deeper and easier to detect than their VLT/UVES counterparts. This adds to the fact that for this Doppler shift, the wavelengths of the most intense C_3 absorption lines become accessible to our observation by no longer coinciding with deep solar absorption lines. It was therefore intended to observe Titan with a (-5 $\pm$ 1) km/s radial velocity with respect to the Sun, a condition that occurs for about 10% of the time during Titan's orbital period of about 16 days.

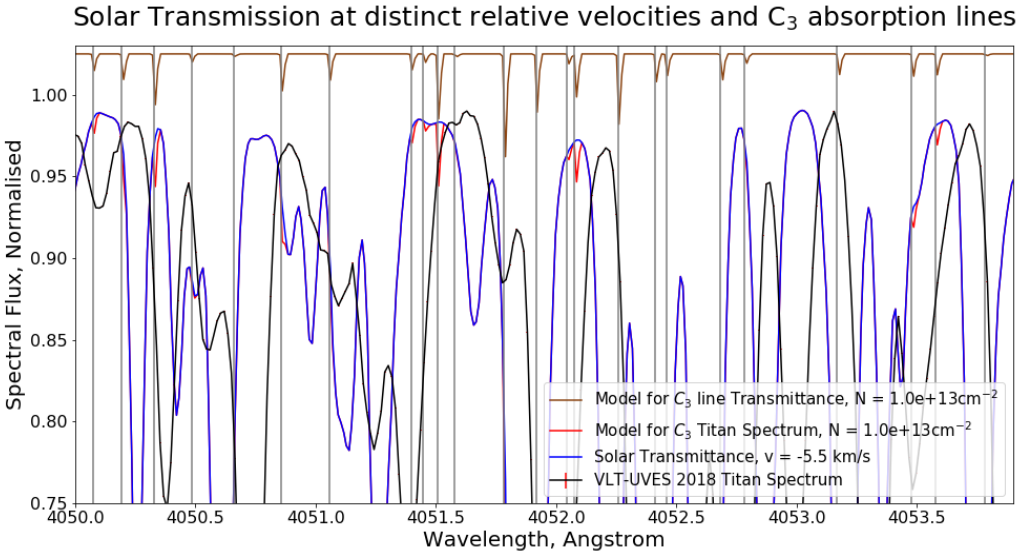

Figure 5.6: Expected Doppler shift of the solar spectrum backscattered from Titan's atmosphere for Titan-Sun relative velocities of -5,5 km/s (blue). Comparison with VLT/UVES 2018 Titan spectrum (black) and model for spectral transmittance of C_3 (brown, moved 2,5% upwards for clarity) and with modelled spectrum of Titan with C_3 (red) at its 405nm band in Titan for a column density of 1×10^{13} cm^{-2} . Vertical grey lines: Schmidt et al., 2014 C_3 lines' wavelengths. 9 C_3 lines cover the detectability criteria of overlapping flat solar spectrum areas devoid of deep solar absorption lines, producing measurable differences for an SNR > 200

Taking advantage of NASA/JPL Horizons System for Solar System Dynamics web interface as well as the StarryNight software, it was possible to obtain a list of observation nights which for the location of Cerro Paranal (where VLT is located) that fulfil the radial velocity condition, while also maximising the quality of the observability of Titan. This implies choosing times when the observed target is the highest in the sky (so that its light travels through a lower atmospheric airmass that affects the quality of the seeing as well as its spectral observations). This also implies choosing times when Titan's angular distance from Saturn is the largest (to avoid field contamination from the much brighter Saturn and its ring system) or even to avoid any proximity to much brighter sources such as the Moon. The best selected dates for observation range from the 28th to the 30th of August 2024, during ESO observation period P113.

In order to understand the required Signal to Noise Ratio (SNR) to conduct these observations so that the C_3 features would be detectable at this higher resolution, the plot of figure 5.7 was obtained. It showcases the radiance difference between the 2 models of Titan's transmittance spectrum, with and without C_3 (at a column density equal to the one estimated from VLT/UVES data in this work), and compares these radiance differences to the limits of measurability for several SNR values. These limits arise as follows: for a SNR = 100, the errorbars will extend to 1% of the measured flux density, and hence

only features corresponding to relative radiance variations above 1% shall have any statistical meaning.

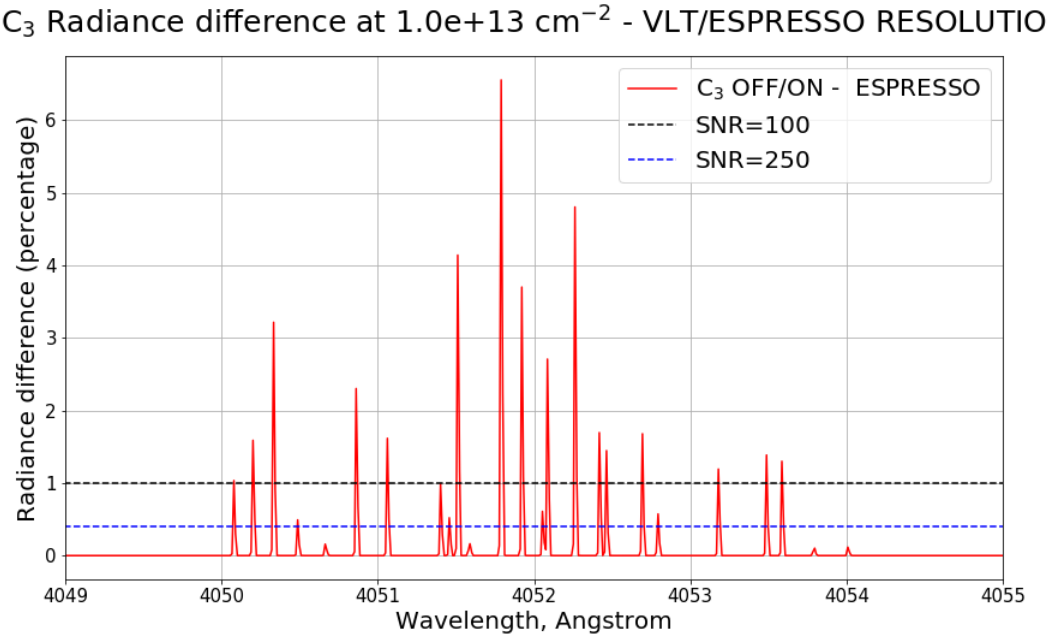

Figure 5.7: Radiance difference relative to the spectrum continuum modelled to be caused by the C_3 4051Å absorption band, as seen by the $R \approx 190.000$ of VLT/ESPRESSO Ultra High Resolution mode - compared with the lower limits of signal detectability given by SNR of 100 (black) and of 250 (blue).

In order to be able to measure most C_3 lines, it was decided to reach a SNR of 250 at the predicted observations. Such SNR implies a larger time of observation, which was calculated using VLT/ESPRESSO exposure time calculator (ETC) (Pepe et al., 2021). Hence, for an average SNR of 250 to be achieved by VLT/ESPRESSO blue arm detector at 405nm, a total of 10 exposures of 1200s (20 minutes), amounting to a total integration time of Titan of 12000s (3h and 20 minutes) during one single observation night were requested at the observing proposal.

Complementary calibration observations were also proposed: one to a nearby field star, 6th magnitude HD 220035, for 2 exposures of 60s, in order to conduct flux calibration, accurately converting the arbitrary units measured by the instrument's detector into physical units. A second calibration observation was also required, this time to observe Saturn's rings (for 2 exposures of 600s) - since these are known to backscatter the solar spectrum without imprinting any extra absorption lines. This will provide a ultra high resolution solar spectrum that will allow an accurate comparison with Titan's backscattered spectrum - so that, if present on Titan's spectrum, C_3 absorption lines will be detected. Thus, including instrument overheads (non-integration time the telescope and instrument take performing tasks related to observations, such as readout time, telescope pointing and dark and flat frames exposures) a total of 4h, 15 minutes and 45 seconds were requested, and the proposal, submitted by the 26th of September 2023 is currently under evaluation.

5.3 Intermolecular structure and interactions of amino-acid films

Motivated by the current experimental work performed by the IST Astrobiology team regarding the photostability of amino acids under Titan's surface conditions, a set of molecular dynamics simulations were conducted in order to replicate the intermolecular interactions between amino acids in a thin molec-

ular film. 2 sets of simulations were conducted: the first set, simulating thin amino acid liquid films in order to probe their structure, emerging from intermolecular interactions; and a second set, aimed at quantifying the amount of Hydrogen bonds being established between amino acid molecules at a liquid bulk.

For both simulation types the main focus was finding some aspect within the simulation results that could explain previous experimental work by Kate et al., 2005 and later support the experimental work currently being performed by the Astrobiology group at IST. This was since irradiation experiments have pointed at a larger photostability of glycine and AABA when compared to Alanine - a puzzling result since this molecular species is structurally intermediate between glycine and AABA (Kate et al., 2005). Furthermore, other works have also shown that intermolecular forces (such as the hydrogen bonds probed here) have the potential to affect molecular photostability (Golec et al., 2018).

Firstly assessing the results from the thin film structure results, it can be observed from figures 4.7 to 4.12 that even in a liquid film, the very polar nature of these amino acids in their zwitterionic state sparks some degree or organisation along the film's width. Such organisation within the film appears to be caused by the average orientation of the polar sides of the amino acids towards each other, which minimises the general electrostatic energy of the system. This causes the neutral side chains to be moved out, forming most of the thin film's interface with the vacuum. This effect is the most evident at the mixture of amino acids with the larger neutral side chains (alanine + AABA, figure 4.12) promoting an average organisation within the film that extends across the entirety of its width.

The thin film simulations provide an interesting insight onto the emergence of structure within amino acid films. Notwithstanding, they do not appear to showcase any particularly distinct effect on the intermolecular interactions between alanine and the remaining species (as a way to explain its easier photochemical degradation). Nor do the results show any clear difference for the amino acid mixtures with respect to pure samples, such that one could draw a link between a putative structural difference within the mixture film and a greater potential for photodegradation.

Analysing instead the film bulk liquid simulations, it was possible to retrieve radial distribution function (RDF) plots of the amine Hydrogen atoms distribution on the vicinity of carboxyl oxygen atoms - a proxy for the intensity for hydrogen bonds established between the molecules - for both pure samples and amino acid mixtures, shown in figures 4.13, 4.14 and 4.15. On these figures, for each amino acid mixture, were plotted the radial distribution functions of the 2 distinct molecules amine's Hydrogen atoms with relation to either amino acid's oxygen atoms. These 4 distinct RDFs are compared with the RDFs of simulated pure samples of the 2 amino acids in question.

As expected, a 2 peak radial distribution is observed for all plotted liquid bulk simulations - with the steepest and closer peak corresponding to the atoms undergoing a hydrogen bond with the carboxyl oxygen (at a characteristic radial distance of about 0,2 nm) and with the second, more distant and shallower peak (at a typical radial distance of 0,3 nm to an Oxygen atom) corresponding to the positions of the other Hydrogen atoms in the same amine group as the hydrogen atom forming an Hydrogen bond, in accordance to previous molecular dynamics simulations of amino acid ionic liquids (Herrera et al., 2016). Interestingly, it is also possible to observe that RDF profiles of H atoms in the vicinity of O atoms within an amino acid mixture tend showcase a behaviour intermediate between the the profiles of the 2 pure amino acid samples - which is expected for a well mixed liquid (Morgado et al., 2020), as had been mentioned at the results section. This could be interesting since we observe a larger density increase in H atoms density surrounding O atoms in glycine when mixed with alanine or when mixed with AABA, compared to its pure state.

But although these radial density profiles provide an interesting indication of the relative densities of

Table 5.1: Average number of H neighbours to a O atom within pure liquid film bulk simulations, with typical uncertainty of ± 0,02. For simulated mixtures, the value presented under each amino acid corresponds to the average number of hydrogen atoms forming a H bond to the given amino acid Oxygen atoms, within the liquid mixture.

	Glycine	Alanine	AABA
Pure sample	1,74	1,88	1,52
Gly + Ala mixture	1,65	1,57	—
Gly + AABA mixture	1,68	—	1,56
Ala + AABA mixture	—	1,56	1,53

hydrogen molecules intervening in H bonds, these density profiles can nonetheless be deceiving regarding their interpretation, since, calculated as they were, the radial density profiles of distinct simulations (for instance, pure amino acid samples and mixtures) cannot be compared directly. This is due to the distinct sizes of the molecules in question, for in order to keep a constant pressure, the simulation box sizes were varied differently under the action of the Parrinello-Rahman barostat (Parrinello et al., 1981) across distinct simulations. For reference, at the Gly + AABA mixture simulation, the cubic box side size stabilised at 3,66 nm - whereas this value was of 3,99 nm for the pure AABA bulk simulation and 3,29 nm for the Glycine simulation - with a typical variability in box size for the simulations not larger than ± 0,005 nm. This alters the average hydrogen number density within the box, affecting the RDF plots.

Therefore, in order to accurately quantify the the average number of hydrogen bonds established within pure and mixture simulations, we shall count the number of hydrogen neighbours N_H on the first peak of all Radial Distribution Functions. This is done by inverting equation 3.31 and integrating $N(r, r+dr)$ up to the local minimum between the first and second peak (at a radius of 0,242 nm), resulting in equation 5.1, where 1200 is the number of amine H atoms in the 400 simulated amino acids and a accounts for the length of the simulation box size.

$$N_{Hbonds} = \int_0^R N(r, r+dr)dr = \int_0^R RDF(r) \cdot \frac{V(r, r+dr)}{n_H} dr = \int_0^R RDF(r) \cdot \frac{V(r, r+dr) \cdot 1200}{a^3} dr \quad (5.1)$$

The number of hydrogen neighbours provides a direct measurement of the average intensity of formed hydrogen bonds between amino acid molecules on this liquid bulk. In table 5.1 we present the values of the average number of hydrogen atoms in the close neighbourhood (within the first peak region, up to a radial distance of R = 0,242 nm) of oxygen atoms for the pure amino acid simulations and for the amino acid mixtures. Since the simulation software GROMACS does not provide uncertainties or typical dispersion values when retrieving Radial Distribution Functions, it is challenging to attribute a typical uncertainty value for the calculated number of the average number of H neighbours to an O atom. As the sole associated uncertainty to the calculation of the number of neighbours was the box size variation (Δa), not larger than 0.005 nm, the effect of this sole uncertainty was propagated through equation 5.1, (for the maximum RDF value) corresponding to an uncertainty of ± 0,02 in the value of H neighbours stemming from the box size variation.

Taking into account the values of Hydrogen atom neighbours of Oxygen atoms (as a measure of H bonds forming within the simulated liquid bulk), 2 main effects can be pointed out: Firstly, regarding the pure liquid bulk simulations, the structurally intermediate alanine appears to form, on average, the most intermolecular hydrogen bonds within the liquid bulk - followed by glycine and then by AABA. Although this stands out, given alanine's intermediate structure, is nonetheless unclear how an 8% increase in

hydrogen bonds could explain the sharp decrease in alanine photostability, when compared to other amino acids (Kate et al., 2005). The ongoing laboratory work by the Astrobiology group at IST may provide further insight on whether these simulation results, of an increased number of hydrogen bonds in Alanine films, may indeed be related to Alanine's lower photostability.

Secondly, both glycine and alanine appear to form slightly less hydrogen bonds when in mixture than when in their pure state (a decrease of about 6% for H neighbours of glycine Oxygen atoms and of about 17% for the case of alanine). The number of H bonds with AABA molecules stays roughly unchanged in its pure and mixture state. Despite previous laboratory and simulation work on Hydrogen bonds in amino acid ionic liquids (Ohno et al., 2007) (Herrera et al., 2016), direct comparisons cannot be drawn between these previous works and ours, since no literature on glycine, alanine or AABA pure or amino acid mixture samples has been found.

However, these neighbour calculations, aimed at quantifying the H-bonds established between amino acids have confirmed the general observations drawn from the molecular dynamics simulations of thin-film structure analysis and the radial distribution functions of the liquid film bulk: No significant increase in intermolecular interactions occurs in amino acid mixtures when compared with their pure state. On the contrary, both pure samples of glycine and alanine appear to form more intermolecular H bonds than any of the mixtures, and glycine's intermolecular interaction with AABA appears to be no different than its interaction with alanine. A possible reason for this increased intermolecular interaction in a pure amino acid sample could be due to the molecules' geometrical distribution of charges, that may facilitate intermolecular interactions with molecules with a shape more similar to its own (Morgado et al., 2020). Thus, these simulation results provide a relevant comparison with ongoing laboratory work: Should this laboratory work observe any alteration of amino acid photostability in amino acid mixtures, then these simulation results suggest that such an impact in photostability would be caused by a distinct effect, other than intermolecular interactions at the amino acid films.

It is also important to mention the large set of approximations conducted during this preliminary approach towards understanding the intermolecular nature of these amino acid films. Despite our arguments for the equivalence of the structural nature of a liquid amino acid film to its amorphous solid nature (Rodrígez-Lazcan et al., 2012) the difference of 500K between the simulations "in silico" and the amino acid films used at the irradiation experiments is still very considerable. Furthermore, the atomistic OPLS-AA based molecular simulations do not include any quantum effects - which are at the very core of the photochemical interaction that sparks the phenomenon of photolysis in study, as well as what regards the reactivity between molecular species. For a follow up study, Schrodinger Equation-based *ab initio* calculations could provide a more realistic insight on the nature of the photochemistry and reactivity of these amino acids of interest (Friesner et al., 2005).

Chapter 6

Conclusions

In the context of this master thesis work, an exploration of the complex chemistry and emerging prebiotic complexity of the icy moon Titan was conducted. Titan's atmospheric methane is one of the most important stages of its geochemical methane cycle, as it is photolysed by incoming UV solar radiation, (Lunine et al., 2008) (Hörst, 2017). This photolysis sparks a network of atmospheric chemistry that has produced the tens of hydrocarbon, nitrile and organic molecular species already detected using distinct techniques of Astrophysical spectroscopy (Nixon et al., 2013) (Lombardo et al., 2019).

As an important geo- and biosignature (Thompson et al., 2022) CH_4 is widely searched in for planetary atmospheres, within and beyond our solar system in Infrared wavelengths - despite the fact that the scientific community lacks a visible high resolution spectrum of CH_4 on visible wavelengths (Hargreaves et al., 2020). Hence, during the course of this work, very high resolution archived spectra of Titan ($R = 100.000$) were processed and analysed in search for new high resolution methane absorption lines in previously known (in low-resolution) CH_4 absorption bands centred at 5430Å, 5760Å, 5970Å and 6190Å (Giver et al., 1978).

In a backscattered visible spectrum of Titan, crowded with deep solar spectral absorption lines, a new Doppler shift-based method was developed in order to distinguish between solar absorption lines (which suffered distinct Doppler shifts over several observation nights) and Titan CH_4 absorption lines (which, originated at Titan's frame of reference, do not suffer Doppler shifts from nights of observations). Thanks to this new method it was possible to identify 97 new CH_4 absorption lines, whose line strength was estimated through 2 distinct estimation methods, one based on the detected line's Equivalent width (EW method), and another relying on fitting a spectral model of this absorption band (MF method). The systematic difference between line strength measurements performed by both methods has been assessed and several explanations have been put forward to explain this difference - in general, concluding that due to the set of approximations taken with the EW method, the MF method is likely a more robust approach to estimating new line strengths.

Regardless of the line strength estimation method used, the distribution and intensity of the detected lines at CH_4 6190Å band appear to explain the low resolution features observed on this band described on previous works (Smith et al., 1990). This master thesis work presents therefore the development of a new method for spectral line identification that allows an empirical expansion of high resolution line by line lists of molecules present in other solar system objects. It showcases as well a successful first demonstration of the usage of this method to empirically expand our knowledge of the visible spectrum of CH_4, one of the most important molecules for the study of planetary atmospheres temporal evolution in icy worlds and gas giants, and a biosignature in rocky planets.

This analysis was followed by the processing of more recent, dedicated VLT/UVES observations

of Titan in very high spectral resolution (R = 60.000) at the blue end of the visible spectrum, in search for the transient tricarbon molecule, C_3. C_3 is a missing link in the current understanding of Titan's upper atmosphere high energy photochemical pathways between hydrocarbons (Hérbad et al., 2013) (Dobrijevic et al., 2016) which was yet to be detected in any planetary atmosphere (D'Aversa et al., 2017). Given its transient nature, reduced spectral information regarding the C_3 visible absorption band at 4051Å was available, and hence its absorption spectrum was simulated by a simple, 1-layer atmospheric radiative transfer model developed over the course of this work.

Fitting a model of Titan's backscattered spectrum with and without C_3 absorption to the processed data has allowed the detection of 3 spectral features unexplained solely by the backscattered solar spectrum, but which could be explained by C_3 absorption lines. Model fitting to these lines has therefore provided the first tentative detection of C_3 in any planetary atmosphere at C_3 column densities of $(1{,}0 \pm 0{,}6) \times 10^{13}$ cm^{-2}, which falls within the predicted range from recent photochemical models of Titan's upper atmosphere (Dobrijevic et al., 2016). Given the reduced number and shallow nature of the tentatively detected C_3 features in Titan's spectrum, observing proposals for new observations of Titan at ultra high resolution (R = 190.000) were submitted to ESO's VLT/ESPRESSO instrument (Pepe et al., 2021). Its goal is to confirm this important detection for the study of high energy photochemistry on Titan - a process akin to the one that is thought to have occurred on early Earth, promoting the abiotic synthesis of organic matter, thought to have contributed to the origin of life on Earth (Hörst et al., 2012) (Ali et al., 2015).

The astrobiology community's interest in Titan is not restricted its very interesting atmospheric chemistry, nonetheless. Laboratory experiments in analogous conditions to Titan have suggested the synthesis of organic molecules such as amino acids though atmospheric chemistry (Hörst et al., 2012), which might endure deposition upon Titan's icy surface. Aiming at understanding the fate of amino acids deposited upon Titan's surface, this master thesis work contributed with a study of molecular dynamics simulations of amino acid films.

Using the GROMACS molecular dynamics simulation software, it was possible to simulate thin amino acid films and liquid film bulks of Glycine, Alanine and α-Aminobutyric acid (AABA) in pure and mixed equimolar samples, to study how the intermolecular interactions between these zwitterionic amino-acids affected the structure of the films - by tracking the hydrogen bonds established between amino acids. It was observed that (structurally intermediate) alanine molecules formed, on average, more hydrogen bonds in a pure film than glycine and AABA. We also report that it was not observed an increase in intermolecular hydrogen bonds when mixing amino acids under Titan-like conditions. Future studies with more complex *ab initio* simulations may provide a clearer picture for the mechanisms of amino acid degradation in thin films deposited in icy moon's conditions.

To conclude, this master thesis work has allowed a very prolific opportunity to learn new techniques and methods for the study of the fate of organic molecules in extraterrestrial environments through molecular dynamics simulations, and for the study of planetary atmospheres, such as High Resolution Spectroscopy. The application of these techniques to solar system targets and case studies is crucially complementary to future exploration studies regarding the potential habitability of icy moons on the solar system and future surveys of exoplanet atmospheres across the galaxy.

Bibliography

Aboudarham, J. and C. Renié (2020). "BASS2000, database of Solar ground-based observations. BASS2000." In: DOI: https://doi.org/10.25935/9TXJ-F095.

Abrahams, M. et al. (2015a). *GROMACS User Manual version 5.0.7*. www.gromacs.org.

— (2015b). "GROMACS: High performance molecular simulations through multi-level parallelism from laptops to supercomputers". In: *SoftwareX* 1-2, pp. 19–25. DOI: https://doi.org/10.1016/j.softx.2015.06.001.

Ali, A. et al. (2015). "Organic chemistry in Titan's upper atmosphere and its astrobiological Consequences: I. Views towards Cassini plasma spectrometer (CAPS) and ion neutral mass spectrometer (INMS) Experiments in space". In: *Planetary and Space Science* 109. DOI: DOI:10.1016/j.pss.2015.01.015.

Allen, M. and D. Tildesley (1991). *Computer simulation of Liquids*. Clarendon Press, Oxford, UK.

Atkins, P. et al. (2013). *Chemical Principles, 6th edition*. W.M. Freeman and Company, New York, USA.

Barnes, J. et al. (2021). "Science Goals and Objectives for the Dragonfly Titan Rotorcraft Relocatable Lander". In: *The Planetary Science Journal* 2, p. 130. DOI: 10.3847/PSJ/abfdcf.

Berendsen, H. et al. (1984). "Molecular dynamics with coupling to an external bath". In: *J. Chem. Phys* 126, pp. 3684–3690. DOI: https://doi.org/10.1063/1.448118.

Bussi, G. et al. (1984). "Canonical sampling through velocity rescaling". In: *J. Chem. Phys* 126, p. 014101. DOI: https://doi.org/10.1063/1.2408420.

Célia-Silva, L. et al. (2020). "Preaggregation of Asphaltenes in the Presence of Natural Polymers by Molecular Dynamics Simulation". In: *Energy Fuels* 34, pp. 1581–1591. DOI: https://doi.org/10.1021/acs.energyfuels.9b03703.

Cordiner, M. et al. (2015). "Ethyl Cyanide On Titan: Spectroscopic Detection and Mapping Using ALMA". In: *The Astrophysical Journal Letters* 800 - L14. DOI: https://doi.org/10.1088/2041-8205/800/1/L14.

Coustenis, A. et al. (2007). "The composition of Titan's stratosphere from Cassini/CIRS mid-infrared spectra". In: *Icarus* 189, pp. 35–62. DOI: doi:10.1016/j.icarus.2006.12.022.431.

D'Aversa, E. et al. (2017). "A visible solar occultation of Titan's atmosphere from Cassini-VIMS". In: *19th EGU General Assembly, EGU2017*. DOI: https://meetingorganizer.copernicus.org/EGU2017/EGU2017-5167.pdf.

Dekker, H. et al. (2000). "Design, construction and performance of UVES, the echelle spectrograph for the UT2 Kueyen telescope at the ESO Paranal". In: *Proc. SPIE 4008, Optical and IR Telescope Instrumentation and Detectors*. DOI: https://doi.org/10.1117/12.395512.

Dias, J. et al. (2022). "From Atmospheric Evolution to the Search of Species of Astrobiological Interest in the Solar System—Case Studies Using the Planetary Spectrum Generator". In: *Atmosphere* 13. DOI: https://doi.org/10.3390/atmos13030461.

Dobrijevic, M. et al. (2016). "1-D coupled photochemical model of neutrals, cations and anions in the atmosphere of Titan". In: *Icarus* 268, pp. 313–339. DOI: https://doi.org/10.1016/j.icarus.2015.12.045.

Dodda, L. et al. (2017). "LigParGen web server: an automatic OPLS-AA parameter generator for organic ligands". In: *Nucleic Acids Research* 45. DOI: https://doi.org/10.1093/nar/gkx312.

Ehrenfreund, P. et al. (2001). "The Photostability of Amino Acids in Space". In: *The Astrophysical Journal* 550, p. L95. DOI: 10.1086/319491.

Encrenaz, T. et al. (2010). *The Solar System*. Springer-Verlag.

Formisano, V. et al. (2004). "Detection of Methane in the Atmosphere of Mars". In: *Science* 306. DOI: https://doi.org/10.1126/science.1101732.

Friesner, R. et al. (2005). "Ab initio quantum chemistry: Methodology and applications". In: *PNAS* 102. DOI: doi:10.1073/pnas.0408036102.

Gausset, L. et al. (1965). "Analysis of the 4050-Ågroup of the C_3 molecule". In: *Astrophysical Journal* 142:45.

Gialluca, M. et al. (2021). "Characterizing Atmospheres of Transiting Earth-like Exoplanets Orbiting M Dwarfs with James Webb Space Telescope". In: *Publications of the Astronomical Society of the Pacific* 133. DOI: https://doi.org/10.1088/1538-3873/abf367.

Giver, L. et al. (1978). "Intensity measurements of the CH4 bands in the region 4350Å to 10600Å". In: *Journal of Quantitative Spectroscopy and Radiative Transfer* 19. DOI: https://doi.org/10.1016/00224073(78)90064-X.

Golec, B. et al. (2018). "Combined effect of hydrogen bonding interactions and freezing of rotameric equilibrium on the enhancement of photostability". In: *Physical Chemistry Chemical Physics* 19. DOI: DOIhttps://doi.org/10.1039/C8CP00726H.

Gómez-Zavaglia, A. et al. (2003). "Low-temperature solid-state FTIR study of glycine, sarcosine and N,N-dimethylglycine: observation of neutral forms of simple α-amino acids in the solid state". In: *Physical Chemistry Chemical Physics* 5, p. 3154. DOI: 10.1039/B304888H.

Gordon, I. et al. (2022). "The HITRAN2020 molecular spectroscopic database". In: *Journal of Quantitative Spectroscopy and Radiative Transfer* 272. DOI: https://doi.org/10.1016/j.jqsrt.2021.107949.

Hanel, R. et al. (2003). *Exploration of the Solar System by Infrared remote sensing, Second Edition*. Cambridge University Press.

Hargreaves, R. et al. (2020). "An Accurate, Extensive, and Practical Line List of Methane for the HITEMP Database". In: *The Astrophysical Journal Supplement Series* 247:55. DOI: https://doi.org/10.4533847/1538-4365/ab7a1a.

He, Q. et al. (2021). "Scattering and absorption cross sections of atmospheric gases in the ultraviolet–visible wavelength range (307–725nm)". In: *Atmospheric Chemistry and Physics* 21. DOI: https://doi.org/10.5194/acp-21-14927-2021.

Hérbad, E. et al. (2013). "Photochemistry of C3Hp hydrocarbons in Titan's stratosphere revisited". In: *Astronomy & Astrophysics* 552, A132. DOI: doi:10.1051/0004-6361/201220686.

Herrera, C. et al. (2016). "A molecular dynamics study on aminoacid-based ionic liquids". In: *Journal of Molecular Liquids* 213, pp. 201–212. DOI: http://dx.doi.org/10.1016/j.molliq.2015.10.056.

Hinkle, K. et al. (1988). "Detection of C_3 in the Circumstellar Shell of IRC+10216". In: *Science* 241. DOI: doi:10.1126/science.241.4871.1319.

Hörst, S. et al. (2012). "Formation of Amino Acids and Nucleotide Bases in a Titan Atmosphere Simulation Experiment". In: *Astrobiology* 12. DOI: DOI:10.1089/ast.2011.0623.

Hörst, S. (2017). "Titan's Atmosphere and Climate". In: *Journal of Geophysical Research: Planets* 122, p. 428. DOI: doi:doi:10.1002/2016JE005240.

Irwin, P. et al. (2008). "The NEMESIS planetary atmosphere radiative transfer and retrieval tool". In: *Journal of Quantitative Spectroscopy and Radiative Transfer* 109. DOI: https://doi.org/10.1016/j.jqsrt.2007.11.006.

Karkoschka, E. (1994). "Spectrophotometry of the Jovian Planets and Titan at 300- to 1000-nm Wavelength: The Methane Spectrum". In: *Icarus* 111:1. DOI: https://doi.org/10.1006/icar.1994.1139.

Karkoschka, E. and M. Tomasko (2010). "Methane absorption coefficients for the jovian planets from laboratory, Huygens, and HST data". In: *Icarus* 205. DOI: https://doi.org/10.1016/j.icarus.2009.07.044.

Kate, I. et al. (2005). "Amino acid photostability on the Martian surface". In: *Meteoritics & Planetary Science* 40, n.8, pp. 1185–1193. DOI: https://doi.org/10.1111/j.1945-5100.2005.tb00183.x.

Krasnopolsky, V. et al. (2004). "Detection of methane in the martian atmosphere: Evidence for life?" In: *Icarus* 172:2. DOI: https://doi.org/10.1016/j.icarus.2004.07.004.

Krissansen-Totton, J. et al. (2018). "Disequilibrium biosignatures over Earth history and implications for detecting exoplanet life". In: *Science Advances* 4. DOI: https://doi.org/10.1126/sciadv.aao5747.

Lellouch, E. et al. (2022). "Pluto's atmosphere observations with ALMA: spatially-resolved maps of CO and HCN emission and first detection of HNC". In: *Icarus* 372. DOI: 10.1016/j.icarus.2021.114722.

Lombardo, N. et al. (2019). "Detection of propadiene on Titan". In: *The Astrophysical Journal Letters* 881:L33. DOI: https://doi.org/10.3847/20418213/ab3860.

Lorenz, R. et al. (1999). "Seasonal Change on Titan Observed with the Hubble Space Telescope WFPC-2". In: *Icarus* 142. DOI: https://doi.org/10.1006/icar.1999.6225.

Lunine, J. and S. Atreya (2008). "The methane cycle on Titan". In: *Nature Geoscience* 1. DOI: doi:10.1038/ngeo125.

Luz, D. et al. (2006). "Characterization of zonal winds in the stratosphere of Titan with UVES: 2. Observations coordinated with the Huygens Probe entry". In: *Journal of Geophysical Research* 111. DOI: doi:10.1029/2005JE002617.

Machado, P. et al. (2014). "Wind circulation regimes at Venus' cloud tops: Ground-based Doppler velocimetry using CFHT/ESPaDOnS and comparison with simultaneous cloud tracking measurements using VEx/VIRTIS in February 2011". In: *Icarus* 243, pp. 249–263. DOI: https://doi.org/10.1016/j.icarus.2014.08.030.

Martins, L. et al. (2021). "Solubility of xenon in liquid n-alkanes and cycloalkanes by computer simulation. Towards the perfect anaesthetic". In: *Journal of Molecular Liquids* 340 - 117272. DOI: https://doi.org/10.1016/j.molliq.2021.117272.

Martins, Z. et al. (2013). "Shock synthesis of amino acids from impacting cometary and icy planet surface analogues". In: *Nature Geoscience* 6. DOI: DOI:10.1038/NGEO1930.

Maté, B. et al. (2011). "An infrared study of solid glycine in environments of astrophysical relevance". In: *Physical Chemistry Chemical Physics* 26, pp. 12268–12276. DOI: https://doi.org/10.1039/C1CP20899C.

McKay, C. et al. (2001). "Physical properties of the organic aerosols and clouds on Titan". In: *Planetary and Space Science* 49. DOI: https://doi.org/10.1016/S0032-0633(00)00051-9.

Minkov, V. et al. (2010). "A study of the temperature effect on the IR spectra of crystaline Amino Acids, Dipeptids, and Polyamino acids. VI. L-Alanine and DL-Alanine". In: *Journal of Structural Chemistry* 51, 6, pp. 1052–1063. DOI: https://doi.org/10.1007/s10947-010-0162-4.

Morgado, P. et al. (2020). "Solubility of water in perfluoroalkylalkanes surfactants: Evidence of specific interaction between water and the surfactant molecule". In: *Fluid Phase Equilibria* 522, p. 112754. DOI: https://doi.org/10.1016/j.fluid.2020.112754.

Niemann, H. et al. (2010). "Composition of Titan's lower atmosphere and simple surface volatiles as measured by the Cassini-Huygens probe gas chromatograph mass spectrometer experiment". In: *J. Geophys. Res.* 115, E12006. DOI: doi:10.1029/2010JE003659.

Nixon, C. et al. (2013). "Detection of Propene in Titan's Stratosphere". In: *The Astrophysical Journal Letters* 776:L14, 6pp. DOI: doi:10.1088/2041-8205/776/1/L14.

— (2020). "Detection of Cyclopropenylidene on Titan with ALMA". In: *The Astronomical Journal* 160. DOI: doi:10.3847/15383881/abb679.

Ohno, H. et al. (2007). "Amino Acid Ionic Liquids". In: *Accounts of Chemical Research* 40, 11, pp. 1122–1129. DOI: https://doi.org/10.1021/ar700053z.

Palmer, M. et al. (2017). "ALMA detection and astrobiological potential of vinyl cyanide on Titan". In: *Science Advances* 3. DOI: https://doi.org/10.1126/sciadv.1700022.

Parrinello, M. et al. (1981). "Polymorphic transitions in single crystals: A new molecular dynamics method". In: *J. Appl. Phys* 52, pp. 7182–7190. DOI: https://doi.org/10.1063/1.328693.

Pepe, F. et al. (2021). "ESPRESSO at VLT: On-sky performance and first results". In: *Astronomy and Astrophysics* 645, A96. DOI: https://doi.org/10.1051/0004-6361/202038306.

Poch, O. et al. (2013). "Chemical evolution of organic molecules under Mars-like UV radiation conditions simulated in the laboratory with the "Mars organic molecule irradiation and evolution" (MOMIE) setup". In: *Planetary and Space Science* 85, pp. 188–197. DOI: https://doi.org/10.1016/j.pss.2013.06.013.

Poggiali, P. et al. (2020). "Ultraviolet Photoprocessing of Glycine Adsorbed on Various Space-Relevant Minerals". In: *Frontiers in Astronomy and Space Sciences* 7. DOI: doi:10.3389/fspas.2020.00018.

Rigby, J. et al. (2023). "The Science Performance of JWST as Characterized in Commissioning". In: *Publications of the Astronomical Society of the Pacific* 135, p. 1046. DOI: 10.1088/1538-3873/acb293.

Robinson, J. (1996). *Atomic Spectroscopy - 2nd Edition, Revised and Expanded*. Marcel Dekker Inc.

Rodrígez-Lazcan, Y. et al. (2012). "Solid L--alanine: Spectroscopic properties and theoretical calculations". In: *Journal of Quantitative Spectroscopy and Radiative Transfer* 113 - 11, pp. 1266–1275. DOI: https://doi.org/10.1016/j.jqsrt.2012.01.020.

Roueff, E. et al. (2002). "Interstellar C_3 towards HD 210121". In: *Astronomy & Astrophysics* 384. DOI: https://doi.org/10.1051/0004-6361:20020067.

Sánchez-Lavega, A. (2011). *An Introduction to Planetary atmospheres*. Boca Raton, Florida, USA: Taylor & Francis.

Sbordone, L. et al. (2023). *Very Large Telescope Paranal Science Operations UV-Visual Echelle Spectrograph User manual*. EUROPEAN SOUTHERN OBSERVATORY, ESO.

Schmidt, M. et al. (2014). "Detection of vibronic band of C_3 in a translucent cloud towards HD 169454". In: *MNRAS* 441. DOI: https://doi.org/10.1093/mnras/stu641.

Smith, W. Hayden et al. (1990). "Absorption Coefficients for the 6190-Å CH4 Band between 290 and 100K with Application to Uranus' Atmosphere". In: *Icarus* 85. DOI: https://doi.org/10.1016/0019-1035(90)90103-G.

Tanabashi, A. et al. (2005). "; Fourrier transform emission of the (000)-(000) band of the λ4051.6 band of C_3". In: *The Astrophysical Journal* 624:2. DOI: doi:10.1086/429316.

Teanby, N. et al. (2006). "Latitudinal variations of HCN, HC_3N, and C_2N_2 in Titan's stratosphere derived from Cassini CIRS data". In: *Icarus* 181. DOI: https://doi.org/10.1016/j.icarus.2005.11.008.

Tennyson, J. et al. (2016). "The ExoMol database: Molecular line lists for exoplanet and other hot atmospheres". In: *Journal of Molecular Spectroscopy* 327, pp. 73–94. DOI: https://doi.org/10.1016/j.jms.2016.05.002.

Thompson, M. et al. (2022). "The case and context for atmospheric methane as an exoplanet biosignature". In: *PNAS* 119:14. DOI: https://doi.org/10.1073/pnas.2117933119.

Tinetti, G. et al. (2018). "A chemical survey of exoplanets with ARIEL, in Experimental". In: *Experimental Astronomy* 46. DOI: DOI:10.1007/s10686-018-9598-x.

Tobie, G. et al. (2006). "Episodic outgassing as the origin of atmospheric methane on Titan". In: *Nature* 440, pp. 61–64. DOI: doi:10.1038/nature04497.

— (2009). "Evolution of Titan and implications for its hydrocarbon cycle". In: *Philosophical of the Royal Society* 367. DOI: doi:10.1098/rsta.2008.0246.

Villanueva, G. et al. (2018). "Planetary spectrum generator:An accurate online radiative transfer suite for atmospheres, comets, small bodies and exoplanets". In: *Journal of Quantitative Spectroscopy and Radiative Transfer* 217. DOI: https://doi.org/10.1016/j.jqsrt.2018.05.023.

Vuitton, V. et al. (2019). "Simulating the density of organic species in the atmosphere of Titan with a coupled ion-neutral photochemical model". In: *Icarus* 324, pp. 120–197. DOI: doi.org/10.1016/j.icarus.2018.06.013.

Appendix A

Supplementary Information

A. SUPPLEMENTARY INFORMATION

TableA.1: List of all 8 detected lines by our method at the spectral section comprising the weak CH_4 5430Å absorption band, ranked by line depth. Presented Line Strength, S_i, measurements are retrieved from the Equivalent Width (EW) and the Model Fit (MF) method. Line Wavelength uncertainty is obtained as the maximum dispersion of assigned line wavelengths for the 4 observation nights. Some of these lines are shown detected at the spectral plot of figure 5 of the main article. These spectral lines are likely part of the $6\nu_1+\nu_3$ CH_4 band as described by Giver et al., 1978.

Line	Wavelength (Å)	Line Depth (%)	Line EW (cm^{-1})	S_i, EW, (cm/molec)	S_i, MF, (cm/molec)
1	5427.01 ± 0.02	3.8 ± 0.3	0.011 ± 0.003	(8.5 ± 2.3) x 10^{-25}	(2.5 ± 0.5) x 10^{-25}
2	5449.49 ± 0.02	2.4 ± 0.4	0.007 ± 0.002	(5.0 ± 1.8) x 10^{-25}	(1.0 ± 0.5) x 10^{-25}
3	5430.75 ± 0.02	2.4 ± 0.3	0.009 ± 0.004	(7.0 ± 3.0) x 10^{-25}	(1.5 ± 0.5) x 10^{-25}
4	5433.99 ± 0.01	2.3 ± 0.6	0.005 ± 0.003	(4.0 ± 2.0) x 10^{-25}	(1.5 ± 0.5) x 10^{-25}
5	5427.49 ± 0.02	2.1 ± 0.1	0.006 ± 0.002	(4.4 ± 1.2) x 10^{-25}	(1.5 ± 0.5) x 10^{-25}
6	5442.84 ± 0.02	2.0 ± 0.3	0.006 ± 0.002	(4.4 ± 1.4) x 10^{-25}	(1.5 ± 0.5) x 10^{-25}
7	5427.29 ± 0.01	1.9 ± 0.2	0.007 ± 0.002	(5.6 ± 1.3) x 10^{-25}	(1.5 ± 0.5) x 10^{-25}
8	5439.26 ± 0.01	1.8 ± 0.2	0.008 ± 0.003	(6.2 ± 2.2) x 10^{-25}	(1.0 ± 0.5) x 10^{-25}

TableA.2: 4 detected non-solar lines at the weak CH_4 5760Å absorption band, ranked by line depth. These spectral lines are likely part of the $5\nu_1+\nu_3+(\nu_2$ or $\nu_4)$ CH_4 band as described by Giver et al., 1978 (1978)

Line	Wavelength (Å)	Line Depth (%)	Line EW (cm^{-1})	S_i, EW, (cm/molec)	S_i, MF, (cm/molec)
1	5779.46 ± 0.01	2.5 ± 0.5	0.005 ± 0.002	(4.2 ± 1.8) x 10^{-25}	(1.5 ± 0.5) x 10^{-25}

TableA.3: 2 detected non-solar lines at the weak CH_4 5970Å absorption band, ranked by line depth. These spectral lines are likely part of the $4\nu_1+2\nu_3$ CH_4 band as described by Giver et al., 1978.

Line	Wavelength (Å)	Line Depth (%)	Line EW (cm^{-1})	S_i, EW, (cm/molec)	S_i, MF, (cm/molec)
1	5959.40 ± 0.02	2.3 ± 0.3	0.006 ± 0.002	(4.3 ± 1.4) x 10^{-25}	(1.5 ± 0.5) x 10^{-25}

Table A.4: List of all 87 detected lines by our method at the spectral section comprising the weak CH_4 6190Å absorption band, ranked by line depth. Presented Line Strength, S_i, measurements are retrieved from the Equivalent Width (EW) and the Model Fit (MF) method. Line Wavelength uncertainty is obtained as the maximum dispersion of assigned line wavelengths for the 4 observation nights. Some of these lines are shown detected at the spectral plot of figure 4 of the main article. These spectral lines are likely part of the $5\nu_1+\nu_3$ CH_4 band as described by Giver et al., 1978

Line	Wavelength (Å)	Line Depth (%)	Line EW (cm^{-1})	S_i, EW, (cm/molec)	S_i, MF, (cm/molec)
1	6182.21 ± 0.01	13.8 ± 0.3	0.033 ± 0.007	(24.7 ± 5.0) x 10^{-25}	(8.5 ± 0.5) x 10^{-25}
2	6183.91 ± 0.01	10.6 ± 0.4	0.020 ± 0.005	(15.5 ± 4.1) x 10^{-25}	(6.5 ± 0.5) x 10^{-25}
3	6177.73 ± 0.00	8.5 ± 0.3	0.017 ± 0.004	(13.1 ± 3.2) x 10^{-25}	(4.5 ± 0.5) x 10^{-25}
4	6184.39 ± 0.01	7.9 ± 0.9	0.018 ± 0.005	(13.5 ± 4.1) x 10^{-25}	(4.0 ± 0.5) x 10^{-25}
5	6183.01 ± 0.01	7.3 ± 0.8	0.023 ± 0.006	(17.7 ± 4.4) x 10^{-25}	(4.5 ± 0.5) x 10^{-25}
6	6185.13 ± 0.02	6.7 ± 1.2	0.014 ± 0.005	(11.0 ± 4.1) x 10^{-25}	(4.0 ± 0.5) x 10^{-25}
7	6180.98 ± 0.01	6.6 ± 0.3	0.028 ± 0.004	(21.4 ± 3.1) x 10^{-25}	(3.5 ± 0.5) x 10^{-25}
8	6179.37 ± 0.02	6.3 ± 0.5	0.015 ± 0.004	(11.4 ± 2.9) x 10^{-25}	(4.5 ± 0.5) x 10^{-25}
9	6184.92 ± 0.01	6.1 ± 0.1	0.014 ± 0.003	(10.5 ± 2.2) x 10^{-25}	(3.0 ± 0.5) x 10^{-25}
10	6181.41 ± 0.02	6.1 ± 1.7	0.015 ± 0.009	(11.3 ± 7.2) x 10^{-25}	(4.5 ± 0.5) x 10^{-25}
11	6178.72 ± 0.01	6.0 ± 1.3	0.013 ± 0.006	(10.2 ± 4.2) x 10^{-25}	(3.5 ± 0.5) x 10^{-25}
12	6181.79 ± 0.01	5.9 ± 0.3	0.016 ± 0.003	(12.5 ± 2.5) x 10^{-25}	(3.5 ± 0.5) x 10^{-25}
13	6172.29 ± 0.01	5.9 ± 0.2	0.012 ± 0.003	(9.2 ± 2.3) x 10^{-25}	(4.0 ± 0.5) x 10^{-25}
14	6178.28 ± 0.01	5.8 ± 0.8	0.012 ± 0.004	(9.4 ± 3.2) x 10^{-25}	(3.5 ± 0.5) x 10^{-25}
15	6179.55 ± 0.02	5.5 ± 0.4	0.010 ± 0.003	(7.6 ± 2.4) x 10^{-25}	(3.0 ± 0.5) x 10^{-25}
16	6175.08 ± 0.02	5.2 ± 1.9	0.012 ± 0.009	(9.4 ± 6.8) x 10^{-25}	(3.0 ± 0.5) x 10^{-25}
17	6180.71 ± 0.01	5.2 ± 0.1	0.013 ± 0.002	(10.1 ± 1.8) x 10^{-25}	(3.0 ± 0.5) x 10^{-25}
18	6132.58 ± 0.02	4.7 ± 0.2	0.013 ± 0.003	(10.0 ± 1.9) x 10^{-25}	(3.0 ± 0.5) x 10^{-25}
19	6150.40 ± 0.02	4.7 ± 1.4	0.010 ± 0.005	(7.6 ± 3.8) x 10^{-25}	(2.0 ± 0.5) x 10^{-25}
20	6179.81 ± 0.01	4.4 ± 0.7	0.008 ± 0.003	(5.8 ± 2.4) x 10^{-25}	(2.5 ± 0.5) x 10^{-25}
21	6131.27 ± 0.02	4.0 ± 0.9	0.010 ± 0.004	(7.9 ± 3.2) x 10^{-25}	(2.5 ± 0.5) x 10^{-25}
22	6164.80 ± 0.01	4.0 ± 0.3	0.007 ± 0.002	(5.5 ± 1.7) x 10^{-25}	(2.0 ± 0.5) x 10^{-25}
23	6163.09 ± 0.02	3.9 ± 0.5	0.008 ± 0.003	(6.4 ± 2.0) x 10^{-25}	(1.5 ± 0.5) x 10^{-25}
24	6136.11 ± 0.02	3.8 ± 1.3	0.015 ± 0.007	(11.6 ± 5.1) x 10^{-25}	(2.5 ± 0.5) x 10^{-25}
25	6145.49 ± 0.02	3.8 ± 1.7	0.012 ± 0.008	(8.8 ± 6.4) x 10^{-25}	(2.0 ± 0.5) x 10^{-25}
26	6180.52 ± 0.02	3.6 ± 0.9	0.008 ± 0.005	(5.9 ± 3.7) x 10^{-25}	(2.0 ± 0.5) x 10^{-25}
27	6172.90 ± 0.00	3.6 ± 0.3	0.011 ± 0.002	(8.2 ± 1.8) x 10^{-25}	(2.0 ± 0.5) x 10^{-25}
28	6175.84 ± 0.02	3.5 ± 0.1	0.008 ± 0.002	(6.3 ± 1.3) x 10^{-25}	(2.0 ± 0.5) x 10^{-25}

Continued on next page

A. SUPPLEMENTARY INFORMATION

Line	Wavelength (Å)	Line Depth (%)	Line EW (cm^{-1})	S_i, EW, (cm/molec)	S_i, MF, (cm/molec)
29	6181.54 ± 0.02	3.4 ± 0.9	0.007 ± 0.003	(5.2 ± 2.5) x 10^{-25}	(3.0 ± 0.5) x 10^{-25}
30	6172.43 ± 0.01	3.4 ± 0.3	0.007 ± 0.002	(5.0 ± 1.5) x 10^{-25}	(2.0 ± 0.5) x 10^{-25}
31	6176.32 ± 0.02	3.4 ± 1.1	0.006 ± 0.003	(4.9 ± 2.6) x 10^{-25}	(2.0 ± 0.5) x 10^{-25}
32	6158.64 ± 0.02	3.3 ± 0.1	0.009 ± 0.002	(6.7 ± 1.3) x 10^{-25}	(2.0 ± 0.5) x 10^{-25}
33	6164.59 ± 0.01	3.3 ± 1.2	0.008 ± 0.006	(5.9 ± 4.3) x 10^{-25}	(2.0 ± 0.5) x 10^{-25}
34	6143.06 ± 0.02	3.2 ± 0.4	0.007 ± 0.002	(5.3 ± 1.7) x 10^{-25}	(2.0 ± 0.5) x 10^{-25}
35	6154.81 ± 0.01	3.2 ± 1.1	0.007 ± 0.005	(5.5 ± 4.0) x 10^{-25}	(1.5 ± 0.5) x 10^{-25}
36	6166.75 ± 0.02	3.1 ± 0.8	0.010 ± 0.004	(7.4 ± 2.9) x 10^{-25}	(2.0 ± 0.5) x 10^{-25}
37	6127.39 ± 0.02	3.1 ± 0.4	0.008 ± 0.002	(5.9 ± 1.8) x 10^{-25}	(2.0 ± 0.5) x 10^{-25}
38	6159.74 ± 0.01	3.1 ± 0.6	0.011 ± 0.004	(8.6 ± 2.7) x 10^{-25}	(2.5 ± 0.5) x 10^{-25}
39	6147.23 ± 0.01	3.0 ± 0.3	0.006 ± 0.002	(4.7 ± 1.5) x 10^{-25}	(2.0 ± 0.5) x 10^{-25}
40	6167.04 ± 0.02	3.0 ± 0.4	0.006 ± 0.002	(4.2 ± 1.6) x 10^{-25}	(2.0 ± 0.5) x 10^{-25}
41	6129.43 ± 0.02	3.0 ± 0.2	0.008 ± 0.002	(5.7 ± 1.3) x 10^{-25}	(2.5 ± 0.5) x 10^{-25}
42	6179.10 ± 0.02	3.0 ± 0.9	0.007 ± 0.004	(5.6 ± 2.7) x 10^{-25}	(2.0 ± 0.5) x 10^{-25}
43	6182.77 ± 0.02	2.9 ± 0.4	0.007 ± 0.003	(5.5 ± 2.6) x 10^{-25}	(2.5 ± 0.5) x 10^{-25}
44	6152.33 ± 0.02	2.9 ± 0.7	0.008 ± 0.005	(5.7 ± 4.2) x 10^{-25}	(2.0 ± 0.5) x 10^{-25}
45	6148.78 ± 0.01	2.9 ± 0.5	0.007 ± 0.002	(4.9 ± 1.8) x 10^{-25}	(1.5 ± 0.5) x 10^{-25}
46	6178.46 ± 0.02	2.9 ± 0.8	0.006 ± 0.003	(4.9 ± 2.3) x 10^{-25}	(2.5 ± 0.5) x 10^{-25}
47	6150.69 ± 0.02	2.8 ± 0.1	0.009 ± 0.002	(6.9 ± 1.2) x 10^{-25}	(1.5 ± 0.5) x 10^{-25}
48	6142.80 ± 0.02	2.8 ± 0.4	0.006 ± 0.002	(4.4 ± 1.6) x 10^{-25}	(1.5 ± 0.5) x 10^{-25}
49	6165.99 ± 0.02	2.8 ± 0.7	0.005 ± 0.002	(4.1 ± 1.9) x 10^{-25}	(1.5 ± 0.5) x 10^{-25}
50	6171.95 ± 0.01	2.7 ± 0.4	0.006 ± 0.003	(4.9 ± 2.5) x 10^{-25}	(1.5 ± 0.5) x 10^{-25}
51	6145.76 ± 0.01	2.7 ± 0.7	0.007 ± 0.003	(5.6 ± 2.3) x 10^{-25}	(1.5 ± 0.5) x 10^{-25}
52	6109.84 ± 0.01	2.7 ± 0.3	0.006 ± 0.002	(4.4 ± 1.3) x 10^{-25}	(1.5 ± 0.5) x 10^{-25}
53	6139.02 ± 0.02	2.7 ± 1.2	0.005 ± 0.003	(3.9 ± 2.6) x 10^{-25}	(1.5 ± 0.5) x 10^{-25}
54	6173.89 ± 0.00	2.6 ± 0.3	0.007 ± 0.004	(5.6 ± 3.3) x 10^{-25}	(1.5 ± 0.5) x 10^{-25}
55	6112.24 ± 0.01	2.6 ± 0.1	0.008 ± 0.002	(6.1 ± 1.2) x 10^{-25}	(1.5 ± 0.5) x 10^{-25}
56	6174.77 ± 0.00	2.6 ± 0.1	0.006 ± 0.001	(4.5 ± 1.1) x 10^{-25}	(1.5 ± 0.5) x 10^{-25}
57	6140.76 ± 0.02	2.6 ± 0.5	0.007 ± 0.003	(5.4 ± 1.9) x 10^{-25}	(1.5 ± 0.5) x 10^{-25}
58	6132.84 ± 0.01	2.5 ± 0.2	0.007 ± 0.002	(5.4 ± 1.2) x 10^{-25}	(1.5 ± 0.5) x 10^{-25}

Continued on next page

Line	Wavelength (Å)	Line Depth (%)	Line EW (cm^{-1})	S_i, EW, (cm/molec)	S_i, MF, (cm/molec)
59	6179.18 ± 0.02	2.5 ± 0.2	0.011 ± 0.002	(8.0 ± 1.6) x 10^{-25}	(2.0 ± 0.5) x 10^{-25}
60	6157.11 ± 0.02	2.5 ± 0.2	0.006 ± 0.002	(4.3 ± 1.2) x 10^{-25}	(1.5 ± 0.5) x 10^{-25}
61	6146.71 ± 0.02	2.5 ± 0.7	0.006 ± 0.003	(4.4 ± 2.2) x 10^{-25}	(1.0 ± 0.5) x 10^{-25}
62	6143.78 ± 0.01	2.4 ± 0.6	0.005 ± 0.002	(4.0 ± 1.9) x 10^{-25}	(1.5 ± 0.5) x 10^{-25}
63	6165.01 ± 0.01	2.4 ± 0.2	0.006 ± 0.002	(4.3 ± 1.1) x 10^{-25}	(1.0 ± 0.5) x 10^{-25}
64	6175.68 ± 0.02	2.4 ± 0.1	0.006 ± 0.001	(4.5 ± 0.9) x 10^{-25}	(1.5 ± 0.5) x 10^{-25}
65	6140.40 ± 0.00	2.3 ± 0.3	0.006 ± 0.002	(4.4 ± 1.3) x 10^{-25}	(1.5 ± 0.5) x 10^{-25}
66	6117.35 ± 0.01	2.3 ± 0.6	0.006 ± 0.003	(4.2 ± 2.6) x 10^{-25}	(1.0 ± 0.5) x 10^{-25}
67	6144.47 ± 0.01	2.3 ± 0.3	0.007 ± 0.002	(5.5 ± 1.4) x 10^{-25}	(1.0 ± 0.5) x 10^{-25}
68	6148.12 ± 0.02	2.2 ± 0.6	0.005 ± 0.003	(3.9 ± 2.6) x 10^{-25}	(1.0 ± 0.5) x 10^{-25}
69	6174.01 ± 0.00	2.2 ± 0.5	0.005 ± 0.003	(3.6 ± 2.3) x 10^{-25}	(1.5 ± 0.5) x 10^{-25}
70	6177.50 ± 0.02	2.2 ± 0.1	0.005 ± 0.001	(4.1 ± 0.9) x 10^{-25}	(1.0 ± 0.5) x 10^{-25}
71	6171.82 ± 0.01	2.2 ± 0.6	0.003 ± 0.002	(2.3 ± 1.3) x 10^{-25}	(1.5 ± 0.5) x 10^{-25}
72	6152.96 ± 0.01	2.2 ± 0.8	0.004 ± 0.004	(3.4 ± 2.7) x 10^{-25}	(1.0 ± 0.5) x 10^{-25}
73	6158.23 ± 0.02	2.2 ± 0.6	0.008 ± 0.004	(5.8 ± 3.1) x 10^{-25}	(1.5 ± 0.5) x 10^{-25}
74	6085.62 ± 0.02	2.1 ± 0.1	0.006 ± 0.001	(4.8 ± 0.9) x 10^{-25}	(1.5 ± 0.5) x 10^{-25}
75	6147.37 ± 0.02	2.1 ± 0.8	0.004 ± 0.002	(3.0 ± 1.8) x 10^{-25}	(1.5 ± 0.5) x 10^{-25}
76	6132.32 ± 0.02	2.0 ± 0.3	0.005 ± 0.002	(3.7 ± 1.2) x 10^{-25}	(1.0 ± 0.5) x 10^{-25}
77	6138.75 ± 0.02	2.0 ± 0.4	0.005 ± 0.003	(3.9 ± 2.1) x 10^{-25}	(1.0 ± 0.5) x 10^{-25}
78	6141.23 ± 0.02	2.0 ± 0.6	0.006 ± 0.003	(4.5 ± 1.9) x 10^{-25}	(1.0 ± 0.5) x 10^{-25}
79	6182.44 ± 0.01	2.0 ± 0.3	0.006 ± 0.003	(4.4 ± 2.5) x 10^{-25}	(1.0 ± 0.5) x 10^{-25}
80	6158.40 ± 0.02	1.9 ± 0.2	0.004 ± 0.001	(3.3 ± 0.9) x 10^{-25}	(1.0 ± 0.5) x 10^{-25}
81	6168.64 ± 0.01	1.9 ± 0.1	0.003 ± 0.001	(2.2 ± 0.7) x 10^{-25}	(1.0 ± 0.5) x 10^{-25}
82	6149.87 ± 0.02	1.9 ± 0.4	0.003 ± 0.002	(2.6 ± 1.8) x 10^{-25}	(1.0 ± 0.5) x 10^{-25}
83	6138.15 ± 0.00	1.9 ± 0.5	0.005 ± 0.003	(3.4 ± 2.2) x 10^{-25}	(1.0 ± 0.5) x 10^{-25}
84	6177.93 ± 0.00	1.8 ± 0.5	0.003 ± 0.002	(2.4 ± 1.8) x 10^{-25}	(1.0 ± 0.5) x 10^{-25}
85	6151.06 ± 0.02	1.8 ± 0.3	0.004 ± 0.002	(3.0 ± 1.8) x 10^{-25}	(1.0 ± 0.5) x 10^{-25}
86	6153.74 ± 0.02	1.8 ± 0.6	0.004 ± 0.003	(3.1 ± 2.2) x 10^{-25}	(1.0 ± 0.5) x 10^{-25}
87	6174.35 ± 0.02	1.8 ± 0.3	0.004 ± 0.002	(3.1 ± 1.6) x 10^{-25}	(1.5 ± 0.5) x 10^{-25}

A. SUPPLEMENTARY INFORMATION

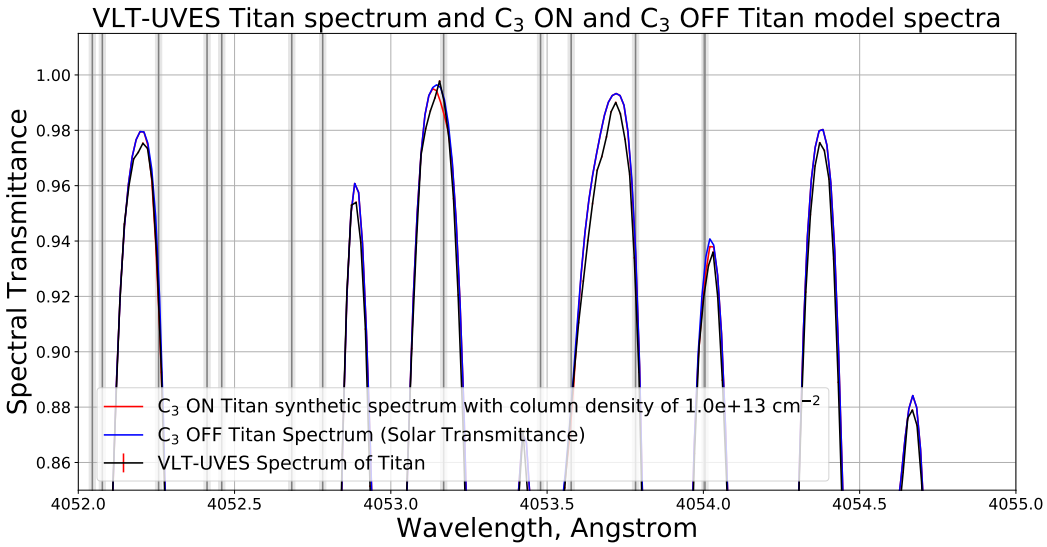

Figure A.1: Normalised Spectrum of Titan (black) compared with a synthetic normalised spectrum of Titan with a C_3 column density of 1.0×10^{13} cm^{-2} (red) and a normalised solar spectrum (blue) as a proxy for a synthetic spectrum of Titan without C_3 absorption features, obtained in the same fashion as figure 7 of the main article, but zooming on the rest of the wavelength range of the C_3 4051Å band, from 4052Å to 4055Å. Vertical grey lines correspond to C_3 line centres and respective uncertainty identified in Schmidt et al., 2014. As mentioned on the main article, no C_3 absorption line matches a spectral region devoid of deep solar lines in this section of Titan's spectrum, preventing any C_3 line detection in this section of the band.